Radio galaxies near the epoch of reionisation

Saxena, A.

Author: Saxena, A.
Title: Radio galaxies near the epoch of reionisation
Issue Date: 2019-06-26

Radio Galaxies near the Epoch of Reionisation

Proefschrift

ter verkrijging van
de graad van Doctor aan de Universiteit Leiden,
op gezag van Rector Magnificus prof. mr. C.J.J.M. Stolker,
volgens besluit van het College voor Promoties
te verdedigen op Woensdag 26 Juni 2019
klokke 12:30 uur

door

Aayush Saxena
geboren te New Delhi, India
in 1992

Promotiecommissie

Promotor:	Prof. dr. Huub Röttgering
Co-promotor:	Dr. Kenneth Duncan

Promotiecommissie:	Prof. dr. Marijn Franx
	Prof. dr. Paul van der Werf
	Prof. dr. George Miley
	Prof. dr. Carole Jackson
	Prof. dr. Laura Pentericci (INAF-OAR, Italy)
	Dr. Rychard Bouwens
	Dr. Jacqueline Hodge
	Dr. Carlos de Breuck (ESO, Germany)

ISBN: 978 94 6380 379 3
Cover: A radio galaxy inflating ionising bubbles, reionising the neutral Universe.
Printed by: ProefschriftMaken || www.proefschriftmaken.nl

To those who have dedicated their lives to making other people's lives better.

The atom bombs are piling up in the factories, the police are prowling through the cities, the lies are streaming from the loudspeakers, but the earth is still going round the sun, and neither the dictators nor the bureaucrats, deeply as they disapprove of the process, are able to prevent it.

– George Orwell[1]

[1] Some Thoughts on the Common Toad, 1946

Contents

1 Introduction **1**
1.1 Historical context 1
1.1.1 Radio galaxies 2
1.2 High-redshift radio galaxies 4
1.2.1 Selection techniques 4
1.2.2 Follow-up of promising candidates 7
1.3 Physics of Radio-loud AGN 7
1.3.1 Powering the radio emission 8
1.3.2 Powering the rest-frame optical/NIR emission lines 8
1.4 A panchromatic view of high-redshift radio galaxies 10
1.4.1 Radio 10
1.4.2 Ultraviolet/optical/near-infrared 11
1.4.3 Mid-infrared/far-infrared/sub-mm 12
1.4.4 X-rays 12
1.5 Cosmological properties of high-redshift radio galaxies 13
1.5.1 Number density at high redshifts 13
1.5.2 Formation and evolution of massive galaxies across cosmic time 13
1.5.3 AGN feedback 14
1.5.4 Large scale structure formation 15
1.5.5 Probes of the epoch of reionisation 16
1.6 This thesis 18
1.7 Outlook 20

2 Modelling the luminosities and sizes of radio sources: radio luminosity function at z = 6 **21**
2.1 Introduction 22
2.2 Modelling radio luminosities and linear sizes 24
2.2.1 Input black hole mass function and Eddington ratio distribution 24
2.2.2 Radio jet power calculation 25
2.2.3 Radio luminosity calculation 26
2.3 Radio luminosities and linear sizes at z = 2 29
2.3.1 Model Input 29

2.3.2 Output jet power distribution . . . 30
2.3.3 Constructing and normalising the radio luminosity function 32
2.3.4 Output luminosity functions . . . 34
2.3.5 Output size distribution . . . 35
2.4 Implementing the model at z = 6 . . . 37
2.4.1 Model input . . . 37
2.4.2 Model predictions at z = 6 . . . 38
2.4.3 Comparison with exponential evolution of space densities 42
2.4.4 Implications of radio luminosity function at z = 6 . . . 44
2.5 Summary . . . 48
2.A Calculation of Inverse Compton loss distance . . . 50

3 A search for faint high-redshift radio galaxy candidates at 150 MHz 53
3.1 Introduction . . . 54
3.2 Radio data sets and sample selection . . . 57
3.2.1 TIFR GMRT Sky Survey (TGSS) Alternative Data Release at 150 MHz . . . 57
3.2.2 VLA FIRST and NVSS at 1.4 GHz . . . 57
3.2.3 Target selection . . . 57
3.3 VLA L and P-band observations . . . 64
3.3.1 Objectives . . . 64
3.3.2 Observations and data reduction . . . 64
3.3.3 Flux densities and morphologies . . . 65
3.4 Multi-wavelength properties and interesting sources . . . 69
3.4.1 Optical and IR photometry . . . 69
3.4.2 Comments on interesting sources in the sample . . . 70
3.5 Discussion . . . 79
3.5.1 Radio pulsars . . . 79
3.5.2 Dust obscured radio galaxies . . . 81
3.5.3 Diffuse sources: radio halos and fading radio galaxies . . . 81
3.6 Summary . . . 82
3.A Source catalog . . . 84
3.B VLA L-band images and contour maps . . . 87

4 Discovery of a radio galaxy at z = 5.72 93
4.1 Introduction . . . 94
4.2 Source selection . . . 95
4.3 Observations . . . 98
4.3.1 Gemini GMOS spectroscopy . . . 98
4.3.2 Large Binocular Telescope NIR imaging . . . 101

4.4 Redshift determination 103
4.4.1 Skewness and equivalent width 105
4.4.2 K-z relation for radio galaxies 105
4.5 Discussion 106
4.5.1 Emission line measurements 106
4.5.2 Radio properties 107
4.5.3 Stellar mass limits 111
4.6 Conclusions 113

5 Search for faint high-redshift radio galaxies II: spectroscopic and near-infrared observations 117
5.1 Introduction 118
5.2 The faint HzRG sample 121
5.2.1 Sample selection 121
5.2.2 Observations and data reduction 121
5.2.3 Results 126
5.2.4 Properties of the faint radio galaxy sample 132
5.3 Comparison with literature HzRG sample 134
5.3.1 Literature samples 135
5.3.2 Comparison of emission line and radio properties 137
5.4 Discussion 145
5.4.1 Lyα emission in faint HzRGs is powered by weak AGN . . 145
5.4.2 No direct evidence of strong interaction between radio jet and line-emitting gas 146
5.4.3 Faint HzRGs have lower stellar masses 146
5.4.4 Are faint HzRG hosts rapidly assembling their stellar mass? 148
5.4.5 Inverse Compton losses dominant at high redshift 149
5.5 Summary 152
5.A Long-slit spectra 154
5.B K-band images 158

Bibliography 160

Nederlandse Samenvatting 171

List of publications 175

Curriculum Vitae 177

Acknowledgements **179**

1 Introduction

1.1 Historical context

Although several attempts were made to image the sun at radio (meter) wavelengths in the late 19th century, the recent history of radio astronomy begins with the pioneering engineer Karl G. Jansky who began experimenting with detecting radio emission from the sky using an antenna that he built while working for Bell Telephone Laboratories. From his initial observations, Jansky published a series of papers reporting the detection of radio emission from outside the solar system, and specifically from the centre of the Milky Way (Jansky 1933a,b), which failed to attract much attention. Jansky was subsequently reassigned to another project and did no further work in radio astronomy. The field of astronomy would eventually recognise the importance of his work by naming the unit of flux density after him, where 1 Jansky (Jy) = 10^{-26} Watt Hz^{-1} m^{-2}.

Jansky's papers captured the attention of another radio engineer, Grote Reber. In 1937, Reber built what could be attributed as the first ever radio 'telescope', consisting of a 9.5-m parabolic reflector dish, in his backyard and began surveying the radio sky. He corroborated Jansky's detection of radio emission from the Galactic plane and in 1944 Reber published a map of the radio sky finding peaks in emission originating from the constellations of Sagittarius (galactic centre), Cygnus, Cassiopeiae, Canis Major and Puppis (Reber 1944). Only a couple of years later, Hey et al. (1946) reported the detection of radio fluctuations from the constellation Cygnus, which would be the first truly extragalactic source observed at radio wavelengths (Cygnus A).

The end of the Second World War ushered in an era of large-sky radio surveys, primarily led by ex-radar scientists based in Cambridge, Manchester and Sydney. Over the next few decades, these surveys would lead to the discovery of hundreds, and even thousands of radio sources, a large majority of which were extragalactic

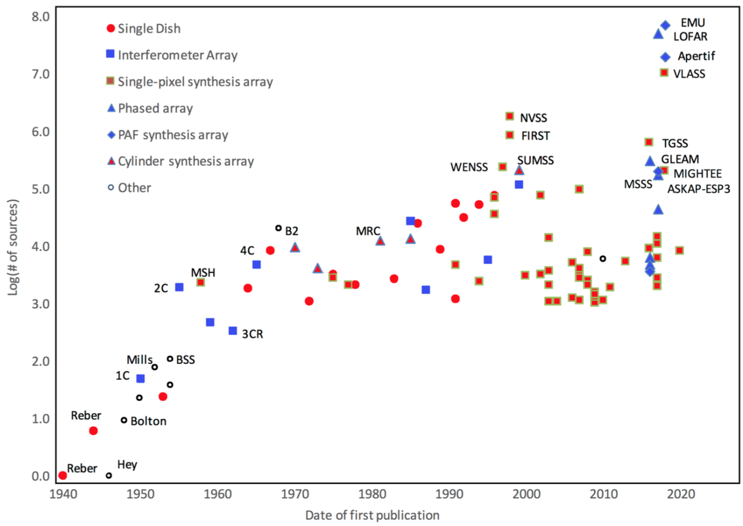

Figure 1.1: Number of known extragalactic radio sources discovered by surveys as a function of time, taken from Norris (2017).

in nature. The best example of one such early survey is the 2C radio survey at Cambridge, that lead to the detection of 1,936 discrete radio sources at an observing frequency of 81 MHz (Shakeshaft et al. 1955). Interestingly, the distribution of radio flux densities of the 'radio stars' in this survey was incompatible with the Euclidean distribution of 'standard candle' sources in the Universe, and was used to rule out the 'Steady State' theory in favour of the 'Big Bang' model for the Universe (Ryle & Scheuer 1955). This remarkable result increased radio astronomy efforts all around the world, in the form of the construction of larger telescopes offering higher sensitivities and better angular resolutions. This resulted in a tremendous increase in the number of known radio sources, and the number of radio sources detected in surveys over the last few decades is shown in Figure 1.1 taken from Norris (2017). We draw the attention of the reader that the y-axis of Figure 1.1 is logarithmic.

1.1.1 Radio galaxies

Although radio surveys have led to the discovery of a plethora of radio sources that include radio pulsars, star-forming galaxies, galaxy clusters and the more recently discovered fast radio bursts, the focus of this thesis is on extragalactic active galactic nuclei (AGN) that emit copious amounts of radio emission. The classi-

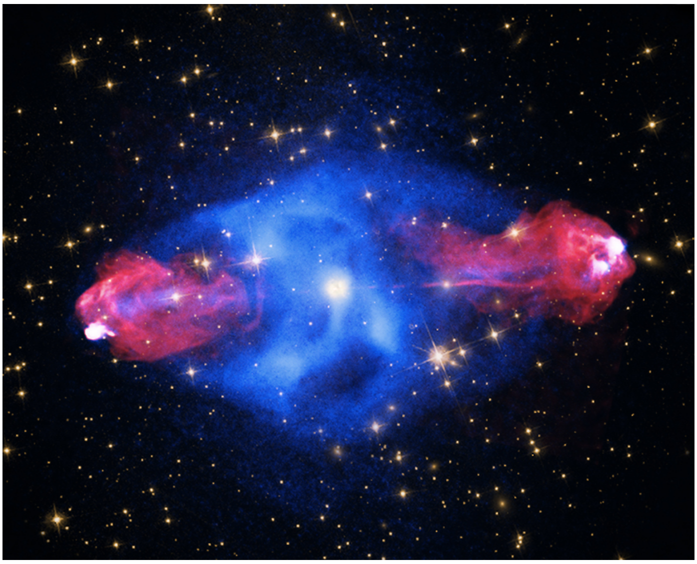

Figure 1.2: Light from Cygnus A at radio (red), X-ray (blue) and optical (background) wavelengths. Cygnus A is a typical twin lobed radio source powered by accretion on to the central SMBH. Image Credit: X-ray: NASA/CXC/SAO; Optical: NASA/STScI; Radio: NSF/NRAO/AUI/VLA. Taken from NASA's Astronomy Picture of the Day, 24 January 2015.

cal 'radio galaxies' discovered in early large-sky surveys usually consisted of two radio 'lobes' that are created by synchrotron radiation from relativistic plasma believed to be ejected as a consequence of material falling on to the supermassive black hole (SMBH) in an AGN. Quite often, the core of the AGN shines brightly at radio wavelengths too. A quintessential example of a radio galaxy in the local Universe – and arguably the first extragalactic radio source discovered – is Cygnus A at a redshift of 0.056 (Baade & Minkowski 1954). In Figure 1.2 a composite image for this radio galaxy with emission at radio (red), X-ray (blue) and optical wavelengths (background) is shown. Cygnus A also shows radio emission from the core of the AGN which is also traced by high-energy X-rays and we elaborate on the various observational signatures from radio galaxies in Section 3.

Many other "local" ($z \sim 0$ radio galaxies displayed morphologies similar to Cygnus A, with their radio lobes extending to hundreds of kiloparsecs. Based on their radio morphology, there were two distinct types of radio galaxies identified. This is the so-called Fanaroff & Riley (1974) classification, where Fanaroff-Riley II (FRII) sources have an edge-brightened morphology and Fanaroff-Riley I (FRI) sources have the peak of emission towards the host galaxy. FRII sources typically have higher radio luminosities. At higher redshifts, radio sources are seen to typically exhibit FRII morphologies and luminosities.

1.2 High-redshift radio galaxies

It was clear that in order to derive meaningful properties of the host galaxies of radio sources, such as the distance, underlying stellar populations, star-formation histories, etc., dedicated imaging and spectroscopic follow-up at optical wavelengths were essential. Spectroscopy of bright radio sources was yielding redshift measurements that were breaking distance records – a redshift of $z = 0.462$ measured by Minkowski (1960) for the radio source 3C 295 was the most distant object known at the time. With the arrival of radio interferometric techniques in the 1950s (such as the Cambridge One-Mile Telescope and Jodrell Bank long-baseline interferometry), precise position measurements for strong radio sources were possible and enabled accurate identification of the host galaxies of radio sources. The first radio galaxy at $z > 1$ was discovered by Spinrad (1982). Chambers et al. (1988) then discovered a radio galaxy at $z > 2$, with the discovery of a $z > 3$ radio galaxy reported only a few months later by Lilly (1988). A couple of years later Chambers et al. (1990) reported the discovery of a radio galaxy at $z = 3.8$. A radio galaxy at $z > 5$ was discovered by van Breugel et al. (1999) at $z = 5.19$, a distance record that was only recently broken by our discovery of a radio galaxy at $z = 5.72$, which is part of this thesis (Saxena et al. 2018a).

Higher sensitivity radio surveys covering larger areas on the sky were discovering orders of magnitude more radio sources, with most of them being low-redshift radio galaxies hosted by ellipticals. The increasing number of radio sources were making dedicated spectroscopic follow-up an expensive exercise. Techniques had to be developed to isolate candidate high-redshift radio galaxies (HzRGs) from these surveys. Miley & De Breuck (2008), in their extensive review of the properties of HzRGs highlight the most commonly used and arguably the most successful selection steps to isolate HzRGs from large radio surveys. In the following we highlight some of the most commonly used and also successful selection techniques for HzRGs.

1.2.1 Selection techniques

Radio colours and spectral indices

The first selection that is often applied to large radio datasets to pick out promising HzRG candidates is to use radio colours or spectral indices to filter out low-redshift radio sources. Radio sources at high-redshifts have been found to exhibit steeper values of the radio spectral index, α, which is defined as $S_\nu \propto \nu^\alpha$, where S_ν is

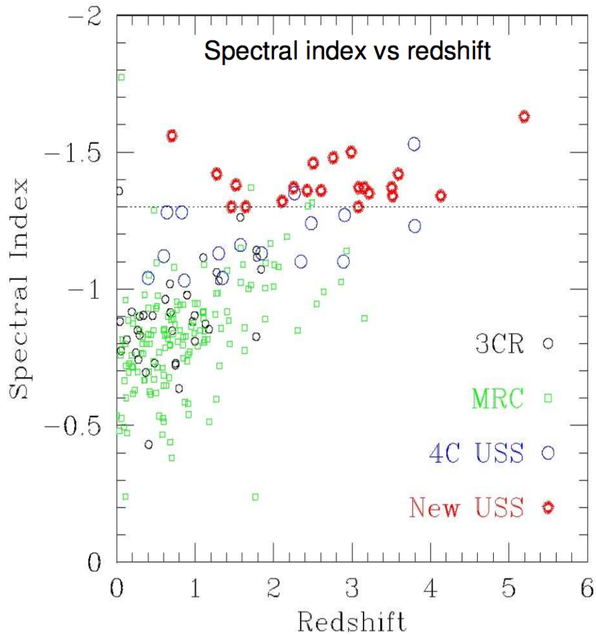

Figure 1.3: The empirically derived correlation between redshift and radio spectral index from De Breuck et al. (2000a). Studies of complete samples have shown that radio sources with steeper spectral indices tend to be at higher redshifts. This has led to the ultra-steep spectrum (USS) selection technique being widely used to shortlist potential HzRGs from large radio datasets.

the flux density at an observing frequency ν. This effect was first investigated by Blumenthal & Miley (1979) and Tielens et al. (1979), where they found that the optical identification fraction in flux limited surveys for steeper spectrum radio sources was lower. Optical faintness serves as a proxy for distance and the lower identification fraction suggested that radio sources with steeper spectral indices are more distant. In Figure 5.10 we show the empirically derived correlation between redshift and spectral index, also known as the $z - \alpha$ correlation, taken from De Breuck et al. (2000a).

Angular size restrictions

The next step is to apply an angular size cut. The motivation to do this largely stems from the observed statistical decrease in angular sizes of radio sources at high redshifts (Miley 1968). This effect was initially observed for radio-loud quasars, but it was soon discovered that extended radio galaxies display such behaviour too (Nilsson et al. 1993). Besides simple geometry, the main reason why sizes of radio sources are expected to decrease at higher redshifts is due to a systematic increase in the density of the ambient medium surrounding these radio galaxies (Barthel & Miley 1988). The higher energy density of the surroundings makes it more difficult for radio jets to grow out to large distances because of increased thrust of radio jets against the ambient medium. Moreover, the substantial increase in the energy density of the cosmic microwave background radiation, that increases as $\propto (1+z)^4$, leads to enhanced inverse Compton losses, extinguishing radio sources earlier in their lifetimes, leading to a statistical decrease in their sizes (Krolik & Chen 1991; Daly 1992).

Optical/infrared faintness

The next step to filter out low-redshift galaxies from a radio survey is to first accurately match the radio data with available optical and infrared data. Once optical/infrared counterparts for radio sources have been identified, the brighter sources may be discarded as they are likely to be lower redshift radio galaxies. The justification of targeting fainter optical/infrared radio sources for spectroscopic follow-up originates from the discovery by Lilly & Longair (1984) that radio galaxies across all redshifts tend to be dominated by an older stellar population, and reside in giant elliptical-like galaxies. This gives rise to a tight correlation between their near-infrared magnitude where light from old stars dominates, and the host galaxy redshift. As a result, near-infrared imaging specifically using the K band was found to be very effective at identifying counterparts of radio sources (see Jarvis et al. 2001b, for example). The same is not true for bluer wavelengths, however, especially at higher redshifts. Lilly & Longair (1984) found substantial deviations at high redshifts for optical to infrared colours, with reported excess of ultraviolet light which they attributed to bursts of star formation.

At very high redshifts ($z \gtrapprox 3$), when the rest frame ultraviolet light redshifts into the optical wavelengths, the 'Lyman break' selection technique may be employed to select high-redshift radio galaxy candidates. This selection essentially relies on the break in the spectrum of a star-forming galaxy produced due to almost complete absorption of radiation by the neutral gas around star-forming regions at wavelengths blueward of the Lyman limit (at 912 Å) (see Steidel et al. 1995, for example). This kind of selection relies on the availability of very deep photometry ($i \gtrapprox 25$ AB) in multiple optical bands, which is hard to achieve over very large areas of the sky (100s of square degrees), the kind of areas that are typically covered by radio surveys. For the largest area radio surveys, it is common practice to identify as promising HzRG candidates only those radio sources that have no optical and/or infrared counterparts in the available all-sky optical and infrared surveys, such as *SDSS* (Alam et al. 2015a), *Pan-STARRS* (Chambers et al. 2016a), *UKIDSS* (Lawrence et al. 2007a) and *WISE* (Wright et al. 2010a).

1.2.2 Follow-up of promising candidates

Once a sample of promising HzRG candidates has been compiled largely following the above mentioned selection criteria, it is then necessary to follow them up at various wavelengths, mainly for spectroscopic redshift measurements but also to study the underlying stellar populations and their environments.

Dedicated deep near-infrared imaging of promising HzRG candidates using the K band filter is an effective way of identifying their host galaxy, as mentioned earlier. Once the host galaxy has been identified or its expected position has been localised, a spectrum may be obtained by placing a long-slit at the appropriate location. Blind spectroscopy at the radio positions has proven to be successful at identifying emission lines originating from the radio galaxy host (see Spinrad 1982, for example). In the future, dedicated integral-field unit (IFU) spectroscopy of promising candidates, which gives a spectrum at every pixel, may help overcome the positional uncertainties that arise due to the lower resolution of radio surveys and could be employed as an effective tool for redshift determination of radio sources.

Once the redshift of a radio source has been determined, it can be followed up at various other wavelengths to shed light on the different physical processes that are underway in distant radio galaxies. In the following Section we first briefly describe the physics of radio and line emission from radio galaxies and then highlight the underlying physical processes that are probed when observing HzRGs at different wavelengths.

1.3 Physics of Radio-loud AGN

In this section, we will briefly describe the key physical processes that are believed to power the large radio lobes originating from AGN and the bright emission lines seen in the ultraviolet, optical and infrared spectra of high-redshift radio galaxies. We will then provide an overview of the pan-chromatic properties of HzRGs and describe the various physical processes that can be probed at different observing wavelengths.

1.3.1 Powering the radio emission

Some of the earliest models to explain the bright radio emission observed from AGN followed the idea that accretion on to the central black hole in an AGN can give rise to twin jets that are perpendicular to the accretion disk and are capable of accelerating particles to relativistic speeds (Blandford & Rees 1974; Scheuer 1974). The presence of strong magnetic fields around the AGN would give rise to radio emission both from the core of the AGN and from the collimated jets (Blandford & Payne 1982). The production of charged particles in the vicinity of the AGN that can then be electromagnetically transported to the poles of the rotating black hole and get accelerated in the jets came to be known as the Blandford-Znajek process (Blandford & Znajek 1977).

Once the jets emanating from the AGN are powered, semi-analytical models describing the growth of FRII type radio sources (as discussed in Section 1.1) can be implemented. These models were primarily constructed to track the growth of radio sources and energy losses due to several physical mechanisms that dominate at different stages of a radio source's lifetime (Kaiser & Alexander 1997; Kaiser et al. 1997; Blundell et al. 1999). The typical lifetime of a radio-loud AGN is $\sim$ 100 Myr (Wan et al. 2000) and the key processes that dominate through the lifetime of a radio AGN are: (i) synchrotron emission in the early stages of radio AGN evolution that also give rise to the power-law behaviour of the low-frequency SED, (ii) adiabatic losses when the jet reaches galactic scales and beyond and finally, (iii) inverse Compton losses due to interaction with the cosmic microwave background (CMB) photons at much larger scales. These processes can be implemented in a cosmological framework using semi-analytical prescriptions and can then be used to estimate the distribution of luminosities, ages and sizes of radio sources at different epochs (see Kaiser & Best 2007, for example).

1.3.2 Powering the rest-frame optical/NIR emission lines

Radio AGN produce a number of rest-frame optical and infrared emission lines. Broadly, a distinction between the emission line spectra exhibited by HzRGs can be made based on the widths of the lines. Classical HzRGs typically exhibit narrow emission lines (FWHM < 2000 km s^{-1}), McCarthy (1993) found that only $\sim 15\%$ of HzRGs show broad emission lines, that are more commonly found in radio-loud quasars where the broad-line region close to the accreting black hole is directly visible. A detailed review of emission lines from HzRGs is presented in McCarthy (1993), and a composite HzRG spectrum presented in this study is shown in Figure 1.4. There are a number of strong emission lines visible in a HzRG spectrum that can be used to infer several important properties about the AGN and the host

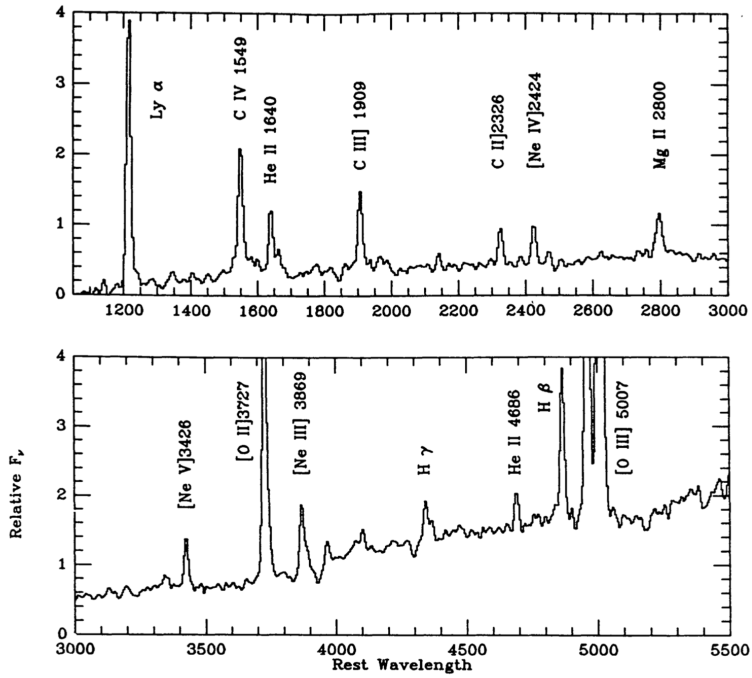

Figure 1.4: Composite HzRG spectrum at rest-frame UV and optical wavelengths, taken from McCarthy (1993). A wide range of broad and narrow emission lines are detected in HzRGs and comparing the line ratios can give insights into the underlying ionising mechanisms.

galaxy, such as ionisation state, metallicity, star-formation rates, etc.

Several ionisation mechanisms have been proposed to explain the observed emission lines. The most direct way to constrain the underlying ionisation mechanism is to compare emission line ratios. McCarthy (1993) found that simple photoionisation models from an AGN spectrum following a power law $\nu^{-1.5}$ were enough to explain the line ratios observed in a large majority of radio galaxies. However, Villar-Martin et al. (1997) showed that the contribution from shocks, which lead to interaction between the radio jet and the line-emitting gas, must also be taken into account when modelling radio galaxy spectra, especially at high redshifts. Best et al. (2000) further showed that for smaller radio sources, shock ionisation due to the radio jet becomes important in explaining the observed spectra. The emerging picture is that in small radio sources the jet is traversing the intergalactic medium of the host galaxy and the shocks associated with the radio jet dominate the ionisation and the kinematics of the emission line gas. In larger radio sources, the shock has passed beyond the line emitting regions and the observed line ratios and kinematics can be explained using simple photoionisation models.

The impact of radio size on the kinematics of the Lyα emission line from HzRGs was shown by van Ojik et al. (1997), where they found that smaller radio sources showed broader Lyα emission lines. This behaviour was again attributed to the interaction between line emitting gas and the radio jet in small radio sources. This result is particularly important for studies of radio galaxies at the highest redshifts, where the rest-frame optical lines are redshifted into the infrared and are harder to observe. However, near-infrared intergral-field spectroscopy of nebular lines for a subsample of the most distant radio galaxies showed complex emission line kinematics, which arise from jet-driven AGN winds and outflows at high redshifts (Nesvadba et al. 2008, 2017).

1.4 A panchromatic view of high-redshift radio galaxies

Having briefly introduced the physics that power the radio emission and the emission lines from gas in radio galaxies, we now discuss the various physical processes that can be studied at different observing wavelengths. Radio galaxies, especially at high redshifts, show remarkable features at almost every wavelength and the relationships and interactions between these constituents make HzRGs excellent probes of galaxy formation and evolution in the early Universe. A lot of the discussion that will follow is derived from the excellent review by Miley & De Breuck (2008). We add in some of the latest observations wherever applicable to sketch a complete picture about HzRGs and their environments. We group the discussion that follows by observing wavelength and then explain the physical processes that contribute to the observed emission at that wavelength. The spectral energy distribution (SED) across a wide range of wavelengths for a radio galaxy at $z = 2.5$, taken from Miley & De Breuck (2008), is shown in Figure 1.5.

1.4.1 Radio

As mentioned already, the bulk of the radio emission observed at low frequencies is powered by non-thermal synchrotron emission emitted by relativistic plasma being accelerated by the central AGN or at the hotspot created by the interaction of the radio jet and the ambient medium, that usually follows a single power law. This single power-law SED is then acted upon by various energy loss processes, such as spectral ageing that affects the radio SED at the high frequencies (Harwood et al. 2013, and references therein) and synchrotron self-absorption at the low frequencies (Callingham et al. 2015, and references therein). As a result, depending on the

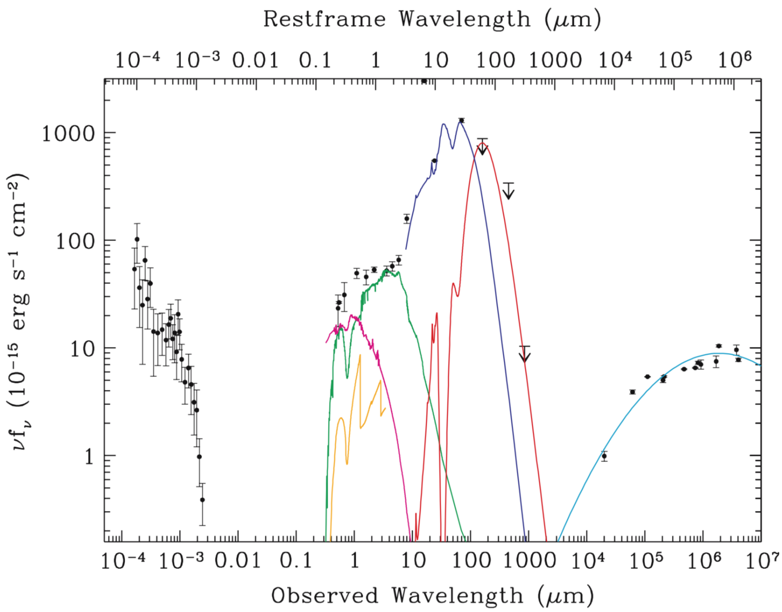

Figure 1.5: A pan-chromatic view of the spectral energy distribution of the HzRG 4C 23.56 at $z = 2.5$, taken from Miley & De Breuck (2008). The solid lines indicate best fitting models to the observations, starting from the highest energies (shortest wavelengths), Black: non-thermal X-ray radiation from the AGN, Green: light from old stars, Yellow: nebular continuum, Magenta: scattered quasar light, Blue: thermal dust emission heated by AGN, Red: thermal dust emission heated by star-bursts, Cyan: radio synchrotron emission.

age and the environment of the radio source, deviations from a single power-law emerge and the SED of radio sources can vary almost on a case by case basis.

1.4.2 Ultraviolet/optical/near-infrared

Studies of radio galaxies at $z > 2$ have shown that the rest-frame ultraviolet (UV) radiation in HzRGs has a strong contribution from light from young stars, but the stellar light is often not enough to account for the total rest-frame UV emission. A significant fraction of the contribution could be attributed to non-stellar emission, such as from an obscured AGN (see Cimatti et al. 1998, for example) or from free-free emission. As discussed already, the UV-optical emission lines shed light on the state of the warm ionised gas and help study properties such as temperature, density, metallicity, ionisation and kinematics of ionised gas. The UV-optical absorption lines probe the cooler atomic gas. The cool atomic gas can also be probed using HI absorption at radio wavelengths (Morganti et al. 2006). At high redshifts

($z > 1.5$), the strong Lyα emission line typically observed in radio galaxy spectra is redshifted into the visible wavelengths, offering an easy way to spectroscopically confirm redshifts of radio sources.

The optical-near infrared (NIR) continuum probes the old stars and is sensitive to the age and formation epoch of the host galaxy (Lilly & Longair 1984). Radio galaxies across all epochs tend to be dominated by an old stellar population (Rocca-Volmerange et al. 2004), which explains the observed correlations between K band magnitudes and redshifts for HzRGs (Jarvis et al. 2001b; Willott et al. 2003). The nebular emission-lines at optical wavelengths have also been used to quantify the excitation state of gas in the radio galaxy, leading to distinct populations of high-excitation and low-excitation radio galaxies (HERGs and LERGs; Best & Heckman 2012). Additionally, emission line ratios are often used to study the nature of the ionising source, as discussed in the previous section.

1.4.3 Mid-infrared/far-infrared/sub-mm

Continuum emission at the mid- to far-infrared wavelengths all the way to sub-mm wavelengths is dominated by thermal dust emission, heated by both the AGN and star-formation activity (van der Werf 1999; Reuland et al. 2004; Seymour et al. 2008). The mid-IR colours of HzRGs have shown that they lie in a similar region as unobscured AGN, and their mid-IR luminosities classify most of them in the category of luminous infrared galaxies (LIRGs) (see Seymour et al. 2007, for example). Observations of HzRGs at 450/850 μm have revealed dust masses of the order of $\sim 10^8\ M_\odot$ and temperatures of $\sim$ 50 K (see Reuland et al. 2004, for example). Although the dust could be heated either by X-rays from the AGN or UV photons from young stars, it is not easy to distinguish one source from the other.

The sub-mm emission lines probe the vast reservoirs of molecular gas, in addition to the dust that is typically present in HzRGs (Emonts et al. 2014, 2016). This molecular gas forms the fuel for intense star-formation activity that is observed in many HzRGs. However, recently **?** showed that the star-formation rates inferred from sub-mm observations of HzRGs may be overestimated, as there may be significant contribution from synchrotron emission extending to these wavelengths. This would mean that hosts of radio AGN lie below the main sequence of star-forming galaxies and many HzRGs may be quenched.

1.4.4 X-rays

Thermal X-ray continuum observations of HzRGs seem to predominantly trace the hot ionised gas that is heated by shocks propagated through the relativistic jets emanating from the AGN, which can often extend to large scales (few 100 kpc) around the central AGN (Carilli 2003; Belsole et al. 2007). Additionally, non-thermal emission from inverse Compton (IC) scattering produced by the same relativistic electron population that contributes to the synchrotron emission is also seen in the X-rays (Schwartz 2002). These components can be seen in blue in Figure 1.2 for a low-redshift radio galaxy. In principle, the energy density of the cosmic microwave background responsible for IC emission increases as $(1+z)^4$ compensates for the $(1+z)^{-4}$ decrease in surface brightness, which should make it possible to detect non-thermal X-rays out to higher redshifts (Schwartz 2002).

1.5 Cosmological properties of high-redshift radio galaxies

Having established that HzRGs are exotic objects with a number of physical phenomena visible at various wavelengths, we now turn our attention towards the cosmological implications of HzRGs. HzRGs were initially used as beacons for finding the most distant objects in the Universe and were later found to be surrounded by dense environments. Below we briefly summarise the currently known cosmological properties of HzRGs and their environments.

1.5.1 Number density at high redshifts

Radio galaxies are some of the rarest objects in the Universe. Dunlop & Peacock (1990) reported a rise in the space density of HzRGs compared to the local Universe, with a peak observed around $z \sim 2$. They tentatively observed a decline in their space densities between redshifts of 2 and 4, which other studies have subsequently confirmed (Jarvis et al. 2001a; Rigby et al. 2011, 2015). This behaviour makes radio galaxies at the highest redshifts even rarer, leading to great challenges in identifying and confirming them. Overall, the space density evolution as a function of redshift is very similar to the redshift evolution of the space densities of quasars (see Fan et al. 2004, for example). To further highlight the rarity of HzRGs, only ~ 200 radio galaxies are currently known at $z > 2$ (Miley & De Breuck 2008), which when compared to the number of star-forming galaxies known at $z > 2$ is a minuscule number.

1.5.2 Formation and evolution of massive galaxies across cosmic time

Radio galaxies across a broad range of redshifts form a fairly narrow sequence across the Hubble $K - z$ diagram (Lilly & Longair 1984). Rocca-Volmerange et al. (2004) found that radio galaxies are some of the most massive galaxies at any given epoch in the redshift range $z = 0 - 4$ using detailed stellar population modelling. However, deriving stellar masses from near-infrared photometry has a number of caveats (Miley & De Breuck 2008). First, the K band photometry can often be contaminated by a warm dust component which must be appropriately accounted for. Second, at certain redshifts the K band flux may be contaminated by strong emission lines, which would lead to an overestimation of the stellar mass. Using space based observatories, such as *Spitzer*, that help probe the rest frame infrared wavelengths, Seymour et al. (2007) were able to successfully decompose the optical to infrared SEDs of HzRGs to properly account for the light emitted by old stars. They found that once contaminants are accounted for, a large majority of radio galaxies have stellar masses in the range $10^{10} - 10^{11}\ M_{\odot}$ even at the highest redshifts ($z \sim 4$), putting radio galaxies truly at the most massive end of the galaxy stellar mass function across cosmic time. Therefore, studies of the cosmological evolution of radio galaxies offer a way to understand the physical processes that help shape the most massive galaxies in the Universe.

1.5.3 AGN feedback

The close correlations observed between the supermassive black hole (SMBH) mass and the velocity dispersion of bulges of massive galaxies has shown that the growth of the SMBH directly influences and regulates the growth of the host galaxy (Kormendy & Gebhardt 2001; Merritt & Ferrarese 2001). Therefore, thermal and kinematic feedback from AGN, or simply AGN feedback, must play an important role in galaxy evolution. Without heating of the intergalactic medium through AGN feedback, the Brightest Cluster Galaxies (BCGs), the massive galaxies that reside in the centres of clusters, would encounter runaway star formation through accretion of cold gas and would appear to be even more massive. These BCGs are almost always associated with radio galaxies (see Hogan et al. 2015, for example), showing studies of radio galaxies and their environments are essential to understand the physics of AGN feedback and its impact. For an in-depth review of the observational evidence of AGN feedback, we direct the readers to Fabian (2012).

To match models to the observed distribution of galaxy stellar masses (the galaxy stellar mass function) over redshifts, proper understanding of the feedback physics is essential. At lower stellar masses, feedback from supernovae going off in star-forming regions is enough to heat the gas or move it away through winds, thereby terminating star-formation and regulating the growth of lower mass galaxies. In the most massive galaxies that harbour massive SMBHs, the process of quenching star-formation is undertaken by AGN feedback. Owing to limitations in resolution, state-of-the-art cosmological simulations such as EAGLE (Schaye et al. 2015) rely on calibration of sub-grid physics involving AGN feedback efficiency (Wagner et al. 2012, and references therein) to accurately reproduce the galaxy stellar mass function in the local Universe. To enable modelling of these sub-grid physics from first principles in future simulations, achieving a complete understanding of the role played by AGN feedback in regulating galaxy growth is crucial. A statistically significant sample of radio galaxies and observations of their environments across a broad range of redshifts would help understand this process.

1.5.4 Large scale structure formation

As mentioned in the previous section, radio galaxies are often found at the centres of massive galaxy clusters at low redshifts. From a cosmological point of view, galaxy clusters are crucial to tracing the formation of the most massive dark matter halos, galaxies and supermassive black holes (see Springel et al. 2005, for example). In hierarchical structure formation models, small gravitational instabilities in the early Universe eventually lead to the formation of structure at the largest scales, leading to the emergence of clusters and super-clusters of galaxies in the present day Universe. Therefore, studying the growth and evolution of clusters of galaxies across cosmic time can shed light on the large-scale structure formation history of the Universe. Additionally, the role that a galaxy's environment plays on its evolution requires statistical studies of over-dense regions at high redshifts. Observations of galaxy clusters and proto-clusters also serve as a tool to test fundamental cosmological parameters using simulations, by comparing their number densities, masses and density profiles at different redshifts (Overzier 2016).

Even at high redshifts, radio galaxies are found to lie in the centres of over-dense regions (Pentericci et al. 2000; Venemans et al. 2002, 2007; Overzier et al. 2006; Hatch et al. 2011). Through the Clusters Around Radio-loud AGN (CARLA) survey, Hatch et al. (2014) confirmed that radio galaxies are likely to lie in the centres of clusters and proto-clusters across redshifts. A prime example of a radio galaxy at high redshift, situated in an over-dense environment, orchestrating the formation of proto-clusters is MRC 1138−262, also referred to as the 'Spiderweb Galaxy' (Miley et al. 2006) which is shown in Figure 1.6. The UV/optical image shows numerous satellite galaxies orbiting and merging with the central radio galaxy, which will eventually evolve to become a dominant cluster galaxy, like those observed in clusters in the local Universe. Hunting for bright radio galaxies at higher redshifts is the best way to spot over-dense regions in the early Universe and constrain the growth of these over-densities across cosmic time, testing hierarchical structure formation models.

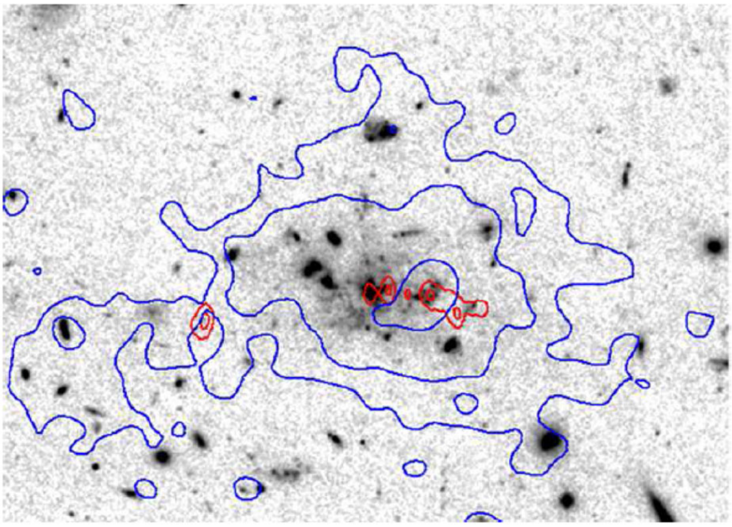

Figure 1.6: Deep HST image of MRC 1138−262, also known as the 'Spiderweb Galaxy' at $z = 2.2$, which is a quintessential example of a proto-cluster surrounding a radio galaxy (Miley et al. 2006). Superimposed on the image are Lyα contours (blue) and radio 8 GHz contours (red). The image shows almost 10 star-forming satellite galaxies in the process of merging with the progenitor of what would go on to become a dominant cluster galaxy in the centre.

1.5.5 Probes of the epoch of reionisation

At $z \geqslant 6$, into the epoch when the Universe was making a phase transition from neutral to completely ionised, bright radio galaxies have the potential to be unique probes of this important cosmological event. At $z \approx 1100$, roughly 400,000 years after the Big Bang, electrons and protons were decoupled from photons, leaving behind a signature in the form of the cosmic microwave background radiation (CMB). As the Universe cooled further, the electrons and protons combined to form neutral hydrogen atoms that pervaded the Universe, giving rise to the so-called 'Dark Ages'. Once the Universe was cool enough for stars and galaxies to start forming, their was light in the Universe and these sources of ultraviolet radiation started ionising the neutral hydrogen around them (Zaroubi 2013). There are many observational signatures showing that the process of reionisation of the Universe was more or less complete by $z \approx 6$. The most important of these are the observations of the Gunn-Peterson trough in the spectra of $z > 6$ quasars (see Becker et al. 2001, for example), which almost completely suppresses flux blueward of the Lyman α line due to absorption by intergalactic neutral hydrogen, an effect that was first predicted by Gunn & Peterson (1965). The fine details about when the pro-

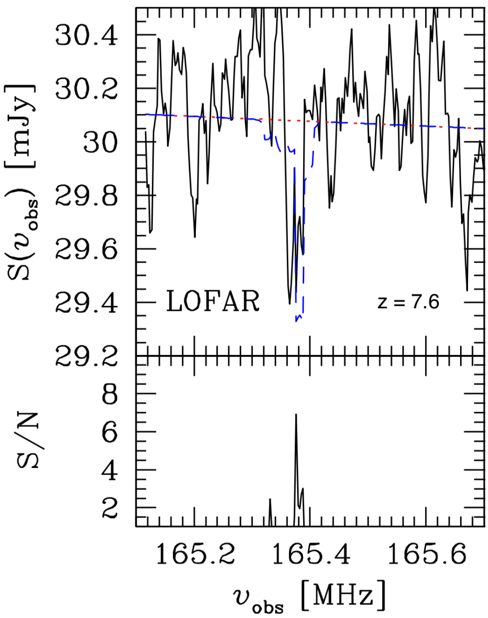

Figure 1.7: Simulated spectrum of a ~ 30 mJy radio source at $z = 7.6$ showing a 21cm absorption feature (Ciardi et al. 2015) from the neutral hydrogen in the intergalactic medium. This simulation shows results with 1000 hours of integration time on LOFAR. The absorption at slightly different wavelengths due to neutral hydrogen clouds in the line-of-sight can give rise to a 21cm forest, which can be studied to constrain the reionisation process over time.

cess of reionisation started and unfolded, and which were the primary sources that drove this process (star-forming galaxies or AGN?) are still unknown and pose an exciting challenge in observational Cosmology today.

One diagnostic that offers the best chance of directly observing the neutral hydrogen at $z > 6$ is the 21cm hyperfine transition line of neutral hydrogen. At $z > 6$, this line is redshifted into the low radio frequency regime ($v_{\rm obs} < 200$ MHz), which can potentially be observed as absorption signals in the spectra of luminous background radio sources that illuminate the line-of-sight (Carilli et al. 2002b). Such a signal is principle observable by the Low Frequency Array (LOFAR; van Haarlem et al. 2013), as shown by Ciardi et al. (2015) and also in Figure 1.7. For a bright radio source at $z > 6$, the radio emission may be absorbed by patches of neutral hydrogen populating the line-of-sight, giving rise to a 21cm forest, similar to the Lyman α forest that is observed in the UV spectra of bright high-redshift quasars.

The biggest challenge at the moment is finding a bright radio source at $z > 6$.

As mentioned earlier, the space density of radio sources decreases dramatically at high redshifts and it is unclear whether bright radio galaxies exist at all at $z > 6$. The detection of distant radio galaxies formed the main motivation behind this thesis, and in the next section we highlight the steps taken through this thesis towards bringing us just a little closer to the epoch of reionisation, as far as radio galaxies are concerned.

1.6 This thesis

The main goal of this thesis is to take advantage of the newer, deeper radio surveys of the sky at low frequencies and detect massive radio galaxies close to or even into the epoch of reionisation, and understand better the physics of galaxy formation and evolution as well as the implications for the reionisation of the Universe. To gain an overall understanding of very distant radio galaxies, this thesis contains a combination of theoretical work, observational work at radio, optical and infrared wavelengths as well as some modelling to interpret those observations. The observations presented in this thesis have been taken from a number of state-of-the-art facilities around the world, namely the *Karl G. Jansky Very Large Array (VLA), William Herschel Telescope (WHT), Large Binocular Telescope (LBT), Gemini North Telescope, Hobby-Eberly Telescope (HET), Gran Telescopio Canarias (GTC)* and the *Very Large Telescope (VLT)*. Below we provide a short description of each chapter of this thesis.

In **Chapter 2** we model the growth of radio sources to predict the expected number of bright radio galaxies at $z \sim 6$, which could be used as effective probes of the epoch of reionisation. We begin by constructing a model that uses masses of supermassive black holes, their accretion rates and spins to calculate jet powers and associated radio luminosities. As these radio sources grow, they lose energy due to various physical processes, the prescriptions for which we put into our model. Running the model for a certain period of time at any epoch, we can predict the space density distribution of radio sources, i.e. the radio luminosity function, along with the distribution of radio source sizes. We first test our model at $z = 2$, where ample radio data is available and show that our predictions match the observations well. We then run our model at $z = 6$ and predict the radio luminosity function and radio size distribution for galaxies at this redshift. We then use this information to define best observing strategies that would help maximise the number of $z = 6$ radio galaxies detected (essentially a coverage area vs. depth trade-off), in a bid to address the first major question faced by studies of distant radio galaxies: ***How many radio galaxies actually exist at*** $z \geqslant 6$ ***and how to find them?***.

In **Chapter 3** we present initial results from an observational campaign to discover fainter radio galaxies across all redshifts. Promising faint high-redshift radio galaxy candidates were selected at 150 MHz using the selection techniques mentioned earlier in this Introduction. For the final sample of 32 promising candidates, we present high-resolution radio observations using the VLA. We also present the overall optical and infrared properties of the sample, and determine photometric redshifts for a handful of sources that have deeper photometry at optical/IR wavelengths. We present radio properties of the sample, including whether the low-frequency radio spectra show signs of curvature, which is often seen in HzRGs. We also report the serendipitous discovery of a giant radio galaxy (GRG) with a photometric redshift of 1.8 ± 0.5. This chapter addresses the question: ***How successful can deeper radio surveys be at identifying distant radio galaxies?***

In **Chapter 4** we present results from a spectroscopic campaign to confirm the redshifts of promising candidates presented in Chapter 3. We are able to identify radio galaxies across a range of redshifts that are almost an order of magnitude fainter in radio luminosity than those previously discovered. We also present near-infrared imaging for of a subset of these confirmed sources to estimate their stellar masses. Next, we select known $z \geqslant 2$ radio galaxies from the literature and add our newly discovered galaxies to form an extended HzRG sample. We then look at the radio and emission line properties of this extended sample, find correlations between many of these properties and introduce scenarios that address open questions surrounding AGN feedback at high redshift. This chapter addresses the question: ***What is the nature of radio galaxies located at the highest redshifts?***

In **Chapter 5** we report the discovery of the most distant radio galaxy known to date, TGSS J1530+1049 at $z = 5.72$, which is very close to the presumed end of the epoch of reionisation. This galaxy was initially selected as a promising radio source in Chapter 2 and subsequent spectroscopic observations and near-infrared photometry helped confirm its high redshift. This discovery breaks the previous record of the most distant radio galaxy, which had been held for almost 20 years. In this Chapter we present a detailed analysis of the Lyα emission line from the host galaxy and how its Lyα and radio properties (such as luminosity and size) compare with other radio sources at high redshifts as well as ‘non-radio’ galaxies at a similar redshift. We also set estimates on the stellar mass of the host galaxy and show that TGSS J1530+1049 must be a very young radio source. This Chapter takes the first step towards addressing the question: ***How does a radio galaxy very close to the epoch of reionisation look like?***

1.7 Outlook

Radio astronomy is currently undergoing a Renaissance, with state-of-the-art radio telescopes such as the *Low Frequency Array (LOFAR)* and in the near future, the *Square Kilometer Array (SKA)*, that will provide larger sky coverage, higher sensitivities and better angular resolutions over large areas on the sky. These new datasets will open up new parameter spaces that will be used to detect fainter radio galaxies at the highest redshifts. The challenge still remains to detect a radio galaxy at $z > 6$ to enable studying the epoch of reionisation in unparalleled detail, and these new radio surveys are expected to detect a number of such sources. Detection of distant radio galaxies will be especially aided by large area surveys at the lowest frequencies, such as the LOFAR LBA survey at 60 MHz. The advantages of going down to lower radio frequencies are: (i) owing to the steepness of the radio spectral index of HzRGs, they should be much easier to detect at low frequencies, and (ii) a flux density point at lower frequencies will enable additional selection criteria, that do not necessarily rely on the steepness of the spectral indices but can also take advantage of spectral curvature that is characteristic of radio galaxies at the highest redshifts.

From a multi-wavelength point of view, the deeper all-sky optical and infrared surveys using telescopes such as the *Large Synoptic Survey Telescope (LSST)*, *Euclid* and *Wide Field Infrared Survey Telescope (WFIRST)* would enable the identification of the host galaxies of an increasingly large number of radio sources. Additionally, this deeper ancillary data would accelerate searches for the most distant radio AGN as well as their host galaxies and environment. The highly accurate photometric redshifts derived from these surveys would enable studying the redshift evolution of large samples of radio galaxies to higher redshifts, without the explicit need for spectroscopically confirming each of them. For the highest redshift sources, the *James Webb Space Telescope (JWST)* would enable deep near-infrared spectroscopy, shedding light on the ionising mechanisms, the interactions of jets with the ambient interstellar media in host galaxies as well as constraining feedback processes in powerful AGN in the early Universe. Current generation facilities such as the *Atacama Large Millimeter Array (ALMA)* are already enabling studies of molecular gas and outflows at the highest redshifts in a bid to constrain the role played by AGN feedback, and the *Next Generation Very Large Array (ngVLA)* will help probe the cold gas in AGN to even higher redshifts and sensitivities.

The future of detailed studies of radio galaxies at the highest redshifts seems bright.

2 Modelling the luminosities and sizes of radio sources: radio luminosity function at z = 6

We present a model to predict the luminosity function for radio galaxies and their linear size distribution at any redshift. The model takes a black hole mass function and Eddington ratio distribution as input and tracks the evolution of radio sources, taking into account synchrotron, adiabatic and inverse Compton energy losses. We first test the model at $z = 2$ where plenty of radio data is available and show that the radio luminosity function (RLF) is consistent with observations. We are able to reproduce the break in luminosity function that separates locally the FRI and FRII radio sources. Our prediction for linear size distribution at $z = 2$ matches the observed distribution too. We then use our model to predict a RLF and linear size distribution at $z = 6$, as this is the epoch when radio galaxies can be used as probes of reionisation. We demonstrate that higher inverse Compton losses lead to shorter source lifetimes and smaller sizes at high redshifts. The predicted sizes are consistent with the generally observed trend with redshift. We evolve the $z = 2$ RLF based on observed quasar space densities at high redshifts, and show that our RLF prediction at $z = 6$ is consistent. Finally, we predict the detection of 0.63, 0.092 and 0.0025 $z \geqslant 6$ sources per sq. degree at flux density limits of 0.1, 0.5 and 3.5 mJy. We assess the trade-off between coverage area and depth and show that LOFAR surveys with flux density limits of 0.1 and 0.5 mJy would are the most efficient at detecting a large number of $z \geqslant 6$ radio sources.

Based on:
Saxena A., Röttgering H.J.A. and Rigby E.E.
MNRAS, 469, 4083 (2017)

2.1 Introduction

Powerful high redshift radio galaxies (HzRGs) are found to reside in massive galaxies, which are thought to be progenitors of the massive ellipticals that we observe today (Best et al. 1998a; McLure et al. 2004). These host galaxies contain huge amounts of dust and gas, and are observed to be forming stars intensively (Willott et al. 2003). HzRGs are also associated with cosmological over-densities such as galaxy clusters and proto-clusters (Röttgering et al. 2003; Stevens et al. 2003; Kodama et al. 2007; Venemans et al. 2007; Galametz et al. 2012; Mayo et al. 2012). These properties make HzRGs important tools to study the formation and evolution of massive galaxies and large-scale structure in the universe. For a review about the nature and properties of HzRGs, their hosts and their environments, we refer the reader to Miley & De Breuck (2008).

Radio galaxies at the highest redshifts, particularly in the Epoch of Reionisation (EoR), have the potential to be important probes of cosmology. Constraining when and how the universe made a phase transition from neutral to completely ionised is one of the most exciting challenges in cosmology today and luminous radio galaxies at $z \geqslant 6$ may hold some clues on how this process unfolded. Evidence of the inter-galactic medium (IGM) being partly neutral at early times is found in the observed Gunn-Peterson trough (Gunn & Peterson 1965) in the spectra of $z \geqslant 6$ quasars (Becker et al. 2001). A robust signature of the neutral gas in the IGM could in principle be observed by measuring the hyperfine transition line of ground-state neutral hydrogen (with a rest-frame wavelength of 21 cm). At $z \geqslant 6$, this line falls in the low-frequency radio regime ($\nu < 200$ MHz) and may be detected as an absorption feature in the radio spectra of $z \geqslant 6$ radio galaxies and quasars (Carilli et al. 2002b; Furlanetto & Loeb 2002). Observing a 21-cm forest (similar to a Ly-α forest) in the continuum of a $z > 6$ radio source can enable studying the process of reionisation over cosmic time (Xu et al. 2009; Mack & Wyithe 2012; Ewall-Wice et al. 2014; Ciardi et al. 2015). Additionally, studying bright radio sources at $z \geqslant 6$ will further help understand the physics behind radiative processes responsible for ionising the universe.

As radio galaxies are often associated with some of the most massive supermassive black holes (SMBHs), HzRGs can be used to constrain black hole growth models. Understanding the growth of SMBHs over cosmic time using observations of active galactic nuclei (AGN) has been a subject of intense study. The growth of the black hole mass function has been studied using AGN and quasar luminosity functions and varying key parameters associated with AGN such as SMBH accretion rate, AGN duty cycles and radiative efficiencies (Shankar et al. 2009; Kelly et al. 2010; Shankar et al. 2013). Willott et al. (2010b) managed to extend studies out to $z = 6$. However, most observations used to study SMBH growth are at optical, infrared and Xray wavelengths. Not many AGN at high redshifts have been observed to be luminous at radio wavelengths and this could partly be due to a lack of deep, all-sky radio surveys. The general understanding, however, is that radio emission is powered by the same mechanism that is also responsible for the optical/IR and Xray emission from AGN, the accretion of material on to the central SMBH.

Many attempts have been made to measure the evolution of the radio luminosity function (RLF). Dunlop & Peacock (1990) reported evidence for the existence of a redshift cut-off in the space density of quasars and radio galaxies over the redshift range $2 - 4$. Subsequent studies also indicated that space densities of radio sources undergo continued decline between $z \simeq 2.5$ and 4.5 (Jarvis et al. 2001b). This is similar to what optical studies of quasars have revealed, i.e. a peak in space density between redshifts 1.7 and 2.7 (Schmidt et al. 1995) and a decline at higher redshifts (Fan et al. 2004). A decline in space density at $z > 2.5$ was also reported in radio studies of flat spectrum quasars (Wall et al. 2005). Further, studies of X-ray selected AGN have shown that the space density of luminous AGN peaks between $z \sim 2$ (Hasinger et al. 2005) and $z \sim 2.5$ (Silverman et al. 2005). More recently, Rigby et al. (2011) used radio data available in the literature at the time to study the density evolution of steep-spectrum sources and found the redshift evolution of space densities to be dependent on luminosity. They found that the redshift at which space density of AGN with higher radio luminosities peaks, $z_{\rm peak}$, is higher, thereby demonstrating that $z_{\rm peak}$ is a function of radio luminosity. Rigby et al. (2015) extended their earlier study to even lower radio luminosities and found consistent results.

It is largely agreed, however, that the RLF at any epoch is dominated by two distinct classes of objects – star-forming systems at the lowest luminosities, which are generally hosted by late-type galaxies, and radio-loud AGN at higher luminosities, generally found to reside in massive early-type galaxies and powered by accretion on to the central SMBH (Jackson & Wall 1999). Radio-loud AGN can further be divided into two categories based on their radio morphologies (Fanaroff & Riley 1974). The Fanaroff-Riley class I (FRI) objects are brightest at their centres and have intermediate radio luminosities, whereas the FR class II (FRII) objects are brightest at the edges, away from the central regions and are some of the most luminous radio sources observed. Dunlop & Peacock (1990) showed that the dividing line between the FR classes, generally thought to be around 10^{25} W Hz^{-1} at $150 - 200$ MHz, is remarkably close to the break in the local RLF.

Observations have been complemented by theoretical studies aiming to understand the evolution of the radio luminosities and sizes of both FRI and FRII objects.

These include modelling the dynamics of a radio source powered by relativistic jets resulting from the accretion on to the SMBH (Kaiser & Alexander 1997) and modelling the different physical processes through which a radio source may lose energy (Kaiser et al. 1997; Blundell et al. 1999; Alexander 2002). Some studies have also explored the link between the growth of the two FR classes (Alexander 2000; Kaiser & Best 2007). However, not a lot of work has gone into painting a complete picture that incorporates the growth of black holes with the evolution of individual radio sources.

In this work, we attempt to model the radio luminosity function based on black hole mass functions. Such an approach naturally establishes a link between the the growth of black holes and the resulting radio luminosity function, which can be tested using existing and upcoming radio surveys. We begin by testing our model at redshift 2, for which there are sufficient observations available. We then extend our model to $z = 6$ with the ultimate goal of predicting a radio luminosity function close to or even into the EoR. Finally we use the modelled RLF to make predictions about the number of radio sources that could be observed in the current and upcoming state-of-the-art low-frequency radio surveys.

The layout of this paper is as follows. In Section 2.2 we construct and describe our model for the growth and evolution of luminosities and linear sizes of radio sources. In Section 2.3 we present luminosity and size predictions from our model at $z = 2$ and test them using data available in the literature. We extend our model to $z = 6$ in Section 2.4 and present our predicted luminosity function and linear size distribution. We then test the predictions at $z = 6$ by comparing with a RLF obtained using a pure density evolution model extrapolated from lower redshifts. We present the number of expected sources in current and future low frequency radio surveys and assess the trade-off between coverage area and depth, determining the optimum survey parameters to maximise detection of radio sources at high redshifts. Finally, we present a summary of our findings in Section 3.6.

Throughout this paper we assume a flat ΛCDM cosmology with $H_0 = 67.8$ km/s/Mpc and $\Omega_m = 0.307$. These parameters are taken from the first Planck cosmological data release (Planck Collaboration et al. 2014).

2.2 Modelling radio luminosities and linear sizes

2.2.1 Input black hole mass function and Eddington ratio distribution

It is generally believed that radio galaxies are powered by accretion of material on to the supermassive black hole (SMBH). Therefore, we take black hole mass obeying the black hole mass functions (BHMF) determined at different epochs by Shankar et al. (2009) as one of the inputs. These BHMFs have been derived using AGN bolometric luminosity functions estimated using optical and X-ray observations, making certain assumptions about radiative efficiency. The BHMF is generally well fit by a Schechter function of the form

$$\phi(M_{BH}) = \phi_\star \left(\frac{M_{BH}}{M_\star}\right)^\alpha \exp\left[-\frac{M_{BH}}{M_\star}\right] \tag{2.1}$$

where $\phi_\star$ and $M_\star$ are the characteristic space density and black hole mass, respectively and α is the low-mass end slope.

For an actively accreting SMBH with an accretion rate dM/dt, the bolometric luminosity can be written as $L_{bol} = \epsilon(dM/dt)c^2$, where ϵ is the efficiency parameter and c is the speed of light. The maximum possible luminosity achievable through this mechanism is the Eddington luminosity, L_{Edd} and the ratio of the bolometric luminosity to the Eddington luminosity, the Eddington ratio, is written as $\lambda = L_{bol}/L_{Edd}$. This can take values between 0 and 1, and is an indicator of how 'actively' a SMBH is accreting. The Eddington ratio is another input in our model, which is drawn from a log-normal distribution that Shankar et al. (2013) found to fit the observed AGN luminosity functions well and is also supported by Willott et al. (2010b) at $z \sim 6$.

2.2.2 Radio jet power calculation

The jet power is thought to be closely coupled to the black hole mass, spin and accretion rate via the Blandford-Znajek mechanism (Blandford & Znajek 1977). Jet power can be calculated either by using the thin disk solution (Shakura & Sunyaev 1973), which typically works for black holes accreting at higher Eddington ratios ($\lambda > 0.01$) or by assuming a thick accretion disk with an advection dominated accretion flow (ADAF) for black holes accreting at lower rates (Narayan & Yi 1994). The expression for jet power in the thin disk regime can be written as (Meier 2002; Orsi et al. 2016)

$$Q_{\rm jet} = 2 \times 10^{36} \left(\frac{M_{BH}}{10^9 M_\odot}\right)^{1.1} \left(\frac{\lambda}{0.01}\right)^{1.2} a^2 \ \ \mathrm{W} \tag{2.2}$$

and in the ADAF regime can be written as

$$Q_{\rm jet} = 2.5 \times 10^{38} \left(\frac{M_{BH}}{10^9 M_\odot}\right) \left(\frac{\lambda}{0.01}\right) a^2 \ \ \mathrm{W} \tag{2.3}$$

where M_{BH} is the black hole mass, λ is the Eddington ratio and a is the black hole spin. We use a Monte Carlo based approach where a value of λ is randomly sampled from the given input distribution (which we elaborate upon in the next section) and assigned to a black hole mass to calculate jet powers for each source using Equations 2.2 or 2.3, depending on the Eddington ratio.

Although studies have indicated that AGN might experience recurrent jet activity through refuelling of the central black hole due to a possible merger, the lifetime of a luminous radio source is typically of the order of 10^7 yr, with the AGN duty cycle found to be close to 10^9 yr (Bird et al. 2008). Note that duty cycle values have been shown to strongly depend on the stellar mass of host galaxies (Best et al. 2005). However, the typical duty cycle timescale is longer than the time for which we evolve our sources, which we talk about in the following sections. Therefore, any recurrent jet activity is not taken into account in our modelling.

2.2.3 Radio luminosity calculation

Several studies have aimed to establish an empirically derived relation between the intrinsic jet power and the observed radio luminosity (Bîrzan et al. 2004, 2008; Cavagnolo et al. 2010). There have also been several attempts to construct analytical models for the growth of jets in radio sources, especially in strong radio sources with an FRII-type morphology that are typically associated with HzRGs (Kaiser & Alexander 1997; Kaiser et al. 1997; Blundell et al. 1999; Alexander 2000, 2002).

Kaiser & Best (2007, hereafter KB07) studied analytically the growth of radio galaxies in the context of the radio luminosity function and determined that the luminosity function at any epoch consists of sources that are dominated by different energy loss mechanisms, depending on their ages and sizes. Each energy loss phase affects their growth and the evolution of their radio luminosity differently. We use the KB07 prescriptions to track the growth of radio sources in our model, which contribute to the luminosity functions. We briefly describe the implemented energy loss mechanisms below.

Synchrotron losses

Synchrotron radiation from ultra-relativistic charged particles is believed to be the major source of virtually all extragalactic radio sources. In star-forming galaxies, synchrotron radiation originates from electrons from HII regions, accelerated by Type II and Ib supernovae. In radio-loud AGN, charged particles are accelerated in the jets and lobes launched by the central SMBH due to accretion of matter, and such systems are the focus of this model.

The energy density of the magnetic field associated with a radio source decreases as a source grows. Therefore, synchrotron emission dominates early in the source's lifetime. KB07 noted that the luminosity of a source growing in this regime stays constant, with the luminosity at an observing frequency ν given by

$$L_\nu \approx \frac{m_e c^2 f_n}{6A^{1/2}\nu} Q_{jet} \tag{2.4}$$

where m_e is the mass of an electron, c is the speed of light, f_n and A are constants with fiducial values 1.2×10^{12} s^{2}kg^{-1}m^{-2} and 4, respectively.

Adiabatic losses

After the early stages of synchrotron losses, the magnetic field strength declines and adiabatic losses begin to dominate. The gas density around a radio-loud AGN into which the jets and lobes grow is generally represented by a single-β model of the form

$$\rho_r = \frac{\rho}{[1 + (r/d)^2]^{\beta/2}} \tag{2.5}$$

where ρ is the density in the inner-most regions, d is the distance until which the gas density remains constant (and follows a power-law decline afterwards) and r is the distance from the centre of the gas distribution. Such a profile has been found to fit X-ray emission from hot gas in elliptical galaxies (that usually host radio-loud AGN), galaxy groups and clusters (Fukazawa et al. 2004).

When the source is in the adiabatic loss phase, the luminosity evolves as (KB07)

$$L_\nu \propto D^{(8-7\beta)/12} \tag{2.6}$$

where D is the linear size of the radio lobe and β depends on the profile of the ambient gas surrounding the radio source.

Inverse Compton losses

Once the size of the lobe has exceeded the extent of the x-ray halo of the host galaxy, and the energy density of the magnetic field in the lobe is comparable to the energy density of the ambient cosmic microwave background (CMB) radiation, losses due to inverse Compton scattering against CMB photons begin to dominate. KB07 found that the luminosity in this phase evolves as

$$L_\nu \propto D^{(-4-\beta)/3} \tag{2.7}$$

The CMB energy density scales with redshift, z, as $\propto (1 + z)^4$. Therefore at higher redshifts, IC losses should begin to dominate much earlier in the source's lifetime. We calculate the distance from the centre of the galaxy after which IC losses begin to dominate, D_{IC}, by equating the luminosities produced by adiabatic losses and IC losses, given by equations (3) and (7) in KB07. This depends on the jet power of the source and can be written as (See Appendix 2.A)

$$D_{IC} \propto (\rho d^{\beta})^{-1/6} Q_{jet}^{1/3} (1+z)^{-8/3} \tag{2.8}$$

Overall evolution and RLF determination

Having set up the various phases of evolution, we can track the luminosity and size evolution of all our sources. Equation (A2) in KB07 describes the growth of the lobe size, D with time

$$D = C \left(\frac{Q_{jet}}{\rho d^{\beta}} \right)^{1/(5-\beta)} t^{3/(5-\beta)} \tag{2.9}$$

where C is a constant. For simplicity, we use the fiducial values from KB07 and set the extent till which the gas density remains constant to $d = 2$ kpc at $z = 2$. We then include redshift evolution of linear sizes of galaxies. van der Wel et al. (2014, and references therein) find that over the redshift range $0 < z < 3$, the size evolution of early-type galaxies is much faster than late-type galaxies. Further, Mosleh et al. (2012) find that the sizes of Lyman break selected galaxies (LBGs) with stellar masses of $10^{9.5} < M_{\star} < 10^{10.4}$ evolve as $(1+z)^{-1.2}$ from $z = 1$ to 7, which is consistent with the findings of van der Wel et al. (2014). At higher redshifts, $7 < z < 12$, Ono et al. (2013) find the size evolution of LBGs to follow $(1+z)^{-1.3}$. Radio galaxies are more likely to be hosted by early-type galaxies up to redshifts of $z = 3$, but at higher redshifts, HzRGs are seen to be forming stars intensively (Miley & De Breuck 2008).

Owing to the faster evolution of early-type galaxies seen at moderate redshifts and the redshift evolution of LBGs at higher redshift, and assuming that early in the universe radio galaxies are expected to be hosted by galaxies with properties similar to LBGs, we include the size evolution with redshift as $(1+z)^{-1.25}$, which is consistent with the majority of studies carried out at $z > 2$. Therefore, the parameter d takes values

$$d = \begin{cases} 2 \text{ kpc}, & \text{if } z \leqslant 2 \\ 2 \times [(1+z)/3]^{-1.25} \text{ kpc}, & \text{if } z > 2 \end{cases}$$

The gas density in the inner parts of the galaxy is set as $\rho = 10^{-22}$ kg m^{-3} at all redshifts.

The initial growth of the lobe would be in a region where the ambient gas density is roughly constant, i.e. $D < d$ and therefore, $\beta = 0$. This very early

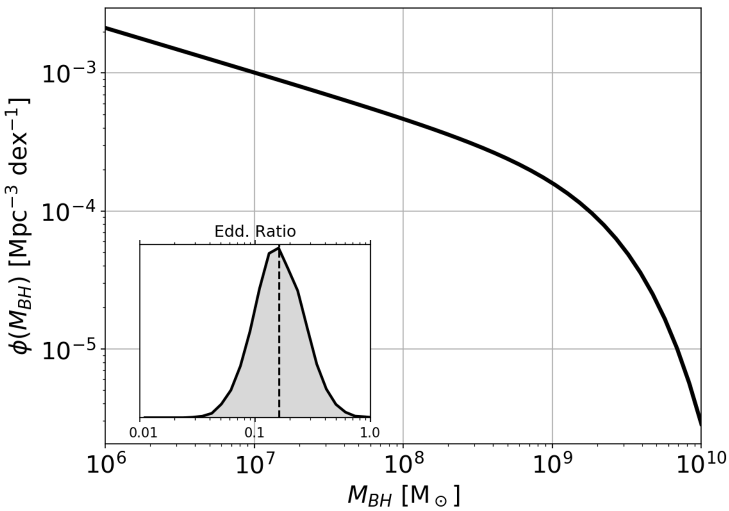

Figure 2.1: Input black hole mass function and the Eddington ratio at $z = 2$ taken from Shankar et al. (2009) and Shankar et al. (2013). Shown in the figure is the best fit Schechter function determined at $z = 2$. The Eddington ratio distribution is a log-normal peaking at $\lambda = 0.16$.

growth would be dominated by synchrotron losses as the magnetic field is influential. Considering Equation 2.4, the luminosity would level off at the stage when synchrotron radiation dominates. After the lobe has grown to a size of 2 kpc, the source enters the adiabatic loss phase. Here, we consider the gas density profile around the radio source to follow a power law decline (Equation 2.5), with $\beta = 2$ being used for further evolution. Finally, once the source has grown to a size when the CMB energy density begins to play an important role, inverse Compton (IC) losses begin to dominate. The values of all model parameters used in this study are shown in Table 2.2 in Appendix 2.A.

2.3 Radio luminosities and linear sizes at z = 2

2.3.1 Model Input

We first implement our model at $z = 2$ to compare the predictions of our model to data, as the radio luminosity function at this epoch is relatively well constrained (Dunlop & Peacock 1990; Blundell et al. 1999; Willott et al. 2001; Rigby et al. 2011, 2015). We use the Shankar et al. (2009) BHMF determined at $z = 2$, which is a Schechter function with parameters $\log \phi_\star = -3.665$, $\log M_\star = 9.076$, and

$\alpha = -0.3223$, and the lognormal Eddington ratio distribution peaking at $\lambda = 0.16$ with dispersion of 0.5 dex from Shankar et al. (2013) (both shown in Figure 2.1) as input. For simplicity, we assume the Eddington ratio to be independent of the black hole mass. We randomly sample a value of the Eddington ratio from the chosen distribution and assign it to each black hole.

We assume a mass dependence for the spin parameter of our black holes, following the conclusions of Volonteri et al. (2007). They note that disk galaxies harbour lower mass SMBHs and weaker AGN, and grow by accreting smaller packets of material. This would skew the black hole spin distribution to lower values. Brighter radio sources, however, are found in elliptical galaxies that host massive SMBHs. These black holes must have had a major accretion episode, likely powered by a merger that was responsible for forming the host elliptical galaxies too. During this episode the spin must have increased significantly. Volonteri et al. (2007) show that the peak in distribution of spin parameter for black holes with masses greater than $10^8\ M_\odot$ lies between $0.7 - 1.0$. Therefore, black holes with masses greater than $10^8\ M_\odot$ in our simulation are randomly assigned a spin from the range $[0.7, 1.0)$ and all other black holes are assigned a spin from the range $[0.0, 0.7)$. As a test, we implement two other spin distribution schemes, one where the mass dependence is reversed, i.e. the smaller mass black holes have higher spins, and the other where all black holes have a constant spin of 0.6. The black hole mass, Eddington ratio and spin parameter are the required inputs to calculate jet powers for all sources in our simulation.

2.3.2 Output jet power distribution

The resulting jet power distributions for the 3 different choices of spin parameter distributions are shown in Figure 2.2. Cases where smaller black holes have higher spin (Case 2) and a constant spin parameter (Case 3) are unable to produce the most powerful jets, which have been observed in the literature (see Godfrey & Shabala 2013). The widely supported idea that more massive black holes are highly spun up (Case 1) accurately reproduces the bimodal distribution of jet powers, which is thought to result in the fundamental difference between the FRI and FRII type radio galaxies. This bimodality is likely due to the two different accretion regimes implemented in our model (ADAF and thin disk regimes), that depend on the accretion rate. Therefore, going forward, we only consider results from Case 1 of spin parameter choice.

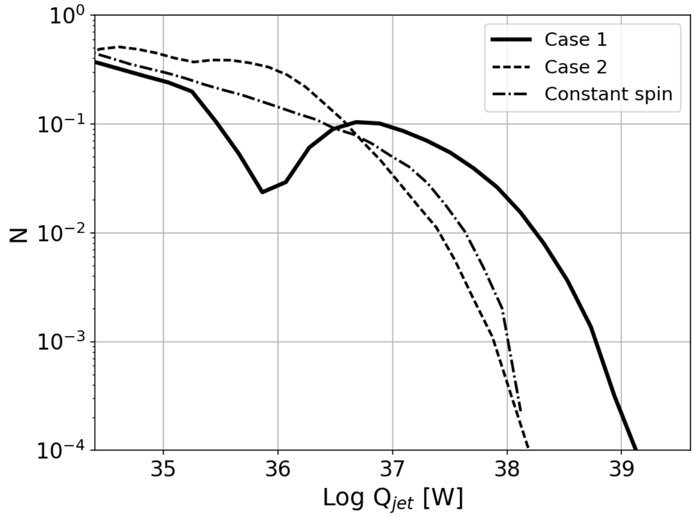

Figure 2.2: Distribution of jet powers predicted by our model at $z = 2$ for different choices of spin parameters. Case 1 is when more massive black holes have a higher spin, Case 2 is when more massive black holes have lower spin and Case 3 is when all black holes have a constant spin. Case 1 most accurately reproduces the bimodality in jet power, and is able to produce sources with very powerful jets that result in some of the largest and brightest radio galaxies in the universe.

2.3.3 Constructing and normalising the radio luminosity function

The first step at which we construct the luminosity function is when the linear size of all sources in the simulation is 2 kpc, i.e. when all sources are dominated by synchrotron losses. Since the growth rate depends on jet power, the radio sources take different times to attain a size of 2 kpc, thus leading to an age distribution. To now track the evolution of radio luminosities, we evolve our sources in time steps of 0.2 Myr, calculating linear sizes at each time step. The size determines which phase of energy loss each source is in and we use this to calculate the evolved luminosities at each time step according to the prescriptions described in the previous section. The simulation is run for a total time of 9 Myr, which is the typical lifetime of a radio galaxy.

Although it has been shown that the radio-loud fraction of AGN is a function of the stellar mass of the host galaxy and the black hole mass in the local universe, these values are relatively unconstrained at high redshifts (Best et al. 2005; Williams & Röttgering 2015). The physical conditions of the universe change dramatically going from $z = 0$ to $z = 2$, so a simple extrapolation from the local universe would not work. It has been observed however, that roughly 10% of all galaxies are AGN (Martini et al. 2013, and references therein) and of these, only 10% are generally found to be bright in the radio or radio-loud, even out to higher redshifts (Bañados et al. 2015). Further, the correlation between stellar mass and radio-loud fraction is weaker for high-excitation radio galaxies (Janssen et al. 2012), which most radio sources at high redshifts are expected to be. Therefore, we take a simplistic approach and randomly select 1% of all our sources to be included in the final radio luminosity function. It is important to note that we do not select objects to be AGN or radio-loud depending on the black hole mass, as black hole masses of (radio-loud) AGN seem to be distributed evenly over several orders of magnitude (Woo & Urry 2002).

We use the Shankar et al. (2009) black hole space densities to normalise the radio luminosity function in the following way. The space densities from the analytical BHMF are used to assign a maximum volume, $V_{\rm max}$, to each simulated black hole, which is the volume probed by a complete survey that would enable the black hole to be detected. These calculated volumes are then used to normalise the resulting radio luminosity function, by summing over $1/V_{\rm max}$ in each luminosity bin, which is the traditional way of calculating luminosity functions (Schmidt 1968).

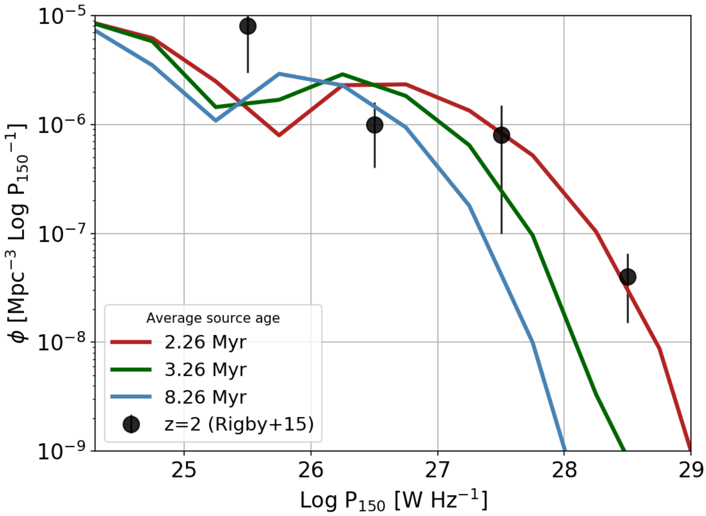

Figure 2.3: Time evolution of the radio luminosity function (RLF) at $z = 2$ at various time steps in our model. Each curve shows the predicted luminosity function at a given average source age. The brightest sources lose their energy very quickly and therefore, those observed must be young. Also shown are the space densities calculated by Rigby et al. (2015), which have been recalculated at 150 MHz. Additionally, two distinct radio populations are apparent, with the dividing luminosity lying between 10^{25} and 10^{26} W Hz^{-1}, which is consistent with the luminosity that is generally considered as the dividing line between the FRI and FRII sources (Dunlop & Peacock 1990; Willott et al. 2001).

2.3.4 Output luminosity functions

Luminosity distributions constructed for 3 time steps are shown in Figure 2.3. The bright end of the luminosity distribution is seen to change, whereas the faint end remains roughly constant over time. This is mainly because the most powerful sources in the simulation grow faster and this rapid growth leads to increased adiabatic losses. Additionally, sources with powerful jets enter the regime of Inverse Compton losses and end up losing energy much quicker. This suggests that the most powerful sources must be very young and as a result, compact.

We plot the space densities calculated by Rigby et al. (2015) for comparison. Since the space densities were calculated at an observing frequency of 1.4 GHz, we scale it to obtain powers at 150 MHz using the $z - \alpha$ relation $\alpha = 0.8 + 0.21\log(1+z)$, determined by Ker et al. (2012). Overall, the data seems to match the predictions well and is also consistent with the expectation that most powerful sources must be younger. There is a slight disagreement in the luminosity bin $25 < \log P < 26$, where the observed space densities are higher than our prediction. However, this may be explained by the apparent presence of two distinct populations, with the dividing luminosity between $10^{25} - 10^{26}$ W Hz^{-1}. This coincides with the dividing luminosity between FRI and FRII radio sources, which is seen in observations (Dunlop & Peacock 1990; Willott et al. 2001) and was also predicted by KB07.

Another interesting feature especially prominent around this dividing luminosity, is the transition of sources from the FRII to the FRI regime over time (purely on the basis of radio power; within the framework of this simulation, we are unable to separate the sources morphologically). Such a scenario was suggested by KB07, where the development of an FRII structure in a source with a weak jet can be disrupted by dense external gas, which starts to fill the lobe volume, eventually reaching the jet flow. At this point the morphology is expected to change from FRII to FRI accompanied by a decrease in radio luminosity, which is what we may be seeing in our simulation. Such a behaviour, combined with the apparent bimodality in the distribution of jet powers as seen in Figure 2.2 suggests that the origin of the FRI and FRII populations could be purely due to the mechanism by which the central SMBH is accreting gas. Such a scenario was suggested by Best & Heckman (2012), where they constructed a large sample of radio sources from the SDSS and classified them broadly into two categories based on their emission line properties, low-excitation radio galaxies (LERGs) and high-excitation radio galaxies (HERGs). They found LERGs to dominate at low radio luminosities and HERGs to dominate at high luminosities, with the switch in population dominance found to be at $L_{1.4\,\mathrm{GHz}} = 10^{26}$ W Hz^{-1}. LERGs are powered by radiatively inefficient accretion, with much lower accretion rate compared to the radiatively efficient

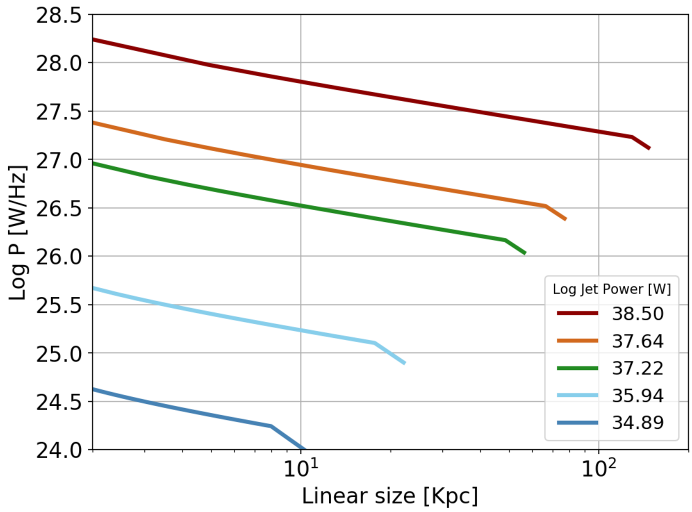

Figure 2.4: The so-called P-D tracks, showing the evolution of radio power (P) with linear size (D) for sources with different radio jet powers at $z = 2$. Sources with stronger jets have a well behaved evolution, whereas sources with weaker jets have a break in their track very early in their lifetime. This is because weaker sources enter the regime of inverse Compton losses much quicker.

accretion that powers HERGs. This divide in luminosity is roughly where we observe two separate populations too, which we attribute to the difference in accretion mechanism. Therefore, the scenarios suggested by Best & Heckman (2012) and what we see in our simulation seem to be consistent.

2.3.5 Output size distribution

The included energy-loss prescriptions in our model give rise to 'P-D tracks' for every source in our simulation, which have been historically used to study the evolution of radio lobes in FRII galaxies (Blundell et al. 1999; Alexander 2000, 2002; Kaiser & Best 2007). Figure 2.4 shows P-D tracks for sources with different jet powers for the entirety of the simulation run (9 Myrs). Sources with low jet powers show a break in their P-D track, which arises when there is a decline in their radio luminosities after attaining a certain linear size, when the dominant energy loss mechanism changes from adiabatic losses to inverse Compton (IC) losses from the CMB. Growth of the source in the IC regime is slower. Sources with high jet powers follow, however, are more likely never to be dominated by IC losses and follow a well-behaved path along the P-D diagram.

Since the average linear sizes of observable sources in our model depend strongly

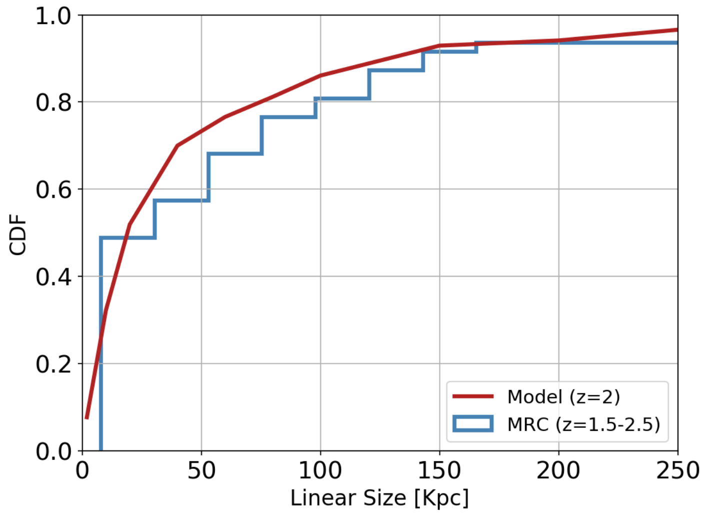

Figure 2.5: Comparison of the cumulative distribution of linear sizes of FRII radio sources predicted by our model (red line) with radio galaxies with confirmed redshifts in the range $z = 1.5 - 2.5$ from the Molonglo Reference Catalogue (MRC; blue line). The distributions seem to agree well, with our model not under- or over-predicting very small or very large linear sizes. The MRC contains 3 sources with sizes greater than 250 kpc in the selected redshift range and since our model at $z = 2$ is unable to produce sources with sizes greater than 250 kpc, we have excluded these particular MRC sources in this comparison for clarity.

on the average age of sources at a given time step, we weigh the observed sizes by age. This is done by assigning a probability of detection, which is defined as the age of a source divided by its total lifetime in the simulation. This means that younger sources have a lower probability of detection than sources that have existed in the universe for a longer time. We construct a linear size distribution in time steps of 1 Myr and normalise this distribution by assigning a detection probability to each source.

To test the size predictions from our model, we use the catalogue compiled by Singal & Laxmi Singh (2013), which contains linear sizes and redshifts for radio sources in the Molonglo Reference Catalogue (MRC; Large et al. 1981). The original MRC contains 12,141 discrete sources with flux density $\geqslant 0.7$ Jy and the survey covers 7.85 sr. of the sky. For this comparison we only consider sources in the redshift range $1.5-2.5$ in the Singal & Laxmi Singh (2013) catalogue. We also implement a flux cut in our predicted observations that matches the completeness level of the sample. The cumulative distribution functions of linear sizes predicted by our model and the MRC are shown in Figure 2.5. The size distributions seem to agree and our model does not over- or under-predict very large or small sources.

Within the selected redshift range however, the Singal & Laxmi Singh (2013) sample contains 3 sources with linear sizes > 250 kpc (263, 284 and 458 kpc at redshifts 1.54, 1.78 and 1.54 respectively). Our model at $z = 2$ is unable to produce sources with sizes greater than 250 kpc. This could be because we do not model recurrent jet activity, which may be responsible for the continued growth of a radio source by periodically refuelling the jet from the SMBH. Therefore, in the comparison shown in Figure 2.5, we have excluded the three largest sources from the MRC. It is safe to assume, however, that the inclusion of the largest sources should not affect the cumulative distribution of linear sizes too much as these sources lie well above the mean linear size.

2.4 Implementing the model at z = 6

Having tested the predictions of our model at $z = 2$ where there are sufficient observations available, we now extend the model to $z = 6$ to predict a radio luminosity function at this redshift, and describe the implementation in the following section.

2.4.1 Model input

We use the black hole mass function (BHMF) and Eddington ratio distribution at $z = 6$ determined by Willott et al. (2010b) using the quasar luminosity function and estimation of black hole masses through measurements of MgII line widths. The luminosity function they use to derive the BHMF has been found to be consistent with more recent studies of $z \sim 6$ quasars exploring both fainter and brighter populations (Kashikawa et al. 2015; Jiang et al. 2016) The best-fit Schechter function parameters for their BHMF assuming a duty cycle of 0.75 are $M_\star = 2.24\times10^9$ $M_\odot$, $\phi_\star(M_{BH}) = 1.23\times10^{-8}$ Mpc^{-3} dex^{-1} and faint-end slope $\alpha = -1.03$. Further, Willott et al. (2010b) found the Eddington ratio distribution at $z = 6$ to be a log-normal distribution, peaking at 0.6 and with a dispersion of 0.30 dex, which is consistent with the distribution used by Shankar et al. (2013) and this is what we use in our model.

We also account for the redshift-evolution of linear sizes of galaxies and how that affects the parameter d, which represents the extent of constant gas density around a source. This redshift evolution goes as $\propto (1 + z)^{-1.25}$ as discussed in Section 2.3.4. Finally, in order for the black hole masses to be high enough at $z = 6$, they must have been accreting very close to the Eddington limit from very early times after their formation and must be nearly maximally spun up (Shapiro 2005; Daly 2009; Dubois et al. 2014). Therefore, we set the spin parameter at this redshift to $a = 1$. The simulation is run for a total of 5 Myrs.

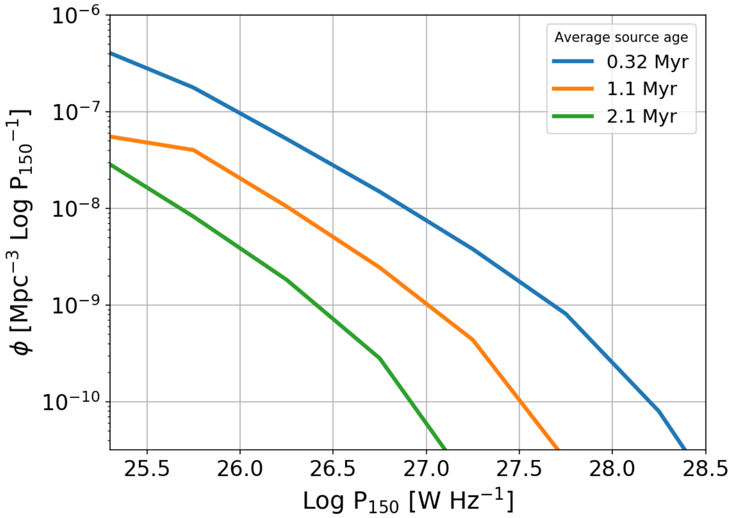

Figure 2.6: Luminosity functions at $z = 6$ at various stages of source evolution. The mean ages of the sources contributing to the luminosity function are shown. At this redshift, it is clear that sources are much younger and lose their energy much more rapidly. This increased loss of energy can be attributed to the much stronger CMB energy density, which increases the inverse Compton losses. After ~ 2 Myrs, there are hardly any luminous sources left in the simulation. This suggests that luminous radio sources observed at $z = 6$ must be very young. The faint end is seen to evolve less than the bright end.

2.4.2 Model predictions at z = 6

Radio luminosity function

The time evolution of the distribution of radio luminosities at $z = 6$ is shown in Figure 2.6. Note that only sources with FRII-like radio powers are shown, as less luminous sources at $z = 6$ are beyond the detection capabilities of current radio surveys. There are only a handful of sources with very powerful radio luminosities ($> 10^{28}$ W Hz^{-1}). This is mainly due to the generally lower SMBH masses at higher redshifts and the increased inverse Compton losses due to the denser CMB. The time evolution of the luminosity function is much stronger too, which can be attributed to rapid energy losses. This is especially prevalent at the most luminous end of the luminosity function, which can be seen from the 'P-D' tracks for sources in our simulation, shown in Figure 2.7. More luminous sources are fuelled by powerful jets and grow faster. As a result, they enter the regime of strong Inverse Compton (IC) losses much earlier in their lifetime. At lower luminosities, evolution is slower as it consists of sources with relatively weaker jets that grow at a lower

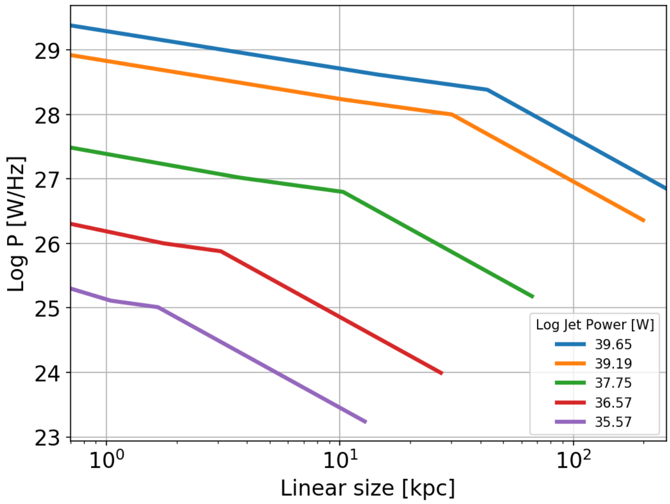

Figure 2.7: Comparison of the evolution of radio power with linear size (P-D tracks) for sources with given jet powers in our simulation at $z = 6$. Clearly, the Inverse Compton losses come in to effect much quicker at higher redshifts, as evident from the break in the P-D tracks at much smaller linear sizes. Overall, sources at $z = 6$ find it much harder to grow to large sizes due to the increased CMB energy density.

rate and lose their energy less rapidly.

Overall at $z = 6$, sources are younger and lose energy at a rate that is much higher than seen at lower redshifts. This has implications on the nature of sources that we can expect to observe at $z \geqslant 6$. Any luminous source observed at this epoch must be very young and compact, consistent with the 'inevitable youthfulness' of radio sources in the early universe, as suggested by Blundell & Rawlings (1999).

Linear sizes

The higher CMB energy density prevents lobes from growing to large sizes (a few hundred kpc) and as a result, linear sizes at higher redshifts are generally smaller compared to lower redshifts. We apply the age-weighted normalisation introduced in Section 3.5, keeping in mind that the detection probability of younger sources is less than older ones. The resulting linear size distribution for sources brighter than 0.5 mJy at 150 MHz, which represents the lowest flux densities for the LOFAR Tier 1 survey (Shimwell et al. 2017), is shown in Figure 2.8. Also shown in the inset is the cumulative distribution function of the linear size distribution. We find that the median size of radio galaxies at $z = 6$ is 20 kpc, which translates to an angular scale of roughly 3.5 arcseconds on the sky.

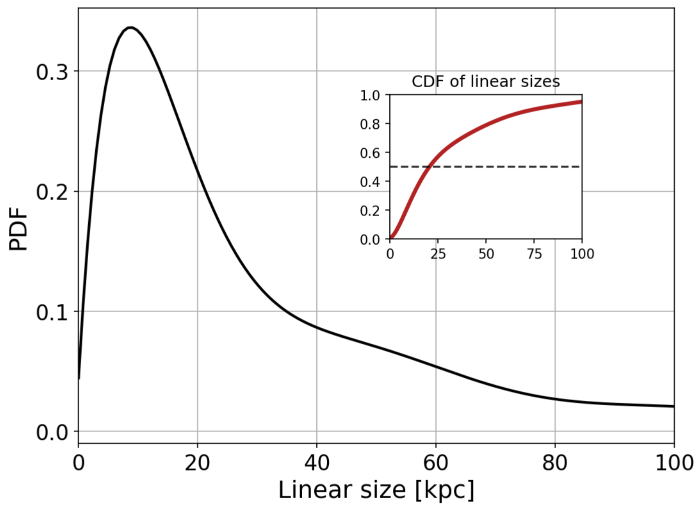

Figure 2.8: The age-weighted probability distribution function and the cumulative distribution (inset) of predicted linear sizes of radio galaxies at $z = 6$. The mean linear size is expected to be roughly 25-30 kpc. Large sources at this epoch die out quicker due to the increased energy density of the CMB. Therefore, radio sources at $z = 6$ are generally expected to be young and very compact.

Our size prediction at $z = 6$ seems to be in line with the observed sizes of currently known high-redshift radio galaxies, as reported by Blundell et al. (1999), Singal & Laxmi Singh (2013), and van Breugel et al. (1999), shown in Figure 2.9. Also shown as reference is the redshift dependence of the parameter D_{IC} (see Section 2.3.3) for a constant jet power (dashed line). It is worth noting that the samples used to compare our results are flux limited, with the Blundell et al. (1999) sample containing sources with $S_{151} \geqslant 0.50$ Jy, Singal & Laxmi Singh (2013) sample containing sources with $S_{150} > 0.7$ Jy and sources in van Breugel et al. (1999), based on the sample of ultra-steep spectrum radio sources compiled by De Breuck et al. (2000a), having flux densities $S_{150} \geqslant 180$ mJy. These are likely to introduce various selection effects that may affect linear size determination that our model does not take into account. Additionally, the flux limits of the above mentioned samples may have implications on linear sizes being probed, as radio power and size seem to be correlated, as seen through the P-D tracks and as reported by Ker et al. (2012). Regardless, the sizes predicted by our model seem to be in line with the observed trend.

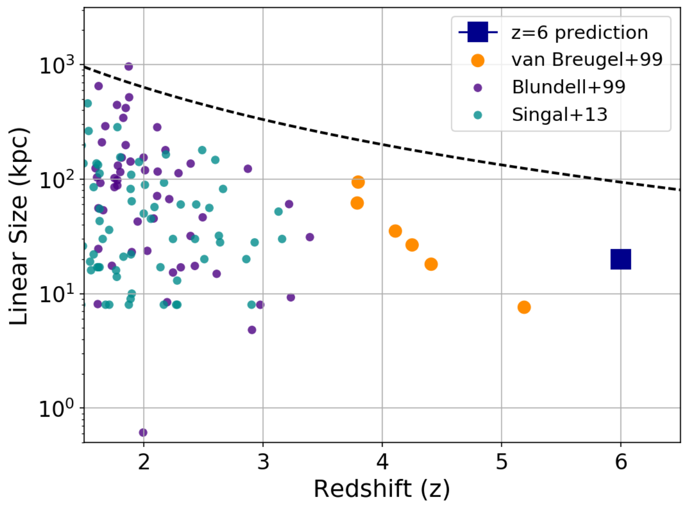

Figure 2.9: The median linear size of radio sources at $z = 6$ with $S_{150} > 0.5$ mJy at 150 MHz in our simulation was found to be around 20 Kpc, shown as a blue square. Also shown are sizes of HzRGs taken from Blundell et al. (1999) (purple points), Singal & Laxmi Singh (2013) (cyan points) and van Breugel et al. (1999) (orange points), which have been updated using the cosmology used in this study. The dashed line shown for representative purposes is the evolution of the parameter D_{IC}, which we show to be a function of redshift (Equation 8). Our predictions seem to be in line with the generally decreasing trend of linear sizes with redshift.

2.4.3 Comparison with exponential evolution of space densities

For further analysis, we take into consideration the predicted $z = 6$ radio luminosity function (RLF) at an average source age of ~ 0.32 Myr. At this time step, the functional form of the RLF is well behaved and samples a broad range of luminosities. The resulting luminosity function is well fit with a double power law of the form

$$\phi(P) = \phi_\star \times \left[\left(\frac{P}{P_\star} \right)^\alpha + \left(\frac{P}{P_\star} \right)^\beta \right]^{-1} \tag{2.10}$$

with parameters $\log \phi_\star = -9.05$ Mpc^{-3} dex^{-1}, $\log P_\star = 27.91$ W Hz^{-1}, faint end slope $\alpha = 1.04$ and bright end slope $\beta = 2.92$.

We now compare the predicted RLF with a simple density evolution model for steep-spectrum radio sources obtained by evolving the relatively well constrained radio luminosity function at $z \sim 2$ determined by Rigby et al. (2015). Again, the space densities have been scaled to 150 MHz from 1.4 GHz at which they were originally calculated. The resulting space densities at 150 MHz are best fit with a double power-law, with parameters $\phi_\star = 1.80 \times 10^{-8}$ Mpc^{-3} $(\log P_{150})^{-1}$, $\log P_\star = 28.95$ W Hz^{-1}, $\alpha = 0.72$ and $\beta = 2.74$. We then assume an exponential decline in space density with redshift, which can be written as $\phi(P_{150}, z) = \phi(P_{150}, 2)10^{q(z-2.0)}$, where q is the evolutionary parameter. Several studies of quasars at various wavelengths have inferred the value of q to range from -0.59 to -0.43 (Fan et al. 2001; Fontanot et al. 2007; Brusa et al. 2009; Willott et al. 2010a; Civano et al. 2011; Roche et al. 2012). Assuming the evolution of radio galaxies to match the evolution of optically-selected quasars at high redshifts, it seems reasonable to scale the radio luminosity function using an exponentially declining model that seems to work for quasars.

We find that $q = -0.49$ fits our predicted RLF best, which is shown in Figure 2.10. The dashed region represents $-0.59 < q < -0.43$. The evolution we find is slightly stronger than what is observed in quasars. This is not surprising, as the dependence of radio luminosity on size and lifetime should introduce deviations from the evolution observed for quasars. Our model over-predicts space densities at the faintest end. This could be due to the fact that the faint-end slope of the black hole mass function we use as input is poorly constrained, which is most likely affecting the faint-end of our predicted RLF too. At the highest luminosities, space densities predicted by our model are lower than those expected from pure density evolution by a factor of 0.67 dex in the luminosity bin $\log P_{150} = 28.5 - 28.5$ and 2 dex in the bin $\log P_{150} = 28.5 - 29.0$, where our model barely predicts any sources. This is most likely due to the increasing dominance of inverse Compton losses at high redshifts, which lowers the space density of the brightest sources that grow

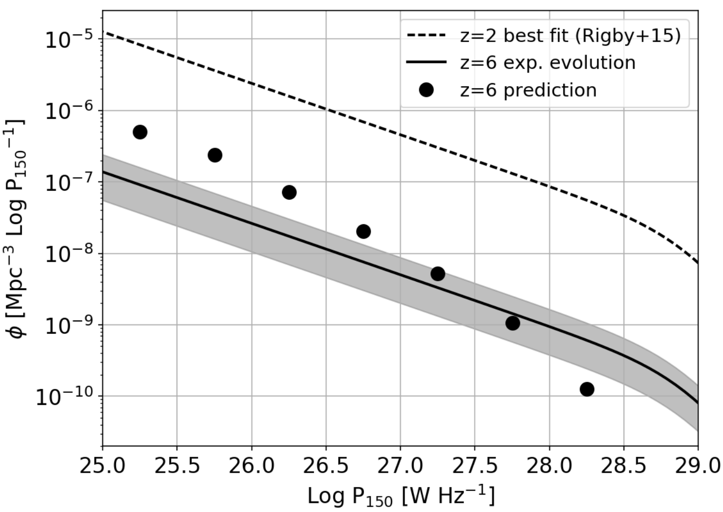

Figure 2.10: Comparison of the radio luminosity function at $z = 6$ predicted by our model (black points) and the RLF obtained by using a pure density evolution model from $z = 2$ (solid curve). The dashed curve shows the luminosity function at $z = 2$ determined by Rigby et al. (2015). The evolutionary parameter found to best match our prediction at $z = 6$ is $q = -0.49$, which indicates stronger evolution for radio galaxies but is within the observed evolution of optical and Xray quasar space densities at high redshifts. The shaded region shows RLFs expected with $-0.59 < q < -0.43$.

and lose energy quicker. This effect is not accounted for by pure density evolution, suggesting that a luminosity-dependent density evolution (LDDE) model (Dunlop & Peacock 1990; Willott et al. 2001; Rigby et al. 2011, 2015) may be better suited to describing the evolution of space densities of radio sources out to high redshifts.

2.4.4 Implications of radio luminosity function at z = 6

We now use the modelled RLF at $z = 6$ to make predictions about number counts in current and future low-frequency radio surveys. Expected number counts are essential for designing surveys and observing strategies that target the identification of the highest-redshift radio galaxies.

Number count predictions

To calculate expected number counts, we integrate the RLF at $z = 6$ down to flux limits chosen to represent various surveys at 150 MHz with instruments such as LOFAR[1], GMRT[2], and MWA[3], which are shown in Table 2.1. It is clear that the current and upcoming surveys with LOFAR will be the way forward to detecting a large number of $z \geqslant 6$ sources. The preliminary LoTSS direction-independent (DI) survey covers roughly 350 sq. degrees (Shimwell et al. 2017) and may lead to detection of around 32 radio galaxies at $z \geqslant 6$. Direction-dependent (DD) calibration, which takes care of effects such as varying ionospheric conditions and errors in beam models, is currently ongoing on the LoTSS fields and will result in high-fidelity images at full resolution and sensitivity (Shimwell et al. 2017). On completion, the LoTSS direction-dependent survey shall provide a large sky coverage (Dec > 0), leading to potential detection of more than 12000 $z \geqslant 6$ sources. The current highest-resolution survey at 150 MHz covering a very large area on the sky is the TGSS ADR, which covers around 37,000 sq. degrees above a declination of -53 (Intema et al. 2017). In this survey, one could expect to detect around 92 sources at $z = 6$.

The probability of 21-cm absorption arising from the neutral intergalactic medium at $z > 6$ depends on the optical depth of neutral hydrogen, τ, that pervades the universe. This in turn depends on a number of key parameters such as the temperature of the CMB, spin temperature of neutral hydrogen and the neutral hydrogen fraction (Carilli et al. 2002b). The detection of such features in the radio continuum of $z > 6$ sources, however, depends on a number of instrumental properties too. Ciardi et al. (2013) investigated whether 21cm absorption can be detected by

[1] http://www.lofar.org/

[2] http://www.gmrt.ncra.tifr.res.in/

[3] http://www.mwatelescope.org/

LOFAR and found that by using 48 stations and assuming the system temperature to be 200 K at an observing frequency of around 150 MHz, 21cm absorption features can be observed for a source at $z = 7$ with a flux density of 50 mJy, along a line-of-sight with $\tau = 0.12$. Such a detection would require an integration time of 1000 hours using a bandwidth of 5 kHz. Using a larger bandwidth may bring down the required integration time. Detection of a source with a flux density of 50 mJy at $z > 6$, however, is very unlikely but there may be more than 30 sources with flux densities > 15 mJy that could indeed be used for 21cm absorption studies (Carilli et al. 2002b). The on-going direction-dependent all-sky survey with LOFAR will be extremely efficient in laying the groundwork for future 21cm absorption studies with the SKA, when much fainter sources can be used for detection of 21cm absorption.

Observing strategies: Coverage area vs. depth

To compare what the ideal trade-off between depth and sky coverage would be that maximises the detection of $z \geqslant 6$ sources in current and upcoming surveys, we calculate the total number of sources that could be detected in a set observing time. A few assumptions go into this calculation: a) we assume that it takes 8 hours to reach depths of 0.1 mJy and b) each 'pointing' of the radio telescope covers 20 sq. degrees on the sky. These assumptions are based on the quoted values for LOFAR (Shimwell et al. 2017).

For a fixed observing time of 100 hours, the expected number of sources for different noise levels achievable is shown in Figure 2.11. Quite clearly, the LoTSS DI and DD surveys would be ideal to detect sources at $z > 5$. The luminosity functions at $z = 5$ and $z = 7$ are obtained by assuming pure density evolution with $q = -0.49$, which was found to best-fit our $z = 6$ RLF prediction in the previous section. There clearly lies a 'sweet-spot' in the coverage area vs. depth trade-off, which covers a large enough area and goes deep enough in a way that maximises detection of high-z radio sources. Note that the 4π sr. limit is achieved just after a flux density limit of 1 mJy in the given observing time.

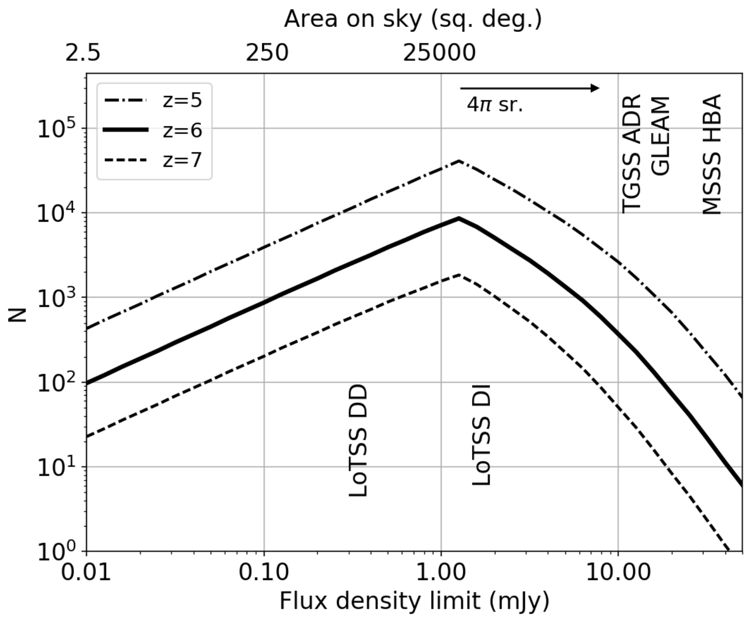

Figure 2.11: Number of high-z radio sources expected to be detected as a function of flux density limits reached in a fixed observing time of 100 hours, using standard LOFAR configuration. The upper x-axis shows sky coverage in the given observing time at a particular flux density limit. Also shown are the 5σ limits of current and future low-frequency surveys. The LoTSS DI and DD surveys seem to be ideal to detect a large number of $z > 5$ sources. This comparison further demonstrates that going too deep is not the best strategy as a large area of the sky needs to be surveyed to increase the number of detections.

Table 2.1: Predicted number of radio galaxies at $z = 6$ detected with 5σ in current and future surveys at 150 MHz.

Survey	Ref.	Flux lim (mJy/beam)	N (deg^{-2})	Area (deg^2)	Total N
LOFAR Tier 3 (planned)		0.01	7.18		
LOFAR Tier 2 (planned)		0.03	2.28		
LoTSS[a] direction-dependent (ongoing)	Shimwell et al. (2017)	0.1	0.63	20500	12915
LoTSS direction-independent	Shimwell et al. (2017)	0.5	0.092	350	32
TGSS ADR	Intema et al. (2017)	3.5	0.0025	37000	92
GLEAM	Wayth et al. (2015)	5	0.001	31000	31
LOFAR MSSS HBA	Heald et al. (2015)	10	0.0001	20500	2

[a] LOFAR Two-metre Sky Survey

2.5 Summary

In this study, we have used a semi-analytical model based on prescriptions laid out by KB07 to predict the luminosity and linear size distribution of radio sources. The model takes as input the black hole mass function and Eddington ratio distribution at any epoch and implements simple energy loss mechanisms that dominate at different phases of a radio source's lifetime. Radio jet powers are assigned to each active black hole depending on the black hole mass and the Eddington ratio, which is randomly sampled from the input distribution. As the radio source grows, it initially loses energy predominantly by synchrotron emission when its magnetic field is strong. Adiabatic losses take over in the intermediate phase, with inverse Compton losses due to the CMB radiation dominating in the later stages of a source's lifetime.

We first implement our model at $z = 2$ where sufficient data for radio luminosities and linear sizes is available. Making certain assumptions about the prevalent physical conditions and the black hole spin distribution, we predict a radio luminosity function that is consistent with observations. We are also able to reproduce the break in luminosity that marks the distinction between FRI and FRII radio source populations, supported by both theory and observations in the literature. We argue that this bi-modality in source population may be due to the accretion mechanism (thin disk vs. ADAF) that is responsible for powering the radio jets. Further, we are able to reproduce the distribution of linear sizes observed in flux limited surveys from the literature.

We then extend our modelling to $z = 6$ where radio sources can be unique probes of the epoch of reionisation as 21cm absorption features in the radio continuum of a source at $z > 6$ can be used to constrain the properties of the neutral inter-galactic medium in the very early universe. Using simplified assumptions about the black hole spin in the early universe, we predict a radio luminosity function at $z = 6$. We show that radio sources at $z = 6$ do not live for very long compared to typical ages of sources in the low-redshift universe. This is mainly due to radio jets being intrinsically weaker because of lower black hole masses and due to inverse Compton (IC) scattering being highly dominant in the early universe (due to a higher CMB energy density) that frustrates the jets and suppresses the growth of linear sizes of sources at high redshifts. Further, the predicted distribution of linear sizes is consistent with observations of the currently known highest redshift radio galaxies and the generally decreasing trend observed between linear sizes and redshift.

We compare the predicted $z = 6$ RLF with a pure density evolution model from lower-z for radio galaxies, based on the evolution of QSO luminosity functions.

The evolution is of the form

$$\phi(P_{150}, z) = \phi(P_{150}, 2)10^{q(z-2.0)} \tag{2.11}$$

We find that $q = -0.49$ fits reasonably well with luminosities between $10^{26.5} - 10^{28}$ W Hz^{-1}. There is some disagreement at the highest luminosity end and we attribute this to the significantly enhanced inverse Compton losses at higher redshifts, that have the most impact on luminous sources. Such an effect is not captured by a pure density evolution model and we argue that luminosity-dependent density evolution would better explain the redshift evolution of the radio luminosity function.

We finally predict the number of high redshift radio galaxies that may be observed in current and future low-frequency surveys with LOFAR, GMRT and MWA. To better understand the trade-off between coverage area and depth in a way that maximises detection of high-z radio sources, we calculate the total number of sources that would be expected as a function of flux density limits for a fixed observing time. We show that the LOFAR Two-metre Sky Survey (LoTSS) direction-independent and direction-dependent calibration surveys sit at the sweet-spot of coverage area and depth, and should be most effective at detecting large numbers of $z > 5$ radio sources. Detection of a 21cm absorption signal in the continuum of a radio source at $z > 6$ will enable studies of the epoch of reionisation in unparalleled detail.

Acknowledgments

We thank the referee for useful comments and suggestions. AS is grateful to Philip Best, George Miley and Kinwah Wu for fruitful discussions and comments over the course of this work. AS and HJR gratefully acknowledge support from the European Research Council under the European Union's Seventh Framework Programme (FP/2007-2013)/ERC Advanced Grant NEWCLUSTERS-321271. EER acknowledges financial support from NWO (grant number: NWO-TOP LOFAR 614.001.006).

This work has made extensive use of IPython (Pérez & Granger 2007). This research made use of Astropy, a community-developed core Python package for Astronomy (Astropy Collaboration et al. 2013). The data analysis and visualisation were done using TOPCAT (Taylor 2005). All figures used in this paper were produced using matplotlib (Hunter 2007a). This work would not have been possible without the countless hours put in by members of the open-source community all around the world.

2.A Calculation of Inverse Compton loss distance

Here we show the calculation of the distance from the galaxy at which Inverse Compton (IC) losses begin to dominate. This is done by equating the predicted luminosities from the adiabatic loss phase and the IC loss phase. The expressions for luminosities are adapted from Kaiser & Best (2007).

For a source in the adiabatic loss phase at an observing frequency of 150 MHz

$$L_{150} = \frac{3 f_L Q_{\rm jet} p^{3/4}}{3 + a_1} t \tag{2.12}$$

where $Q_{\rm jet}$ is the jet power, p is the pressure in the lobe and the constants $f_L = 3.4 \times 10^{-17} \left(\frac{0.15}{\rm GHz}\right)^{-1/2}$ J$^{1/4}$ m$^{1/4}$ s^2 kg^{-1}, and $a_1 = 3/2$ (Kaiser & Best 2007). The pressure inside the lobe is given by

$$p = f_p (\rho d^{\beta})^{1/3} Q_{\rm jet}^{2/3} D^{(-4-\beta)/3} \tag{2.13}$$

The luminosity of a source in the IC loss phase can be written as

$$L_{150} = \frac{3 m_e c^2 f_n Q_{\rm jet} p}{14 \sqrt{A} u_0^{\rm CMB} (1+z)^4 150 \text{ MHz}} \tag{2.14}$$

where m_e is the mass of an electron, c is the speed of light, $u_{\rm CMB}$ is the CMB energy density and the constants $f_n = 1.2 \times 10^{12}$ s^2 kg^{-1} m^{-2} and $A = 4$ (Kaiser & Best 2007). The present day CMB energy density, $u_0^{\rm CMB}$ is $\sim 4 \times 10^{-14}$ J m^{-3} and scales with redshift z as $(1+z)^4$.

Linear size, D is related to the age of the source, t as

$$D \propto t^{3/(5-\beta)} \tag{2.15}$$

For expansion into the ambient medium, we take $\beta = 2$ and therefore, there is a linear relation between source age t and linear size D, $t \propto D$. We then equate equations A1 and A3 using A2 to calculate the distance at which IC losses would begin to dominate over adiabatic losses. This distance depends on the initial jet power of the source and is given by

$$D_{IC} = \text{const} \times (\rho d^{\beta})^{-1/6} Q_{\rm jet}^{1/3} (1+z)^{-8/3} \tag{2.16}$$

where the constant is given by

$$\frac{m_e c^2 f_n f_p^{1/4} C (3 + a_1)}{14 f_L \sqrt{A} u^0_{\rm CMB} 150 \text{ MHz}} \tag{2.17}$$

The values of model parameters used in this study are shown in Table 2.2.

Table 2.2: Fiducial model parameters used in this study, taken from KB07.

Parameter	Value
A	4
ρ	10^{-22} kg m^{-1}
d	2 kpc at $z \leqslant 2$ $2 \times [(1+z)/3]^{-1.25}$ kpc at $z > 2$
$u^0_{\rm CMB}$	4×10^{-14} J m^{-3}
f_n	1.2×10^{12} s^2 kg^{-1} m^{-2}
f_p	0.11
C	1.5
a_1	3/2
f_L	$3.4 \times 10^{-17} \times 1/\sqrt{0.15}$ J$^{1/4}$ m$^{1/4}$ s^2 kg^{-1}

3 | A search for faint high-redshift radio galaxy candidates at 150 MHz

Ultra-steep spectrum (USS) radio sources are good tracers of powerful radio galaxies at $z > 2$. Identification of even a single bright radio galaxy at $z > 6$ can be used to detect redshifted 21cm absorption due to neutral hydrogen in the intervening IGM. Here we describe a new sample of high-redshift radio galaxy (HzRG) candidates constructed from the TGSS ADR1 survey at 150 MHz. We employ USS selection ($\alpha \leqslant -1.3$) in ~ 10000 square degrees, in combination with strict size selection and non-detections in all-sky optical and infrared surveys. We apply flux density cuts that probe a unique parameter space in flux density ($50 < S_{150} < 200$ mJy) to build a sample of 32 HzRG candidates. Follow-up Karl G. Jansky Very Large Array (VLA) observations at 1.4 GHz with an average beam size of 1.3 arcseconds ($''$) revealed $\sim 48\%$ of sources to have a single radio component. P-band (370 MHz) imaging of 17 of these sources revealed a flattening radio SED for ten sources at low frequencies, which is expected from compact HzRGs. Two of our sources lie in fields where deeper multi-wavelength photometry and ancillary radio data are available and for one of these we find a best-fit photo-z of 4.8 ± 2.0. The other source has $z_{\text{phot}} = 1.4 \pm 0.1$ and a small angular size ($3.7''$), which could be associated with an obscured star forming galaxy or with a 'dead' elliptical. One USS radio source not part of the HzRG sample but observed with the VLA nonetheless is revealed to be a candidate giant radio galaxy with a host galaxy photo-z of 1.8 ± 0.5, indicating a size of 875 kpc.

Based on:
Saxena A., Jagannathan P., Röttgering H.J.A., Best P.N., Intema H.T.
Zhang M., Duncan K.J., Carilli C.L. and Miley G.K.
MNRAS, 475, 5041 (2018)

3.1 Introduction

The discovery of high-redshift radio galaxies (HzRGs) has enabled extensive studies of large scale structure and galaxy evolution. HzRGs are among the most massive galaxies in the universe and are thought to be the progenitors of the massive ellipticals we observe today. HzRGs contain large amounts of dust and gas (Best et al. 1998b; Archibald et al. 2001; Carilli et al. 2002a; Reuland et al. 2004; De Breuck et al. 2010), are dominated by an old stellar population (Best et al. 1998a; Rocca-Volmerange et al. 2004; Seymour et al. 2007) and seen to have high star formation rates (Willott et al. 2003; McLure et al. 2004; Miley et al. 2006; Villar-Martín et al. 2007a; Seymour et al. 2008). Likely due to their large stellar masses, HzRGs are often found to be located in the centre of clusters and proto-clusters (Pentericci et al. 2000; Venemans et al. 2002; Röttgering et al. 2003; Miley et al. 2004; Hatch et al. 2011; Orsi et al. 2016). Miley & De Breuck (2008) summarise the properties of radio galaxies and their environments in their extensive review.

Radio galaxies at $z > 6$ can be used to study the epoch of reionisation (EoR) i.e. the epoch at which the universe makes a phase transition from being neutral to ionised. A bright radio source in the EoR provides a perfect background against which absorption by the neutral intergalactic medium can be observed. The 21cm hyper-fine transition line is redshifted into the low-frequency regime at $z \geqslant 6$ ($\nu < 200$ MHz) and the HI absorption features in the continuum of a bright radio source can be observed using current and next-generation telescopes such as the Low Frequency Array[1] (LOFAR), The Murchison Widefield Array[2] (MWA) and the Square Kilometer Array[3] (Carilli et al. 2002b; Furlanetto & Loeb 2002; Xu et al. 2009; Mack & Wyithe 2012; Ewall-Wice et al. 2014; Ciardi et al. 2015). Detection of even a single bright radio source at $z \geqslant 6$ enables studying the processes responsible for reionsing the universe in unparalleled detail.

Over the years, the highest redshift of a known radio galaxy has increased gradually. Starting with a detection at $z = 0.45$ (Minkowski 1960), it took another two decades for the discovery of radio galaxies out to $z \sim 1$ (Spinrad et al. 1977; Smith & Spinrad 1980). It was in the 90s that significant progress was made towards pushing the highest known redshift of radio galaxies, resulting in the discovery of the currently highest redshift radio galaxy known, at $z = 5.19$ (van Breugel et al. 1999). With state-of-the-art radio telescopes such as the Giant Metrewave Radio Telescope[4] (GMRT) and LOFAR, it is now possible to go deeper than ever before at low-frequencies, opening up a new parameter space for HzRG searches.

---

[1] www.lofar.org (van Haarlem et al. 2013)

[2] www.mwatelescope.org (Tingay et al. 2013a)

[3] www.skatelescope.org (Dewdney et al. 2009)

[4] http://www.gmrt.ncra.tifr.res.in (Swarup et al. 1991)

Most searches for HzRGs have relied on exploiting the ultra-steep spectrum (USS; spectral index, $\alpha < -1.3$, where for frequency ν and flux density S_ν, α is given by $S_\nu \propto \nu^\alpha$) search technique. Tielens et al. (1979) and Blumenthal & Miley (1979) found that optical identification fraction went down significantly for radio sources with steeper spectral indices. This was attributed to USS sources having higher redshifts and it is now generally observed that the spectral index of radio galaxies steepens at higher redshifts (Ker et al. 2012, and references therein). The true physical details of why this happens, however, are still under debate but the widely held view is that the $z-\alpha$ correlation is a result of a concave radio spectrum, i.e. flattening of the spectral index at lower radio frequencies, coupled with a radio K-correction. We refer the reader to Miley & De Breuck (2008) for a review on the possible causes of spectral index steepening at higher redshifts. Regardless, this technique has proven to be very successful in identifying HzRGs (Röttgering et al. 1994; Chambers et al. 1996; Blundell et al. 1999; De Breuck et al. 2000a; Afonso et al. 2011). USS selection, however, does not produce complete samples of HzRGs as the spectral index cut naturally excludes part of the complete sample (see Jarvis et al. 2009). Since the goal of this study is to extend the search for radio galaxies to higher redshifts and not necessarily produce complete samples, we still rely on USS selection for the purposes of this paper.

In addition to having an ultra-steep spectrum, HzRGs are also expected to have compact radio morphologies and the statistical decrease of angular sizes of radio sources with redshift has been known for a long time (Miley 1968; Nilsson et al. 1993; Neeser et al. 1995; Daly & Guerra 2002). More recently, Morabito et al. (2017) show that the decrease in size with redshift is also observed in deep radio observations at low frequencies. These compact radio sources of a possible high-z nature are often referred to as compact steep spectrum (CSS) sources and are generally a few arcseconds across. It is believed that CSS sources are in early stages of their lifetime, i.e. young (Fanti et al. 1995). Blundell & Rawlings (1999) showed that there is an 'inevitable youthfulness' associated with radio sources at high redshifts in a way that all observable HzRGs must be seen when their lobes are less than 10^7 years old. Further, Saxena et al. (2017) modelled the compactness of radio galaxies at $z \sim 6$ due to the denser cosmic microwave background at higher redshifts leading to increased inverse Compton losses, thereby shortening their lifetimes. Therefore, selecting compact radio sources as potential HzRG candidates is well justified.

Lastly, to optimise the selection of candidate HzRGs from large all-sky surveys, deep optical and infrared datasets over large areas on the sky are ideal. For example, Ker et al. (2012) showed that a K-band cut of 18.5 recovers almost all the currently known high-z radio sources and near infrared selection is very successful at isolating high-z radio galaxies than any selection based on radio properties alone. Therefore, selecting bright radio sources with steep spectral indices and small angular sizes that are also blank in the relatively shallow all-sky optical and/or infrared surveys has the potential effectively detect promising HzRGs candidates (Garn & Alexander 2008; Middelberg et al. 2011; Ker et al. 2012).

Perhaps one of the most well-studied sample of radio galaxies was put together by Seymour et al. (2007) and De Breuck et al. (2010), where they studied a sample of ~ 70 known high redshift radio galaxies to obtain detailed SEDs over a large wavelength range. Their sample, however, probes only the most powerful radio galaxies ($L_{\rm 500MHz} > 10^{27}$ W Hz^{-1}). Very little is known about the properties of less powerful radio galaxies as the samples of ultra-steep spectrum radio sources have mostly come from shallow all-sky surveys. In this work we present a sample of newly identified ultra-steep spectrum radio sources at 150 MHz using the new, deeper low-frequency survey carried out using the GMRT called TGSS ADR1 (Intema et al. 2017). Our sample aims to extend the studies of radio galaxies to lower radio powers. Probing this unique parameter space is essential to study the overall evolution of radio galaxies across cosmic time, as well as to reveal any underlying differences between the most and less powerful radio galaxies. Probing fainter radio flux densities is also a way to look for powerful radio galaxies at some of the highest redshifts.

In Section 3.2 we describe the data sets used to identify targets that probe a unique parameter space at low radio frequencies and describe our target selection methods. In Section 3.3 we present our follow-up VLA A-configuration observations at 1.4 GHz and 370 MHz of targets in our final sample. We describe the data reduction and imaging procedures. These observations yield accurate flux densities, morphologies and spectral indices. In Section 3.4 we present the multi-wavelength properties of sources in our sample and comment on a few individual sources that happen to lie in famous extragalactic fields and have a wealth of multi-wavelength data available. We discuss classes of radio sources that display an ultra-steep spectral index and that could potentially be present in our sample in Section 5.4. Finally, we summarise our findings in Section 3.6.

Throughout this paper we assume a flat ΛCDM cosmology with $H_0 = 67.8$ km/s/Mpc and $\Omega_m = 0.307$. These parameters are taken from the first Planck cosmological data release (Planck Collaboration et al. 2014).

3.2 Radio data sets and sample selection

3.2.1 TIFR GMRT Sky Survey (TGSS) Alternative Data Release at 150 MHz

The high-redshift radio galaxy (HzRG) candidates presented in this work are selected from the independent reanalysis of archival TIFR GMRT Sky Survey (TGSS) data called the First Alternative Data Release (ADR1; Intema et al. 2017). This is a survey of the 150 MHz radio sky using the Giant Metrewave Radio Telescope (GMRT) in India. The observations were centred at a frequency of 147.5 MHz with a bandwidth of 16.7 MHz.

This data release covers 36,900 sq. degrees of the sky between declinations of -53° and +90°. Each pointing has an integration time of 15 minutes and covers roughly 7 sq. degrees of the sky. The majority of pointings have a background noise level below 5 mJy/beam and a resolution of 25 arcseconds ($''$). The overall astrometric accuracy is better than $2''$.

3.2.2 VLA FIRST and NVSS at 1.4 GHz

The Faint Images of the Radio Sky at Twenty centimetres (FIRST) is a 1.4 GHz survey of the sky covering 10,000 square degrees (Becker et al. 1995; White et al. 1997). This survey was carried out using the NRAO Karl G. Jansky Very Large Array (VLA) in B-configuration acquiring 3 minute snapshots using 2×7 3-MHz channels centred around 1365 and 1435 MHz. The FIRST survey has a typical noise level of 0.15 mJy/beam and a resolution of $5''$. The astrometric reference frame of the radio maps is accurate to $0.05''$ with individual sources having 90% confidence error circles of $1''$ down to the survey threshold. There are ~ 90 sources per sq. degree at the 1 mJy/beam detection threshold.

The NRAO VLA Sky Survey (NVSS) is a continuum survey at 1.4 GHz, which covers the entire sky north of $-40°$ declination (Condon et al. 1998). The survey has a resolution of $45''$ and a completeness limit of about 2.5 mJy. The larger restoring beam makes this survey more sensitive to extended emission compared to FIRST, where the latter performs better for point sources. Therefore, FIRST and NVSS are highly complimentary to each other.

3.2.3 Target selection

To select HzRG candidates for this study, we use the region on the sky in TGSS ADR1 that is coincident with the footprint of the VLA FIRST survey at 1.4 GHz covering roughly 10000 sq. degrees. Further, we only include sources above a declination of $+10°$ to aid eventual follow-up observations with LOFAR. These

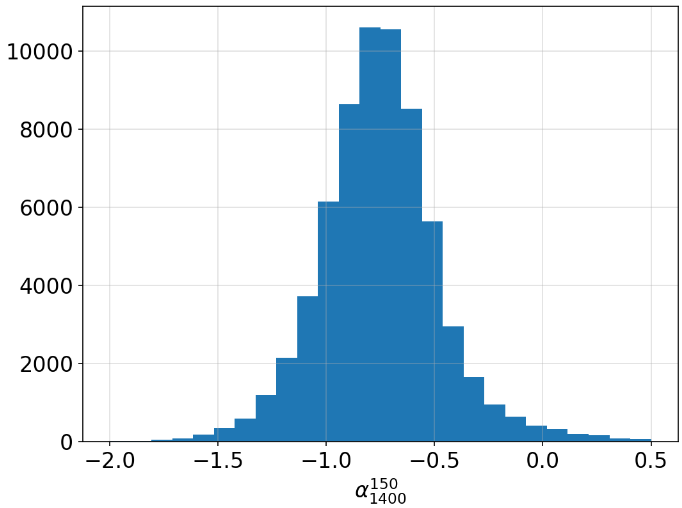

Figure 3.1: Spectral index distribution of all unresolved TGSS ADR1 sources matched with FIRST. The distribution peaks at -0.75, which is consistent with many previous studies of spectral index distribution. For further analysis in this study, we only consider sources with $\alpha_{1400}^{150} < -1.3$.

conditions give us an RA and Dec range of approximately $7\text{h} < \text{RA} < 18\text{h}$ and $10° < \text{Dec} < 70°$.

Angular size restriction

We introduce a size restriction when selecting potential HzRGs from TGSS ADR1 by selecting only compact, single component radio sources. The angular resolution of ADR1 is $25''$ but to account for errors, we use a more conservative size restriction by requiring the catalogued major axis to be $< 28''$. Next, all selected sources are matched with the FIRST catalogue using the position of the peak pixel in ADR1 and a conservative matching radius of $15''$, which ensures that the peak pixel of any matched counterpart lies within the TGSS beam size of $\sim 25''$. A conservative radius for single component radio sources should overcome the positional uncertainties introduced due to different resolutions of the two surveys. After matching, another size restriction is introduced by only retaining sources that are compact in FIRST, which could include either point sources or compact, multiple component sources. This is done by selecting only sources with a deconvolved major axis of less than $10''$ in the FIRST catalogue. This leaves us with sources with angular sizes in the range $5'' - 10''$ in FIRST, in line with the expected HzRG sizes (Miley & De Breuck 2008; Saxena et al. 2017). To ensure robust detections at 1.4 GHz, we only select sources with at least 8σ detection in FIRST, i.e. sources brighter than 1.2 mJy at 1.4 GHz. This results in a sample of 65,996 sources. Next, we determine spectral indices of all the ADR1-FIRST matched sources between 150 MHz and 1.4 GHz. The spectral index distribution of the matched unresolved sources is shown in Figure 3.1.

Ultra-steep spectral index selection

Owing to the success of selecting sources with steep spectral indices to identify HzRGS, we employ ultra-steep spectrum (USS) selection in ADR1 by selecting sources with spectral indices between 150 MHz and 1.4 GHz steeper than -1.3 ($\alpha^{150}_{1400} < -1.3$). This results in 1564 sources, which is roughly 2% of the total number of matched, unresolved sources initially part of the sample. To demonstrate that this technique increases the probability of finding high-redshift radio sources, we show the optical ID (SDSS) fraction as a function of spectral index for all TGSS-FIRST matched sources in Figure 3.2. Any source detected in FIRST with an optical counterpart within $5''$ from its peak pixel was assumed to have a potential optical ID. We elaborate on the optical and infrared counterpart identification process in greater detail in the following sections. Clearly, the ID fraction decreases with increasingly steeper spectral indices, suggesting that the hosts of USS sources are fainter than the detection limit in an optical survey complete to a certain flux limit and therefore, are likely to be more distant. Towards the steepest spectral indices ($\alpha < -1.6$) we suffer from low number statistics. The overall trend can be interpreted due to a $z - \alpha$ relation (Miley & De Breuck 2008).

A point to be noted is that the TGSS ADR1 is prone to small flux density variations on scales of several degrees, owing to the observing strategy implemented (Intema et al. 2017). de Gasperin et al. (2017) found this variation to bias the spectral indices in certain regions of the sky by values < 0.06, which was also reported by Hurley-Walker (2017). For the purposes of this study, however, this result does not significantly influence the selection as the spectral indices of sources of interest would be expected to remain ultra-steep even after taking the variation into account.

Flux limits -- probing a unique parameter space

Next, we apply an upper flux limit at 1.4 GHz, such that none of our sources could have been detected in previous large area HzRG searches using the ultra-steep spectrum technique, such as the De Breuck et al. (2000a) sample that consists of 669 USS sources with $S_{1400} > 10$ mJy. The deepest lowest frequency data

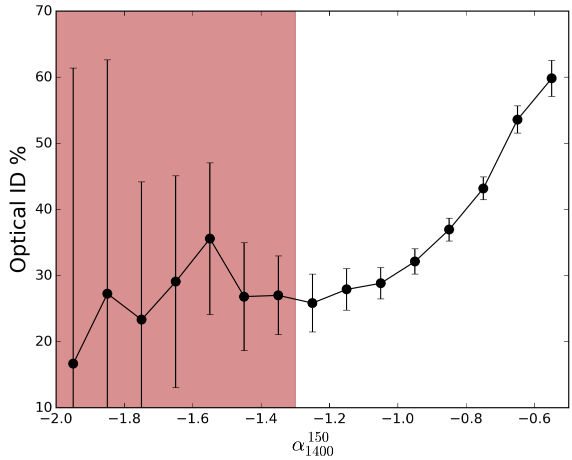

Figure 3.2: Optical ID fraction (using the band-merged SDSS DR12 catalogue) as a function of radio spectral index with Poissonian uncertainties in each spectral index bin. Clearly the ID fraction for sources with steeper spectral indices is lower. Since SDSS and PS1 probe mainly the low redshift universe, optical identification will be more common for lower redshift galaxies and the decreasing ID fraction for sources with steeper spectral indices can be interpreted as a redshift-spectral index correlation.

in their analysis comes from the Westerbork Northern Sky Survey (WENSS) at 92 cm (325 MHz; Rengelink et al. 1997). We select only sources with $S_{1.4} < 10$ mJy in FIRST that ensures that none of these sources would have been detected in WENSS and therefore, were missed by the De Breuck et al. (2000a) sample. These flux limits result in the flux densities at 150 MHz lying between 50 and 200 mJy, which ensures robust detections in TGSS ADR1. Applying these flux limits resulted in 817 sources remaining in our sample.

The high resolution provided by the FIRST survey is prone to missing extended emission from radio sources, as this emission is 'resolved out' from the final image. Therefore, to ensure that the sources that we have selected are truly compact at 1.4 GHz, we look for their counterparts in the lower resolution NVSS survey at the same wavelength. We use a more conservative matching radius of 20″ to account for positional offsets of the peak pixel owing to the difference in resolution between the two surveys. The minimum flux density requirement in FIRST ensures that all our sources must also be detected in NVSS (although many of them are very faint). Enforcing a match in NVSS gives the added advantage of eliminating variable sources from our sample, since FIRST and NVSS were carried out at different epochs and having consistent flux densities in both these surveys should dramatically reduce chances of variability. After matching, we compare the integrated flux densities in FIRST and NVSS and keep only sources with comparable flux densities, i.e., $S_{\rm FIRST}/S_{\rm NVSS} = 0.76-1.3$, roughly within 1σ agreement. This further reduced the sample size to 588 sources.

Optical and infrared non detections

As mentioned before, searching for radio sources with no optical and/or faint infrared counterparts greatly assists in isolating high-redshift radio sources. Therefore, we focus on only those sources in the remaining sample that do not have any obvious counterparts in available all-sky optical and infrared surveys. To do this, we look for optical counterparts for radio sources in the Sloan Digital Sky Survey Data Release 12 (SDSS; Alam et al. 2015b) band-merged catalogue, which covers the entire FIRST footprint in the *u, g, r, i* and *z* bands and in the PanSTARRS1 survey catalogue (PS1; Chambers et al. 2016a), providing photometry in *g, r, i, z* and *y* bands over 3π steradian of the sky.

We use the FIRST positions for optical counterpart identification with a strict matching radius of 5″, which is the resolution of the FIRST survey. It is important to note that we are not interested in the true optical counterpart for the purposes of this study. Finding a counterpart within a conservative matching radius of 5″ is a way to reject radio sources that are not blank in the all-sky optical surveys. As the redshift distribution of galaxies in SDSS peaks at around $z = 0.3$ and there are very few galaxies at $z > 1$ even at the faintest end (Sheldon et al. 2012), we use optical detections to rule out low redshift radio galaxies and for further analysis, we only select sources with no potential optical counterparts in both SDSS and PS1.

It is possible that intrinsically redder objects at $z > 0.3$ may be missed by SDSS and therefore, we match the remaining sources with the ALLWISE survey, which builds upon the work of the *Wide-field Infrared Survey Explorer (WISE*; Wright et al. 2010b*)* mission covering the entire sky at wavelengths of 3.4, 4.6, 12 and 22 µm. The median photometric redshift for faint red objects with $R < 20.0$ peaks at around $z = 0.3$ (Bilicki et al. 2014) and may be slightly higher for even fainter red objects, so we retain only those sources in the sample with no counterparts in ALLWISE either, using a matching radius of 6″, owing to the lower resolution of ALLWISE. This ensures that none of our radio selected sources have optical or infrared counterparts in the available all-sky surveys and are very likely not low redshift radio galaxies.

Final visual inspection of all sources that satisfied the above mentioned criteria was carried out to ensure that they are a) unresolved or barely resolved in FIRST, b) truly compact and c) have no optical or infrared counterparts. At times the FIRST

Table 3.1: Number of sources and fraction of the total matched sources between TGSS ADR1 and FIRST at every stage of selection. We start our selection by only considering unresolved sources in TGSS ADR1.

Selection step	No. sources	Fraction
Unresolved TGSS-FIRST matches	65,996	100%
$\alpha_{1400}^{150} < -1.3$	1564	2%
Flux limits + consistent NVSS	588	0.9%
No SDSS and PS1 + no WISE	32	0.05%

image contained an additional fainter radio component very close to the peak pixel that was reported in the catalogue. In such cases, we measure the total flux density of the radio emission and update the FIRST flux for spectral index calculation. In some cases the FIRST flux was taken out of the $S_{\rm FIRST}/S_{\rm NVSS} = 0.76 - 1.3$ selection range, but these sources were nevertheless retained. Such isolated cases, however, did not result in the recalculated spectral indices becoming less steep than -1.3. There was one source in particular (USS422) that had an ultra-steep spectral index from FIRST ($\alpha = -1.8$) but was relatively flat when compared with NVSS ($\alpha = -1.0$). This source was unresolved in both FIRST and NVSS. This meant that this particular source did not strictly adhere to the HzRG selection criteria, but the intriguing nature of radio emission suggesting large scale diffuse emission led us to include this source in the follow-up VLA observations presented in the next sections.

The strict selection criteria resulted in 32 promising HzRG candidates. In Figure 3.3 our sample probes a completely new parameter space aimed at detecting radio galaxies in or very close to the epoch of reionisation. The grey points are sources from De Breuck et al. (2000a), where we have used the reported spectral index for each source between 325 and 1400 MHz to scale their flux densities to 150 MHz. We show the fraction of the initial sample remaining after each selection step in Table 3.1.

The convention for working names used for sources in this study is of the form ‘USSXY’ where XY is the identification number that was assigned to radio sources in an early version of the TGSS ADR1 source catalogue. We have chosen to continue using these working names for all practical purposes in this paper, but also give the official ADR1 catalogue names in the source table presented. The identification numbers are not necessarily correlated with any other property of the sources.

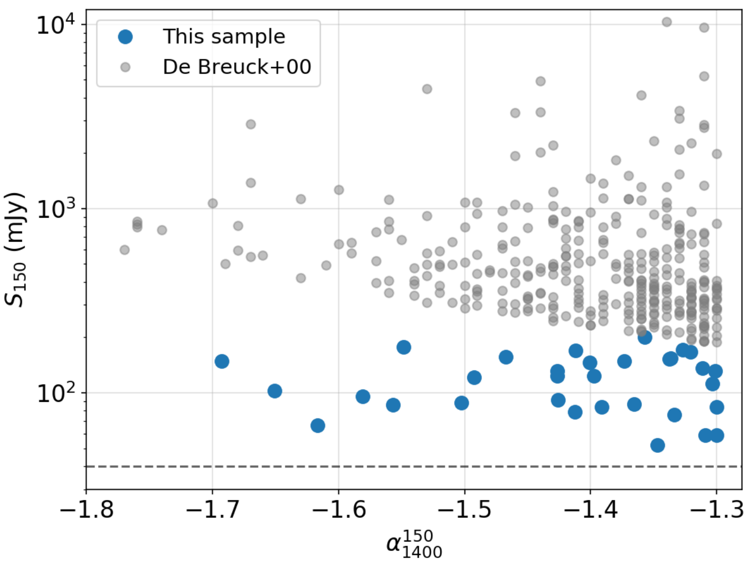

Figure 3.3: The flux-spectral index parameter space probed by our sample (blue points). Also shown in grey are USS candidates from De Breuck et al. (2000a) with their flux densities scaled to 150 MHz. The dashed line is the 8σ detection limit in TGSS ADR1 that we enforced to ensure robust detections. Clearly, our sample goes fainter in flux density and probes a completely new parameter space that has the potential to discover highest redshift radio galaxies.

3.3 VLA L and P-band observations

3.3.1 Objectives

The primary objective of follow-up VLA observations (Project ID: VLA/ 16B-309) in A-configuration was to obtain accurate radio positions and morphologies (L-band) and look for signs of spectral curvature (P-band) for sources in our final sample. With an average resolution of 1.3″ provided by the L-band (1.4 GHz) it is possible to get sub-arcsecond positional accuracy for the identification of the galaxy hosting the radio source. This further enables blind spectroscopy at the radio position without requiring the need to identify a counterpart in deep optical/IR images. Due to constraints on target visibility, we observed 31 out of 32 HzRG candidates and the potential diffuse source (USS422) at 1.4 GHz. The one source that was left out lies in the equatorial strip that is part of the FIRST Southern Sky Coverage and could not be accommodated in the observing blocks containing sources from the Northern Sky Coverage. Owing to time and visibility constraints, we could only observed 17 sources in P-band (370 MHz).

3.3.2 Observations and data reduction

The observations were carried out in A-configuration. The sample in L-band was observed in two blocks of 4 hours each, separated by 2 hours in LST to optimise UV coverage for scans on each source. The typical on-source time was 5 minutes in each observing block, giving a total of 10 minutes of exposure per source. The first block was observed on 28 November 2016 and the second on 28 December 2016. The observations were taken in standard L-band configuration using 27 antennas with 1024 MHz bandwidth (16 sub-bands $\times$ 64 MHz). The flux densities were calibrated using the primary VLA calibrator 3C286 observed in the middle of the observing block. Groups of 3 or 4 sources in RA were created and a suitable phase calibrator was identified for each RA group.

The P-band observations were carried out on 25 January 2017. These were taken in standard configuration with a bandwidth of 200 MHz. The exposures were much shorter, with a single 70 second on-source exposure per source. This short exposure should be enough to detect all targets with a SNR > 10, assuming the spectral index remains more or less constant at intermediate frequencies between 150 and 1400 MHz.

Initial calibration and data reduction was carried out using the Common Astronomy Software Applications (CASA) package. The VLA data reduction pipeline provided by NRAO[5] was used to flag and calibrate the measurement sets. The

[5] available at

CASA command *rflag* was implemented on the calibrated datasets to flag most of the remaining radio frequency interference (RFI). Final images were produced using the *clean* command in CASA, using either uniform or 'robust' weighting scheme. For L-band images we used a cell size varying between $0.25 - 0.4''$ (to ensure that at least 3-5 pixels fall within the beam size). For P-band the chosen cell size was $1.2''$. The final images have an average resolution of $1.3''$ in L-band and $5.6''$ in P-band. The images have an average rms level of 60 μJy/beam in L-band and 1.8 mJy/beam in P-band, which is close to the expected theoretical noise levels. The ionosphere for P-band observations was fairly stable and ionospheric TEC corrections were applied using the *gencal* task in CASA.

3.3.3 Flux densities and morphologies

Flux densities and angular sizes of all sources imaged were then measured using PyBDSF[6] (the Python Blob Detector and Source Finder), which is a tool designed to identify sources in a radio image and extract meaningful properties. We use a threshold of 5σ to identify 'islands' of pixels surrounding the peak pixel. These identified pixels are then fitted with Gaussian components to determine flux densities, positions and de-convolved angular sizes. More details about the source finding algorithm can be found in the PyBDSF documentation.

In Table 3.5 we report the source properties derived from the L-band images using PyBDSF with the above mentioned parameters. For sources that are fitted with multiple gaussian components by PyBDSF, we report the flux density of each component separately. Angular sizes of sources with multiple components are determined by measuring the separation between the peak positions of the components. The distribution of angular sizes is shown in Figure 3.4. We note that the angular sizes of a large majority of our sources are compact (LAS $\leqslant 10''$, as expected from our selection criteria) and in line with predictions for HzRGs by Saxena et al. (2017) assuming $z > 2$, which is promising. We find that 15 of the observed 32 sources (57% of the sample) are fitted with only one Gaussian component by PyBDSF. A further 14 sources (41%) were identified to have two components, one source with three components and another source with four components. For the source USS422, the wide-field image revealed the presence of a candidate giant radio galaxy (GRG). Only one hotspot of this candidate GRG was included in our sample. The angular separation between the two lobes of this galaxy is ~ 1.7 arcminute ($'$). We discuss the properties of this source in Section 4.

https://science.nrao.edu/facilities/vla/data-processing/pipeline/

[6]http://www.astron.nl/citt/pybdsf/index.html

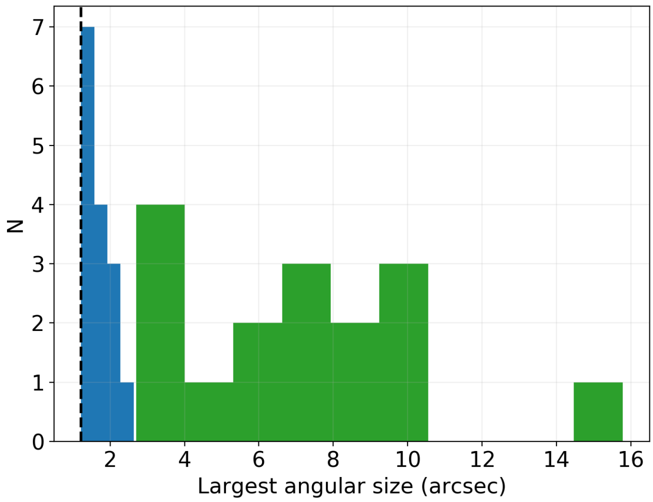

Figure 3.4: Largest angular size (LAS) distribution determined from our VLA observations of targets in the final sample with an average beam size of 1.3″. We find that 15 out of the 31 candidate HzRGs observed are fitted with a single component (blue). There is a wide range of LAS values for sources fit with multiple components (green).

We report flux densities measured at 370 MHz for sources that were also observed in the P-band in Table 3.2. We then calculate the spectral indices and investigate the shape of the radio spectra constructed using data at frequencies of 150, 370 and 1400 MHz. The resulting radio 'colour-colour' plot is shown in Figure 3.5. We find evidence of spectral flattening at lower frequencies in the spectra of 10 out of 17 sources, which is expected from smaller sized HzRGs as they are younger and expand into a denser environment (Callingham et al. 2017). Three sources show a steepening of their spectrum at low frequencies. The radio SED of four sources has a constant spectral index from 150 MHz all the way to 1.4 GHz, within the uncertainties.

We show contour maps of all sources imaged with the VLA in Appendix B. The contours begin at 0.25 mJy and are a geometric progression of $\sqrt{2}$, i.e. for every two contours the flux increases by a factor of 2. The VLA beam used to image each source is shown in the bottom-left part of the contour map.

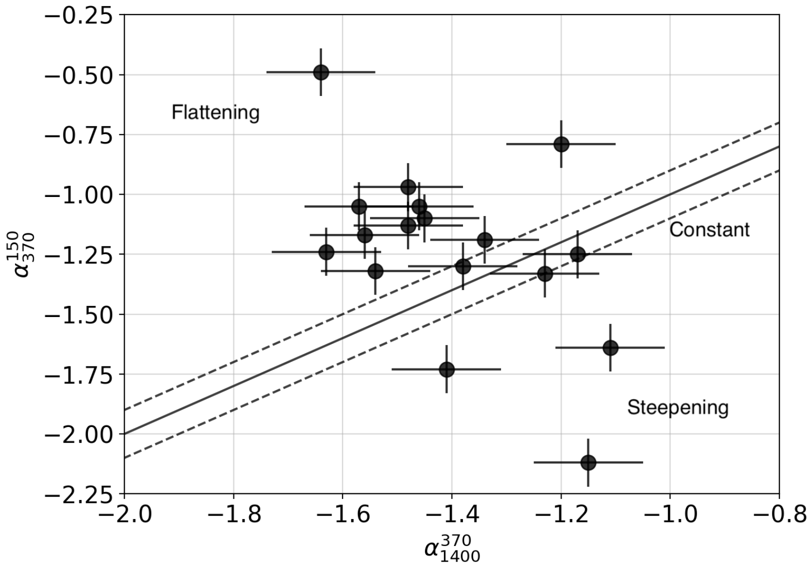

Figure 3.5: A radio colour-colour plot, showing spectral indices from 370 to 1400 MHz on x-axis and 150 to 370 MHz on y-axis. The solid line marks constant spectral index at both radio colours, with the dashed lines representing errors of 0.1. We mark the regions where we observe 'Flattening', 'Steepening' and 'Constant' spectral indices for sources observed in both L- and P-bands.

Table 3.2: Flux densities and spectral indices for the subset of the sample also observed at 370 MHz (VLA P-band). The errors on the spectral index determination have been rounded off to the closest one decimal place value. In the last column we comment on the type of radio SED displayed by each source, where 'Steepening' indicates a steeper spectral index at low frequencies, 'Flattening' indicates flatter spectral index at low frequencies and 'Constant' indicats a constantly steep spectral index, within the uncertainties. The sources are listed in order of Right Ascension in this table and the full source table with more details in shown in Appendix 1 (Table 3.5).

Name	S_{150} (mJy)	S^{tot}_{370} (mJy)	$S^{tot}_{1.4}$ (mJy)	α^{150}_{370}	$\alpha^{370}_{1.4}$	Spectral type
USS206	84 ± 16	65.6 ± 4.0	7.3 ± 0.1	-0.49 ± 0.1	-1.64 ± 0.1	Flattening
USS182	146 ± 30	38.4 ± 4.6	8.5 ± 0.1	-1.33 ± 0.1	-1.23 ± 0.1	Constant
USS31	149 ± 30	35.4 ± 2.3	4.8 ± 0.1	-1.73 ± 0.1	-1.41 ± 0.1	Steepening
USS188	166 ± 33	65.0 ± 2.5	9.2 ± 0.1	-1.05 ± 0.1	-1.57 ± 0.1	Flattening
USS309	83 ± 17	41.3 ± 3.7	8.4 ± 0.1	-0.79 ± 0.1	-1.20 ± 0.1	Flattening
USS27	111 ± 22	37.8 ± 3.1	7.6 ± 0.1	-1.25 ± 0.1	-1.17 ± 0.1	Constant
USS36	123 ± 25	37.9 ± 3.3	6.0 ± 0.1	-1.30 ± 0.1	-1.38 ± 0.1	Constant
USS273	154 ± 31	61.1 ± 3.1	7.4 ± 0.1	-1.05 ± 0.1	-1.57 ± 0.1	Flattening
USS483	89 ± 18	29.2 ± 2.8	3.3 ± 0.1	-1.24 ± 0.1	-1.63 ± 0.1	Flattening
USS46	87 ± 17	35.6 ± 2.5	4.9 ± 0.1	-0.97 ± 0.1	-1.48 ± 0.1	Flattening
USS410	96 ± 19	31.6 ± 2.6	3.7 ± 0.1	-1.32 ± 0.1	-1.54 ± 0.1	Flattening
USS18	131 ± 26	46.1 ± 2.4	5.7 ± 0.1	-1.17 ± 0.1	-1.56 ± 0.1	Flattening
USS172	124 ± 25	42.0 ± 4.0	7.1 ± 0.1	-1.19 ± 0.1	-1.34 ± 0.1	Constant
USS159	149 ± 30	56.4 ± 2.8	8.0 ± 0.1	-1.10 ± 0.1	-1.45 ± 0.1	Flattening
USS253	156 ± 31	35.8 ± 3.0	8.1 ± 0.1	-1.64 ± 0.1	-1.11 ± 0.1	Steepening
USS312	79 ± 16	11.6 ± 2.5	2.5 ± 0.1	-2.12 ± 0.1	-1.15 ± 0.1	Steepening
USS268	92 ± 18	33.3 ± 2.2	4.6 ± 0.1	-1.13 ± 0.1	-1.48 ± 0.1	Flattening

3.4 Multi-wavelength properties and interesting sources

3.4.1 Optical and IR photometry

To gain a better understanding of the average properties of galaxies in our sample, we stack the optical and infrared photometry from publicly available surveys. Stacking analysis works best for galaxies with similar properties and since our galaxies are expected to be distributed over a range of redshifts, stacking photometry and photometric redshift determination may not yield a very accurate description of our sample. However, in order to gain a broad idea of the potential redshift space that our sample is probing, we obtain a photometric redshift using stacking anyway.

To do this, we first create postage stamp cutouts in available optical and infrared bands for all 32 sources in our sample. These cutouts are centred on the expected position of the optical counterpart, which was the flux-weighted peak pixel position of the radio emission for single component sources and the position of the pixel that was most likely to represent the expected position of the host galaxy chosen through visual analysis for radio sources with two (or more) components. We then perform sigma-clipped stacking of all the cutouts in each optical and infrared band in the following way. We calculate sigma-clipped statistics, where pixels above 5-sigma were discarded after the initial calculation of the mean and median values for each image. We then mask the pixels that are brighter than 10σ (where σ is the standard deviation obtained from sigma-clipped statistics) and then stack the images. We ensure that the pixels containing the expected position of the host galaxy are never masked in this process.

Aperture photometry is then performed using PHOTUTILS[7] on the central pixels of the stacked images using an aperture with diameter $2''$. This aperture size should take care of any uncertainty introduced when selecting the expected position of the optical host galaxy. Further, we place 100 apertures of $2''$ on the stacked image to obtain an estimate of the background flux or noise. When the central aperture flux is lower or equal to the noise estimated from random apertures, we report the 3σ limit on the non-detection. We elect to use PanSTARRS1 (PS1; Chambers et al. 2016b) for redder optical bands (*i, z, y*) as they are deeper than SDSS. We then perform aperture corrected photometry in the *WISE* bands *W1* and *W2* using data from the ALLWISE release. The point-spread function of *WISE* is roughly $6''$ in *W1* and *W2* bands and we use an aperture of size $7.2''$ for both these bands. The bands *W3* and *W4* are shallow and we do not see any evidence of detections after stacking. Therefore, we do not include them in this analysis. The magnitudes, both

[7] https://photutils.readthedocs.io/en/stable/index.html

Table 3.3: Stacked photometry (in AB mags) of the final USS sample from SDSS, PS1 and ALLWISE surveys. The lower limits indicate 3σ limits on the background flux for bands where the aperture flux is lower than or equal to the background flux.

Filter	Magnitude (AB)
SDSS u	> 23.15
SDSS g	> 23.88
SDSS r	> 23.15
PS1 i	22.8 ± 0.2
PS1 z	> 22.6
PS1 y	> 21.5
WISE $W1$	19.56 ± 0.2
WISE $W2$	19.05 ± 0.2

limits and detections, determined from the stacking analysis in the SDSS, PS1 and ALLWISE bands are shown in Table 3.3.

We then convert the AB magnitudes to fluxes and derive a photometric redshift by fitting the Brown et al. (2014) SED template using EAZY (Brammer et al. 2008). The redshift grid used ranges from 1.5 to 6.5 with a step size of 0.05. After applying a Bayesian apparent magnitude prior, the best-fit SED gives a photometric redshift of 2.95, with one-sigma confidence levels ranging from $1.0 - 5.5$. We note that $z > 6$ fits are within the 3-sigma confidence levels. We also find that fitting other SED templates using EAZY gives us similar photo-z estimates.

3.4.2 Comments on interesting sources in the sample

In this section we explore the possible nature and properties of a few sources that happen to lie in well-studied extragalactic fields, resulting in the availability of ancillary data at different wavelengths.

USS410 in Lockman Hole field

One source in our sample, USS410, lies in the Lockman Hole field. With the availability of deep LOFAR data at 150 MHz in this region (Mahony et al. 2016), we compare the TGSS ADR1 and LOFAR 150 MHz flux densities for this source and find them to be within 5% of each other. Additionally, LOFAR LBA (60 MHz) observations in this region did not detect this source down to a 5σ flux density limit of 100 mJy. This places its low-frequency spectral index at $\alpha_{150}^{60} > -0.05$, indicating a sharp spectral turnover at low frequencies (Mahony et al. 2016) and suggesting signs of synchrotron self-absorption or free-free absorption (Callingham et al. 2015, and references therein). Deep radio observations are also available

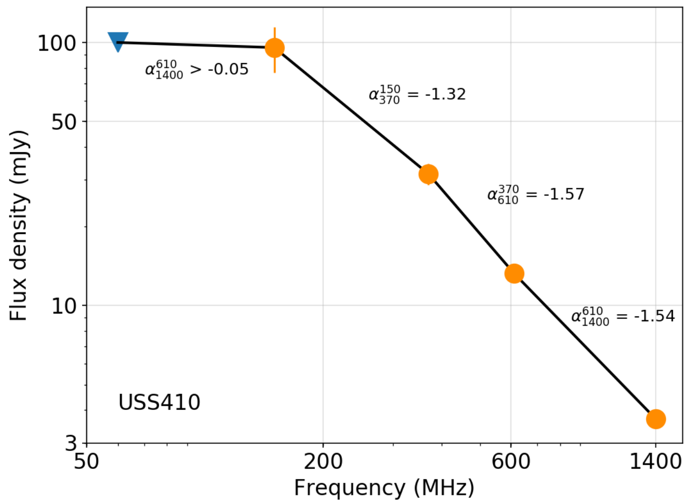

Figure 3.6: The radio SED for USS410 from 60 MHz to 1400 MHz. Also shown are the spectral indices measured between data available for this source at various radio frequencies. The error bars on the higher frequency data points are smaller than the symbol size, and therefore may not be clearly visible. There is a clear spectral turnover between 60 (Mahony et al. 2016) and 150 MHz, whereas the spectral index remains consistently ultra-steep from 150 to 610 MHz (Garn et al. 2010), and from 610 to 1400 MHz. The potential high-z nature of the host galaxy (Figure 3.7) makes USS410 a candidate peaked spectrum source at high redshift.

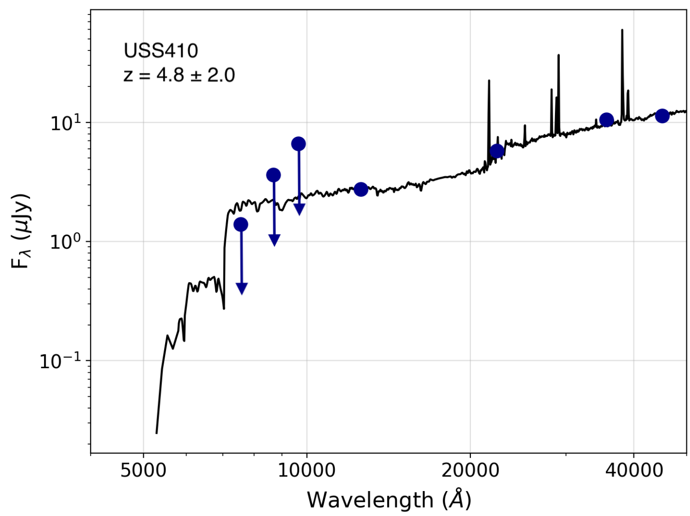

Figure 3.7: Best-fit SED (observed frame) with a photometric redshift of $z = 4.8 \pm 2.0$ obtained for USS410 in the Lockman Hole field. Lower redshift solutions cannot formally be ruled out yet. SED templates by Brown et al. (2014) were used for the fitting. The photometry is obtained from upper limits from PS1 (i, z, y) and detections from UKIDSS DXS (J, K) and *Spitzer* IRAC 3.6 and 4.5 μm. The error bars on the detections are smaller than the symbol size and therefore, not visible. Fits resulting from excluding upper limits yield the same photometric redshift.

at 610 MHz (Garn et al. 2010) with a resolution of $6'' \times 5''$ and USS410 has a detection with a flux density of 13.26 ± 0.23 mJy. With the addition of L- and P-band data that we obtained, we are able to constrain well the radio SED of this particular source. We show the SED from 60 MHz all the way to 1.4 GHz, indicating measured spectral indices between all available frequencies in Figure 3.6. Clearly, USS410 remains an ultra-steep spectrum source from 150 to 1400 MHz and undergoing a dramatic turnover at frequencies between 60 and 150 MHz.

USS410 was detected in the UKIDSS Deep Extragalactic Survey (DXS) carried out using the UKIRT telescope (Dye et al. 2006), with faint detections in both J and K bands with magnitudes of 22.8 $\pm$ 0.1 and 22.0 $\pm$ 0.1 AB, respectively. There are also faint detections in the Spitzer IRAC 3.6 and 4.5 mircon bands from the SWIRE coverage in this field (Surace et al. 2005). The 3.6 micron flux density is 10.5 ± 0.6 μJy and 4.5 micron flux density is 11.3 ± 0.8 μJy. Fitting an SED to non-detections in the PS1 *i,z,y* bands and detections in J, K, IRAC1 and IRAC2 bands, we derive a photometric redshift of $z_{\rm phot} = 4.8 \pm 2.0$, although solutions at lower redshifts and at $z > 5$ are not formally excluded (Figure 3.7). Further, following the tight correlation that exists between the K magnitude and redshift of high redshift radio galaxies (the $K - z$ relation; Lilly & Longair 1984; Jarvis et al. 2001b; Willott et al. 2003), the redshift of this particular radio galaxy is consistent with $z > 4$.

USS410 is unresolved in the VLA image, constraining the size to less than 8 kpc. Further, the turnover of the radio SED between 60 and 150 MHz makes it a possible megahertz-peaked spectrum (MPS) source at high-z. Follow-up spectroscopy is essential to reveal the nature of the host galaxy. The 1.4 GHz VLA image along with PS1 z UKIDSS J and K and the two IRAC bands are shown in Figure 3.8.

USS7 in ELAIS-N1 field

Another source, USS7, was identified in the ELAIS-N1 field. With the recent data release of the Hyper Suprime-Cam Subaru Strategic Program (HSC SSP; Aihara et al. 2017) this source was found to be detected in all of the HSC-SSP bands. Further, there were detections in the J and K bands in the UKIDSS DXS. Using the available photometric information, we derive a fairly robust photometric redshift of 1.4 ± 0.1, using SED templates from Brown et al. (2014), which is shown in Figure 3.9. The available photometry for this source along with USS410 is shown in Table 3.4.

The VLA image revealed a two-component radio morphology, with the near IR counterparts lying right between the two radio components, thereby increasing the likelihood of it being the true host of this radio galaxy. The angular separation

Table 3.4: Known optical and infrared photometry (in AB mags) for USS410 in the Lockman Hole field and USS7 in the ELIAS-N1 field (photometric redshift of $z = 1.4 \pm 0.1$).

Target	Filter	Magnitude (AB)/Flux density
USS410	J	22.8 ± 0.1
	K	22.0 ± 0.1
	IRAC 3.6 µm	10.5 ± 0.6 µJy
	IRAC 4.5 µm	11.3 ± 0.8 µJy
USS7	g	24.4 ± 0.1
	r	24.4 ± 0.2
	i	23.6 ± 0.1
	z	23.1 ± 0.2
	y	22.4 ± 0.1
	J	21.9 ± 0.1
	K	21.1 ± 0.1

between the two radio components is 3.7″. GMRT observations at 610 MHz with a resolution of $6.1''$ in this field have led to the detection of USS7 with a flux density of 18.6 ± 0.1 mJy (A. R. Taylor, private communication). This additional point on the radio SED reveals its spectral index to be consistently ultra-steep, with $\alpha_{610}^{150} = -1.34$ and $\alpha_{1400}^{610} = -1.30$. In contrast to what is observed for USS410, there is evidence of a slight steepening of the spectral index at lower radio frequencies. The K-corrected radio luminosities at 150, 610 and 1400 MHz are $\log L_{150} = 27.8$, $\log L_{610} = 27.0$ and $\log L_{1400} = 26.5$ W Hz^{-1}, respectively.

We show the radio image, along with HSC SSP z, and UKIDSS J and K images in Figure 3.10. The faint optical and infrared photometry combined with bright radio flux density at low frequencies and an ultra-steep spectral index suggest that USS7 could be part of an optically-faint, radio-loud, obscured AGN population. The optical faintness could also be attributed to the presence of a low accreting AGN.

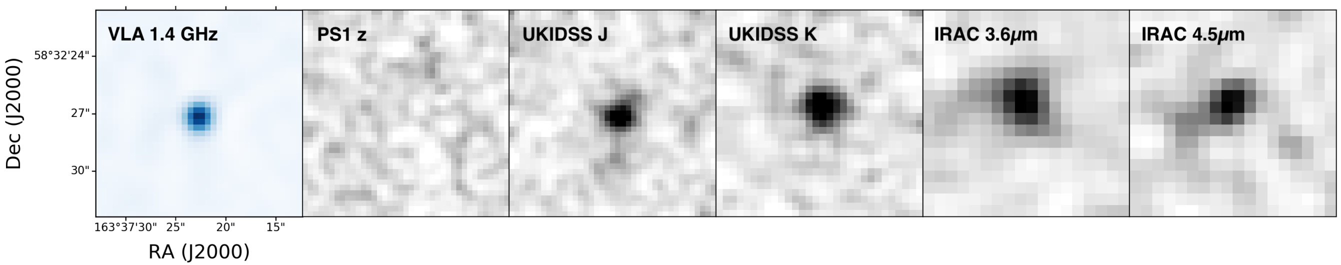

Figure 3.8: VLA 1.4 GHz images of the Lockman Hole source USS410, with PS1 z, UKIDSS J and K and IRAC 3.6 and 4.5 μm bands. USS410 remains unresolved even with a beam size of $1.1''$. There is no detection in PS1 z band down to 22.3 AB. The best-fit photometric redshift is calculated to be 4.8 ± 2.0 (Figure 3.7). Further, following the $K - z$ relation for radio galaxies (Willott et al. 2003), the K-band magnitude is consistent with a $z \geqslant 4$ host galaxy

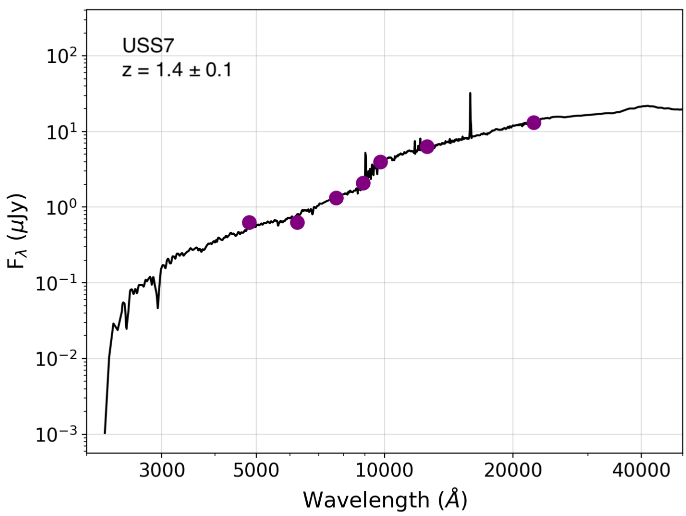

Figure 3.9: Best-fit SED (observed frame) with a photometric redshift of $z = 1.4 \pm 0.1$ obtained for USS7 in the ELAIS-N1 field. SED templates by Brown et al. (2014) were used for the fitting. The photometry is obtained from HSC-SSP (g, r, i, z, y) and UKIDSS DXS (J, K). The error bars on the detections are smaller than the symbol size and therefore, not visible.

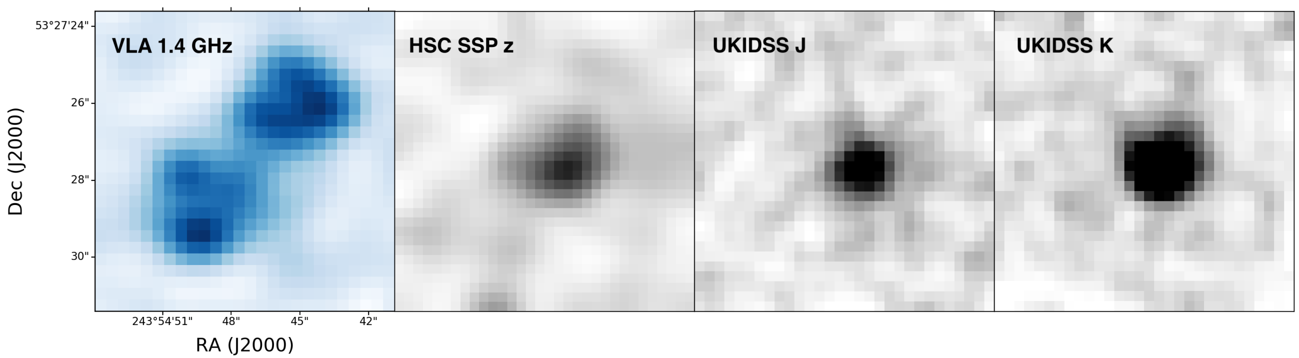

Figure 3.10: VLA 1.4 GHz image of the ELAIS-N1 source USS7, with HSC SSP z, and UKIDSS J and K bands. USS7 is resolved in the VLA map with a 2-component morphology. There is no detection in PS1 z band but the source is detected in UKIDSS J and K bands. Further detections for this galaxy are found in the HSC-SSP (Table 3.4), with a photometric redshift of 1.4 $\pm$ 0.1. The extent of the radio emission is around $6''$.

USS422 - candidate giant radio galaxy

This particular source appears to be point-like and very faint in the FIRST image. However, in the lower resolution NVSS image it appears to be much brighter, indicating presence of extended emission. Due to the very steep spectral index determined using flux density from FIRST, we decided to observe this source with the VLA, even if it did not adhere to our HzRG sample selection criteria.

The wide field VLA image revealed the presence of an additional northern lobe of what seems like a giant radio galaxy. Giant radio galaxies represent an extreme class of active galaxies with typical sizes in the range $\sim 0.7 - 5$ Mpc (Dabhade et al. 2017, and references therein). Figure 3.12 shows the VLA 1.4 GHz radio contours overlaid on the z-band image from PanSTARRS1. Blob 'A' was initially selected in our sample as a USS source. We believe 'B' to be emission from the core of this radio galaxy, as it aligns well with the two lobes. It is not entirely clear whether 'C' is actually part of this system or is a background source. If it is indeed part of the system then it could be classified as a 'knot' in the radio jet. 'D' is the northern lobe which was not identified as an USS source. The two lobes 'A' and 'D' are separated by more than an arcminute and thus, make this galaxy a candidate giant radio galaxy (GRG). The total extent, measured by drawling a straight line from the edge of the northern lobe to the edge of the southern lobe passing through the core is $1.7'$.

We performed aperture photometry ($2.5''$ diameter) in all PS1 bands at the position of component B. We also find counterparts in the *WISE W1* and *W2* bands. For the *WISE* images, we use cutouts from the unblurred coadds (unWISE; Lang 2014), which are better suited for aperture photometry. The associated galaxy in these images, however, is blended with another source $\sim 3''$ away. To get over the potentially overestimated flux density, we set the aperture size to be the PSF of the WISE images ($\sim 6''$) and add a 50% flux uncertainty. We further obtained a K-band image of the host galaxy using the Large Binocular Telescope (PI: Prandoni, Program ID 66; Saxena et al. in prep), and find it to have a magnitude of $K = 20.02$ AB. We then use these flux densities to fit an SED using EAZY and Brown et al. (2014) templates and derive a photometric redshift of $z = 1.8 \pm 0.5$. The best-fit SED is shown in Figure 3.11.

If the photo-z estimate is correct, this would make USS422 one of the highest-z giant radio galaxies currently known, with a total extent of ~ 875 kpc. To achieve such a linear size, the galaxy must harbour an extremely massive black hole and/or have had an AGN accreting close to the Eddington limit for a long time, i.e. $> 10^7$ yr (see for example Saxena et al. 2017). Follow-up spectroscopy is essential to truly confirm the redshift of the host galaxy.

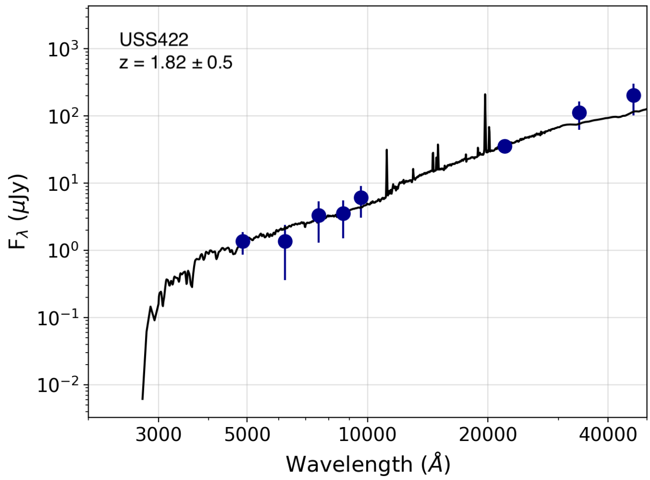

Figure 3.11: Best-fit SED for the candidate giant radio galaxy USS422 (observed frame) with a photometric redshift of $z = 1.82 \pm 0.5$. The photometry used to fit the SED was obtained from PS1 g, r, i, z, y bands, K-band from the Large Binocular Telescope and WISE $W1$ and $W2$ bands. Spectroscopic confirmation of the photo-z would make USS422 one of the highest-z giant radio galaxies currently known.

3.5 Discussion

Compact ultra-steep spectrum radio sources have been found to be excellent tracers for high-redshift radio galaxies. However, HzRGs are not the only sources that have an ultra-steep spectrum. Although our selection has been designed to maximise the chances of detecting high redshift radio galaxies, here we discuss some other classes of objects that could be present in our sample.

3.5.1 Radio pulsars

Radio emission generated in pulsar magnetospheres has been shown to have a spectral index ranging from -0.7 to -3.3 with a median spectral index of -1.6 (Sieber 1973). Radio pulsars are also extremely compact (angular size $<< 1''$). As all known pulsars are galactic sources, the majority lies in or near the galactic plane (Manchester et al. 2005). Since in our analysis we exclude the galactic plane, there is a reduced chance of contamination by radio pulsars. Frail et al. (2016) searched for emission at 150 MHz from TGSS ADR towards all currently known and well-localised radio pulsars covered in the survey. We find that no radio source in our final sample lies within $10''$ of the Frail et al. (2016) pulsar catalog. Addition-

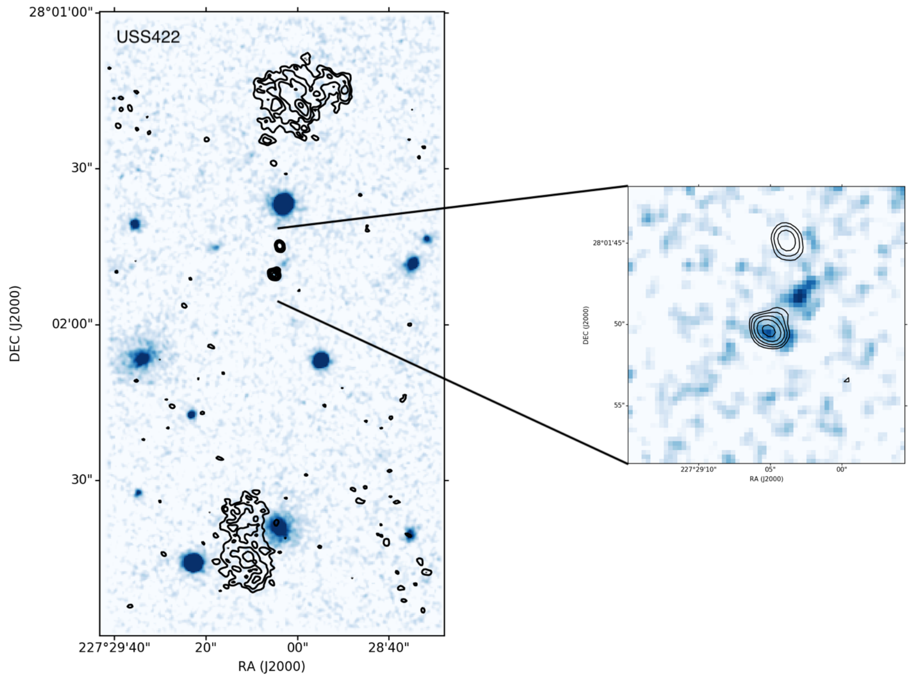

Figure 3.12: VLA 1.4 GHz contours of the giant radio galaxy (GRG) candidate USS422 overlaid on PanSTARRS1 z-band image. The southern lobe (A) has an ultra-steep spectrum when compared with FIRST ($\alpha^{\rm TGSS}_{\rm FIRST} = -1.62$), where the source is likely resolved out. The contours begin at $60\,\mu$Jy, which is roughly equivalent to 2σ and are a geometric progression of $\sqrt{2}$. The largest angular size of the radio galaxy is measured to be $1.7'$. There is no clear optical counterpart in the z-band image, however faint emission in the optical image is visible corresponding to the component 'B' that could potentially be the host galaxy (inset). With a best-fit photometric redshift of 1.8 ± 0.5 (Figure 3.11), the total extent of this radio galaxy is 875 kpc.

ally, pulse-averaged emission from radio pulsars is known to be highly variable in continuum surveys due to interstellar scattering, with changes in peak flux density varying by as much as $> 50\%$ (Brook et al. 2016). Since we suppress the presence of highly variable sources in our sample by ensuring comparable flux densities in both FIRST and NVSS at 1.4 GHz, which were taken at different epochs, and the fact that we record consistent flux density measurements from the two VLA observations that were carried out 30 days apart for each target, we further minimise the presence of pulsars in our sample.

3.5.2 Dust obscured radio galaxies

A class of objects that could have strong radio luminosities but be extremely faint at optical and infrared wavelengths are highly obscured radio AGN. These could be similar to hot dust obscured galaxies (DOGs; Wu et al. 2012) that host a radio AGN. Such galaxies are hard to detect even at 3.6 and 4.5 microns (with WISE $W1$ and $W2$) and show significantly higher submillimeter ratios than normal galaxies, thereby suggesting the presence of very hot dust. Dedicated follow-up observations at submillimeter wavelengths are necessary to identify such objects in our sample.

3.5.3 Diffuse sources: radio halos and fading radio galaxies

Radio halos are diffuse radio sources that are generally found in the centres of clusters and are not identified with any particular host galaxy. They are known to have ultra-steep spectral indices, moderate radio luminosities and large projected sizes (Röttgering et al. 1994). The last property is taken care of in our sample as we ensure true compactness of a USS source and this should in principle exclude the presence of radio halos in our sample.

The lobes of fading radio galaxies also appear to be diffuse, with their spectral index steepened due to extreme radiation and expansion losses. Due to their steep spectral indices, USS searches are often used to select fading radio sources (see for example Parma et al. 2007). We note that USS422 (Figure 3.12) in our sample may be an example of a fading radio source discovered using USS selection. Follow-up observations at various wavelengths are essential to truly determine the nature of this galaxy.

To separate out radio galaxies at the highest redshifts from the plethora of ultra-steep spectrum radio sources that could be present in our sample, we again stress upon the importance of follow-up spectroscopy and deep imaging.

3.6 Summary

Here we summarise the methods, analysis and findings of this paper.

1. We have defined a sample of ultra-steep spectrum (USS) radio sources from the TGSS ADR1 at 150 MHz to search for high-redshift radio galaxies (HzRGs). We have used the TGSS ADR1 along with FIRST and NVSS at 1.4 GHz to select sources with spectral indices steeper than -1.3 ($\alpha_{1400}^{150} < -1.3$). We have employed strict size restrictions: deconvolved major axis $< 28''$ in TGSS ADR1 and $< 10''$ in FIRST to select compact sources and maximise chances of detecting radio sources at high-z. We have ensured that none of the USS radio sources have detections in available all-sky optical (SDSS, Pan-STARRS1) and infrared (ALLWISE) surveys to eliminate low-redshift interlopers. Next, we apply flux density limits that ensure that we probe a completely new parameter space by excluding sources that could have been detected in previous searches for USS sources. This leaves us with sources with flux densities $50 < S_{150} < 200$ mJy. The final sample resulting from these selection criteria consists of 32 sources.

2. We have followed up 31 of these sources with the VLA in A-configuration at 1.4 GHz (L-band) and 14 sources at 370 MHz (P-band). From our L-band observations with an average beam size of $1.3''$, we note that 15 out of 32 sources have a single radio component. The angular sizes of a large majority of sources $< 16''$, in line with predictions and expectations of radio sizes at high redshifts, increasing the likelihood of our sample probing HzRGs. P-band (370 MHz) imaging of 17 of these sources revealed ten of them to show signs of flattening of the radio SED at frequencies between 150 and 370 MHz, which is expected from compact HzRGs.

3. We then analyse stacked photometry in optical and infrared bands of all sources in the sample. Although stacking analysis is most effective for sources that have similar properties, we do this anyway to gain insights into the median properties of our sample. We stack the optical and infrared (non-)detections from SDSS, Pan-STARRS1 and WISE centred on expected positions of the host galaxy and fit an SED to derive a median photometric redshift of 2.93 for the sample with 1σ limits ranging from $z = 1.3 - 4.75$. Fits with $z > 6$ are within 3σ.

4. Two sources in our sample lie in well-studied extragalactic fields that have deeper multiwavelength data available. One of these sources lies in the Lockman Hole field. With the availability of LOFAR LBA data at 60 MHz,

we note the spectral turnover in the radio SED between 60 and 150 MHz, which has also been reported before in the literature. Additionally, the radio source has counterparts in J and K bands in the UKIDSS Deep Extragalactic Survey (DXS) and in Spitzer IRAC 3.6 and 4.5 micron bands from the SWIRE survey. Using these, we derive the best-fit photometric redshift to be $z = 4.8 \pm 2.0$, although lower-z solutions are not formally excluded. Another source lies in the ELAIS-N1 field, with optical and infrared counterparts identified from the deep HSC-SSP optical data and J and K bands from the DXS. We derive the photo-z for this source to be $z = 1.4 \pm 0.1$.

5. In addition to the HzRG candidates, we observed a USS source that was not a candidate HzRG but showed signs of potential large scale diffuse emission. The wide-field VLA image revealed this source to be a candidate giant radio galaxy with a total extent of 1.7 arcmin. We derived the photo-z of the associated host galaxy to be $z = 1.8 \pm 0.5$. If the redshift is accurate, the total extent of this radio galaxy would be ~ 875 kpc, making it one of the largest known giant radio galaxies at these redshifts.

6. Lastly, we discuss some other classes of objects that could be present in our sample. We note that chances of radio pulsars contaminating our sample are minimal, as our sample does not cover the sky area of the galactic plane and we also take measures to rule out variable sources. However, there is a possibility of the presence of dust obscured radio AGN at lower redshifts, fading radio galaxies and also bent, head-tail radio galaxies at lower redshifts to be present in our sample. Follow-up observations are essential to separate our the various classes of objects present in our sample.

The current highest redshift radio galaxy is at $z = 5.12$ with an ultra-steep spectral index of $\alpha = -1.6$ (van Breugel et al. 1999). With new and improved radio surveys coming online, there is potential to push the highest known redshift for a radio galaxy to $z > 6$. Radio galaxies at $z > 6$ can be indispensable probes of the epoch of reionisation and studying even a single radio galaxy at $z > 6$ could have tremendous implications on cosmology. We have attempted to extend the USS search technique at fainter flux densities to be potentially employed as a robust tool to search for HzRGs at the highest redshifts. We have now started an extensive follow-up campaign to spectroscopically determine the redshifts of our HzRG candidates and also study the underlying stellar populations in the host galaxies.

Acknowledgments

We thank the referee for useful comments and suggestions that helped improve this paper. AS and HJR gratefully acknowledge support from the European Research Council under the European Unions Seventh Framework Programme (FP/2007-2013)/ERC Advanced Grant NEWCLUSTERS-321271. PNB is grateful for support from STFC via grant ST/M001229/1. This paper uses observational material taken with the Very Large Array, a National Radio Astronomy Observatory (NRAO) instrument. The NRAO is a facility of the National Science Foundation operated under cooperative agreement by Associated Universities, Inc. This paper uses data from the Giant Metrewave Radio Telescope (GMRT). We thank the staff of the GMRT that made these observations possible. GMRT is run by the National Centre for Radio Astrophysics of the Tata Institute of Fundamental Research.

This work has made extensive use of IPython (Pérez & Granger 2007). This research made use of Astropy, a community-developed core Python package for Astronomy (Astropy Collaboration et al. 2013). This research made use of APLpy, an open-source plotting package for Python (Robitaille & Bressert 2012) and matplotlib (Hunter 2007b) for generating figures and plots. The data analysis and visualisation were done using topcat (Taylor 2005). This work would not have been possible without the countless hours put in by members of the open-source developing community all around the world.

3.A Source catalog

Here we report the measured flux densities and angular sizes of all sources imaged with the VLA, with an average beam size of $1.3''$.

Table 3.5: Flux densities and angular sizes from VLA L-band observations of 32 HzRG candidates with a detection threshold of at least 5σ. The sources are listed in order of Right Ascension. All source names in the column Catalogue ID have 'TGSSADR' as prefix. The column LAS stands for largest angular size. The source USS255 was not observed with the VLA, but we include it here nonetheless to present out complete sample. We also present the source ID from VLA FIRST and the reported flux density in the FIRST source catalogue. The average error in the reported flux density from FIRST is roughly $5-10\%$.

Catalogue ID	Name	Component	RA (J2000)	DEC (J2000)	$S_{1.4}$ (mJy)	$S_{1.4}^{tot}$ (mJy)	S_{150} (mJy)	$\alpha_{1.4}^{150}$	LAS ($''$)	FIRST ID	S_{FIRST}^{tot} (mJy)
J004828.6+115143	USS255		00:48:28.6	+11:51:43.9	3.8 ± 0.2	–	84 ± 16	-1.4 ± 0.1	–	J004828.4+115144	3.7
J070319.0+515157	USS206	A	07:03:18.5	+51:52:01.2	4.6 ± 0.09	7.35 ± 0.1	102 ± 20	-1.6 ± 0.1	8.46	J070319.0+515155	2.6
		B	07:03:19.0	+51:51:54.0	2.75 ± 0.1						
J071622.5+370338	USS182	A	07:16:22.6	+37:03:36.0	5.02 ± 0.07	8.54 ± 0.1	146 ± 30	-1.4 ± 0.1	3.17	J071622.5+370337	6.4
		B	07:16:22.3	+37:03:39.6	3.52 ± 0.05						
J071737.9+592248	USS31	A	07:17:37.9	+59:22:44.4	3.91 ± 0.03	4.84 ± 0.03	149 ± 30	-1.7 ± 0.1	7.55	J071738.2+592245	1.4
		B	07:17:37.2	+59:22:51.6	0.93 ± 0.03						
J073036.8+481103	USS188	A	07:30:36.7	+48:11:06.0	5.67 ± 0.09	9.2 ± 0.1	166 ± 33	-1.3 ± 0.1	4.20	J073036.6+481104	8.7
		B	07:30:36.5	+48:11:02.4	3.53 ± 0.02						
J075751.8+611620	USS309	A	07:57:51.6	+61:16:19.2	4.61 ± 0.12	8.4 ± 0.1	83 ± 17	-1.3 ± 0.1	6.10	J075751.7+611624	2.8
		B	07:57:51.6	+61:16:26.4	3.79 ± 0.07						
J080849.9+382603	USS27		08:08:49.9	+38:26:02.4	7.63 ± 0.06		111 ± 22	-1.3 ± 0.1	2.63	J080849.9+382604	6.1
J081103.2+511443	USS36		08:11:03.1	+51:14:42.0	6.01 ± 0.1		123 ± 25	-1.4 ± 0.1	1.33	J081103.2+511442	5.4
J085746.8+175756	USS273		08:57:46.8	+17:57:57.6	7.37 ± 0.05		154 ± 31	-1.3 ± 0.1	1.37	J085746.8+175757	7.8
J095635.3+270823	USS72		09:56:35.3	+27:08:24.0	3.85 ± 0.05		52 ± 10	-1.4 ± 0.1	1.29	J095635.4+270822	3.2
J095946.1+520906	USS483	A	09:59:46.1	+52:09:07.2	2.11 ± 0.06	3.3 ± 0.1	89 ± 18	-1.5 ± 0.1	2.77	J095946.1+520907	3.1
		B	09:59:45.8	+52:09:03.6	1.19 ± 0.06						
J101813.4+111746	USS46		10:18:13.4	+11:17:45.6	4.91 ± 0.1		87 ± 17	-1.4 ± 0.1	1.62	J101813.4+111745	4.2
J105429.5+583226	USS410		10:54:29.5	+58:32:27.6	3.75 ± 0.05		96 ± 19	-1.6 ± 0.1	1.29	J105429.5+583226	3.1
J110638.7+545018	USS18		11:06:38.6	+54:50:20.4	5.72 ± 0.1		131 ± 26	-1.4 ± 0.1	1.73	J110638.8+545020	5.4
J111054.9+610200	USS172	A	11:10:55.4	+61:02:02.4	3.77 ± 0.06	7.1 ± 0.1	124 ± 25	-1.4 ± 0.1	9.67	J111055.4+610202	3.2
		B	11:10:54.2	+61:01:58.8	3.31 ± 0.04						
J113517.5+465906	USS159		11:35:17.5	+46:59:06.0	8.01 ± 0.05		149 ± 30	-1.4 ± 0.1	1.22	J113517.6+465905	6.9
J114006.3+464451	USS253	A	11:40:06.2	+46:44:49.2	6.36 ± 0.1	8.13 ± 0.1	156 ± 31	-1.5 ± 0.1	10.0	J114006.2+464449	5.9
		B	11:40:06.7	+46:44:52.8	0.87 ± 0.07						
		C	11:40:06.7	+46:44:56.4	0.90 ± 0.07						

Table 3.4: Continued.

Catalogue ID	Name	Component	RA (J2000)	DEC (J2000)	$S_{1.4}$ (mJy)	$S^{tot}_{1.4}$ (mJy)	S_{150} (mJy)	$\alpha^{150}_{1.4}$	LAS ($''$)	FIRST ID	S^{tot}_{FIRST} (mJy)
J122043.6+611906	USS312		12:20:43.9	+61:19:04.8	2.52 ± 0.05		79 ± 16	-1.4 ± 0.1	1.26	J122043.9+611907	3.4
J124158.9+204009	USS439	A	12:41:59.0	+20:40:08.4	6.82 ± 0.06	7.95 ± 0.1	136 ± 27	-1.3 ± 0.1	7.76	J124158.9+204009	7.3
		B	12:41:58.8	+20:40:08.4	0.30 ± 0.04						
		C	12:41:58.6	+20:40:12.0	0.32 ± 0.04						
		D	12:41:58.6	+20:40:12.0	0.51 ± 0.04						
J131206.0+452257	USS268		13:12:06.0	+45:22:55.2	4.62 ± 0.05		92 ± 18	-1.4 ± 0.1	2.02	J131206.0+452257	3.9
J132801.4+202858	USS67	A	13:28:01.2	+20:28:51.6	2.88 ± 0.05	5.1 ± 0.1	59 ± 12	-1.3 ± 0.1	9.40	J132801.6+202901	1.9
		B	13:28:01.7	+20:28:58.8	2.20 ± 0.05						
J133911.8+203348	USS32		13:39:11.8	+20:33:50.4	3.99 ± 0.07		76 ± 15	-1.4 ± 0.1	2.09	J133911.7+203349	3.9
J135045.7+221716	USS415	A	13:50:45.4	+22:17:16.8	3.86 ± 0.1	6.62 ± 0.1	188 ± 38	-1.7 ± 0.1	8.12	J135045.8+221713	2.1
		B	13:50:45.8	+22:17:13.2	2.76 ± 0.05						
J145154.4+400656	USS320	A	14:51:54.5	+40:06:57.6	2.15 ± 0.03	3.03 ± 0.1	86 ± 17	-1.7 ± 0.1	2.70	J145154.5+400656	2.7
		B	14:51:54.2	+40:06:54.0	0.88 ± 0.03						
J153049.9+104933	USS202		15:30:49.9	+10:49:30.0	7.50 ± 0.07		170 ± 34	-1.4 ± 0.1	1.69	J153049.8+104931	7.3
J153813.3+134153	USS43		15:38:13.4	+13:41:52.8	12.5 ± 0.25		200 ± 40	-1.4 ± 0.1	1.47	J153813.4+134153	9.6
J160819.1+123951	USS51	A	16:08:19.2	+12:39:50.4	6.52 ± 0.04	7.88 ± 0.1	59 ± 12	-1.3 ± 0.1	5.69	J160819.1+123950	3.2
		B	16:08:19.2	+12:39:54.0	1.36 ± 0.02						
J161026.5+103924	USS450	A	16:10:26.6	+10:39:21.6	6.55 ± 0.07	9.65 ± 0.2	131 ± 26	-1.4 ± 0.1	15.78	J161026.1+103937	3.0
		B	16:10:26.2	+10:39:36.0	3.10 ± 0.05						
J161538.9+532726	USS7	A	16:15:38.9	+53:27:25.2	2.80 ± 0.04	6.33 ± 0.1	122 ± 24	-1.5 ± 0.1	3.72	J161539.1+532727	4.3
		B	16:15:39.1	+53:27:28.8	3.53 ± 0.03						
J161907.9+631250	USS404		16:19:08.2	+63:12:46.8	9.09 ± 0.09		153 ± 31	-1.4 ± 0.1	2.12	J161908.3+631248	7.7
J162521.8+254647	USS337		16:25:21.8	+25:46:48.0	11.14 ± 0.33		171 ± 34	-1.3 ± 0.1	1.66	J162521.8+254648	8.8
J163643.1+195830	USS98	A	16:35:43.2	+19:58:30.0	1.47 ± 0.20	3.8 ± 0.3	178 ± 36	-1.5 ± 0.1	7.24	J163543.2+195833	2.0
		B	16:35:43.0	+19:58:22.8	2.33 ± 0.22						

3.B VLA L-band images and contour maps

Here we show VLA L-band (1.4 GHz) A-configuration images in greyscale, with contours overlaid for all 31 HzRG candidates that were observed. The average beam size is $\sim 1.3''$ and the noise in the images varies from 50 to 70 µJy. The contours begin at 250 µJy, which translates to roughly $3.5 - 5\sigma$. The images are presented in order of source Right Ascension.

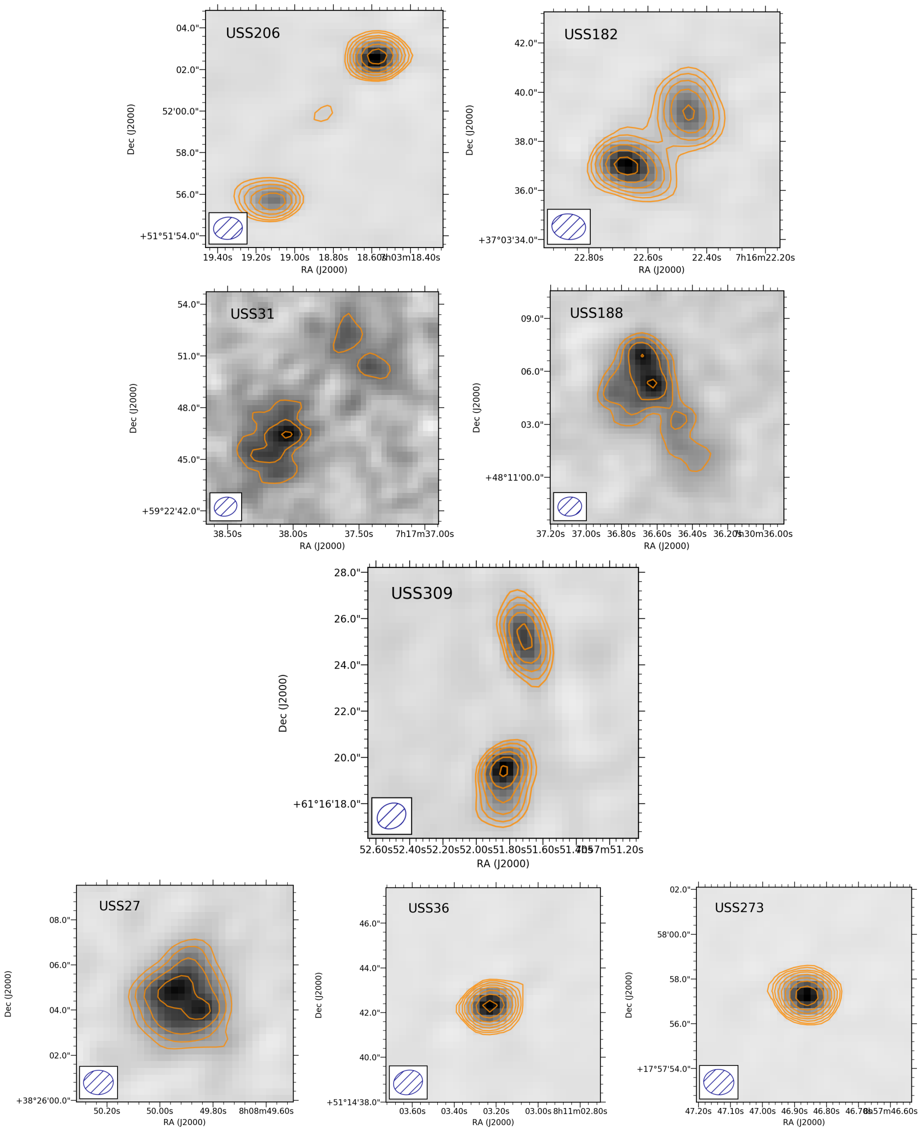

Figure 3.13: VLA L-band images and contours for 31 sources observed. The contours shown begin at 0.25 mJy, which is on average $3.5 - 5\sigma$ and are a geometric progression of $\sqrt{2}$, such that the flux density increases by a factor of 2 for every 2 contours. The beam used to image each source is shown in the bottom-left.

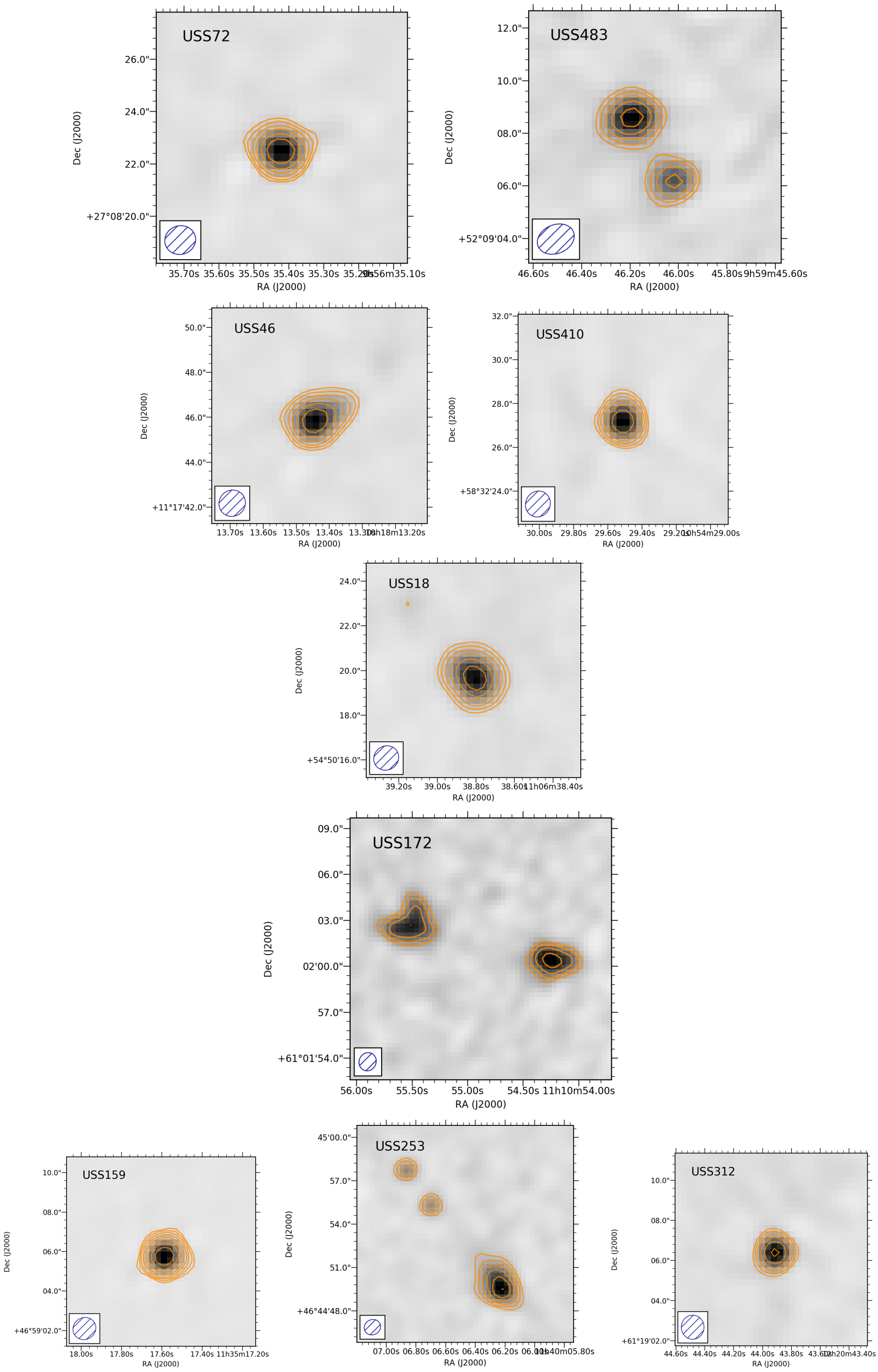
USS72
USS483
USS46
USS410
USS18
USS172
USS159
USS253
USS312

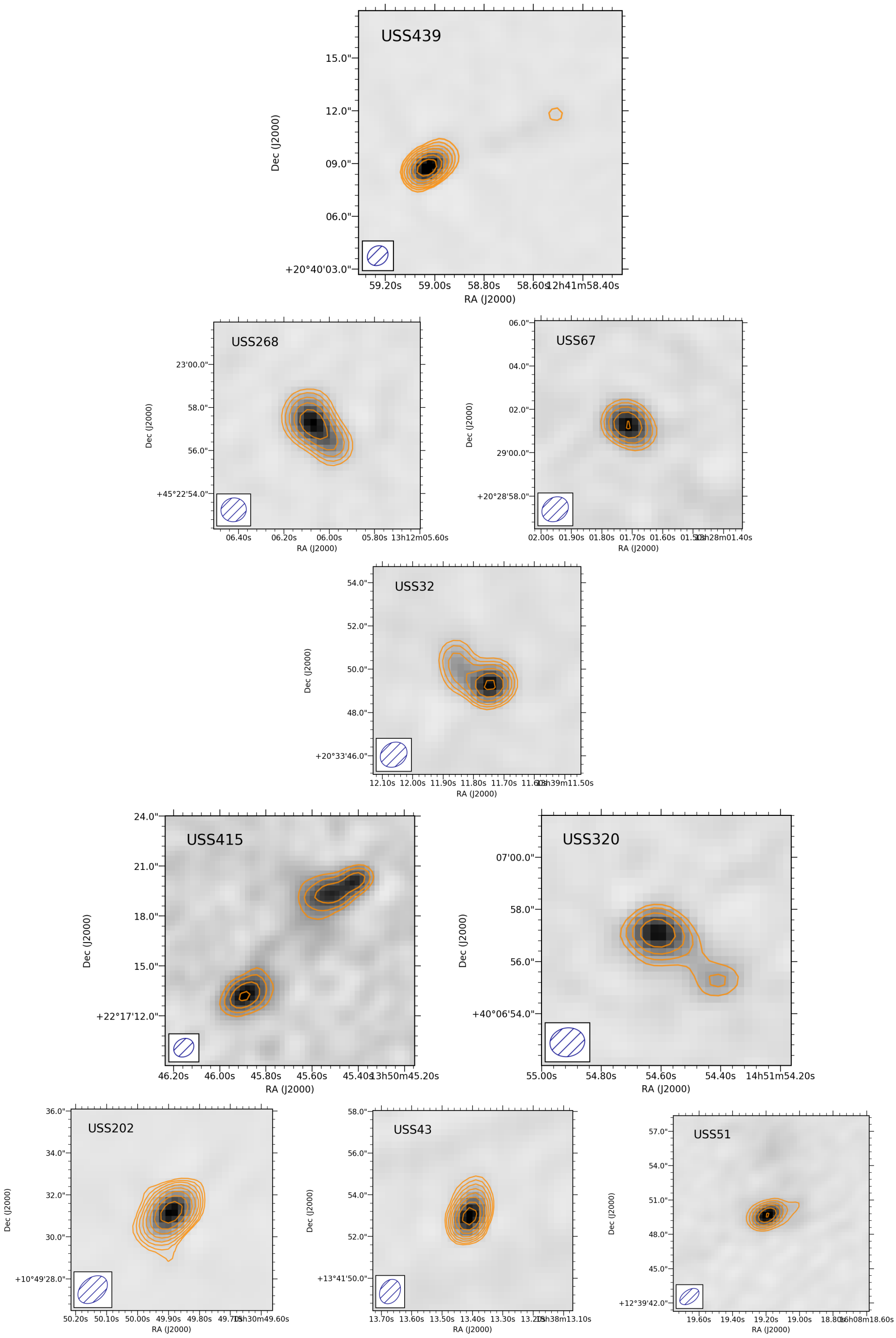
USS439
USS268
USS67
USS32
USS415
USS320
USS202
USS43
USS51
RA (J2000)
Dec (J2000)

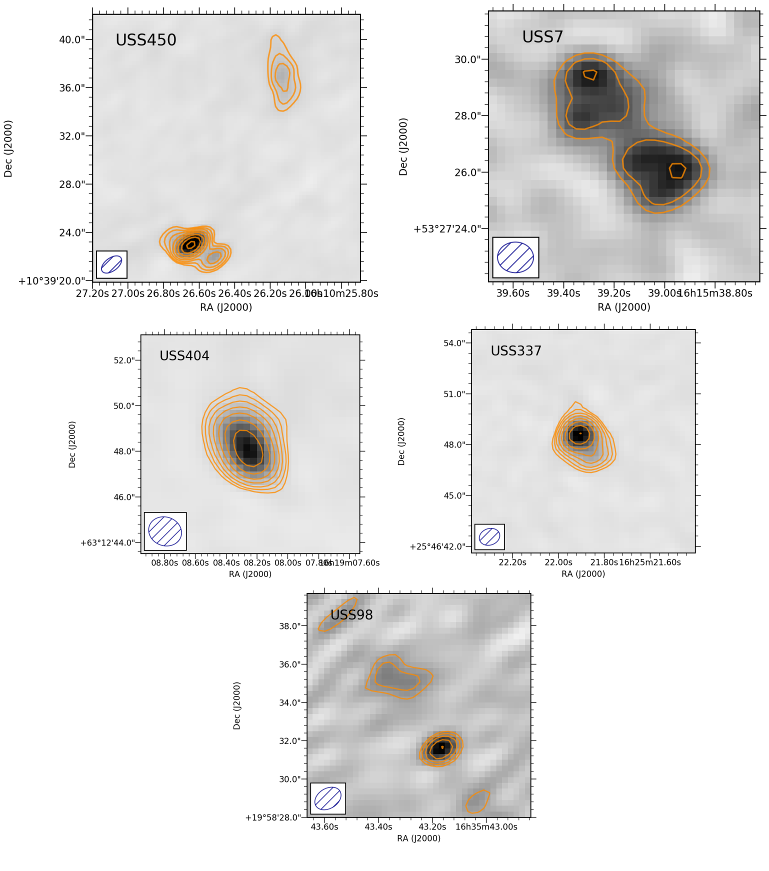
USS450
Dec (J2000)
RA (J2000)
USS7
Dec (J2000)
RA (J2000)
USS404
Dec (J2000)
RA (J2000)
USS337
Dec (J2000)
RA (J2000)
USS98
Dec (J2000)
RA (J2000)

4 | Discovery of a radio galaxy at z = 5.72

We report the discovery of the most distant radio galaxy to date, TGSS J1530+1049 at a redshift of $z = 5.72$, close to the presumed end of the Epoch of Reionisation. The radio galaxy was selected from the TGSS ADR1 survey at 150 MHz for having an ultra-steep spectral index, $\alpha_{1.4\,\mathrm{GHz}}^{150\,\mathrm{MHz}} = -1.4$ and a compact morphology obtained using VLA imaging at 1.4 GHz. No optical or infrared counterparts for the radio source were found in publicly available sky surveys. Follow-up optical spectroscopy at the radio position using GMOS on Gemini North revealed the presence of a single emission line. We identify this line as Lyman alpha at $z = 5.72$, because of its asymmetric line profile, the absence of other optical/UV lines in the spectrum and a high equivalent width. With a Lyα luminosity of 5.7×10^{42} erg s^{-1} and a FWHM of 370 km s^{-1}, TGSS J1530+1049 is comparable to 'non-radio' Lyman alpha emitters (LAEs) at a similar redshift. However, with a radio luminosity of log $L_{150\,\mathrm{MHz}} = 29.1$ W Hz^{-1} and a deconvolved physical size 3.5 kpc, its radio properties are similar to other known radio galaxies at $z > 4$. Subsequent J and K band imaging using LUCI on the Large Binocular Telescope resulted in non-detection of the host galaxy down to 3σ limits of $J > 24.4$ and $K > 22.4$ (Vega). The K band limit is consistent with $z > 5$ from the $K - z$ relation for radio galaxies and helps rule out low redshifts. The stellar mass limit derived using simple stellar population models is $M_{\mathrm{stars}} < 10^{10.5}\ M_{\odot}$. Its relatively low stellar mass and small radio and Lyα sizes suggest that TGSS J1530+1049 may be a radio galaxy in an early phase of its evolution.

Based on:
Saxena A., Marinello M., Overzier R.A., Best P.N., Röttgering H.J.A.,
Duncan K.J., Prandoni I., Pentericci L., Magliocchetti M., Paris D.,
Cusano F., Marchi F., Intema H.T. and Miley G.K.
MNRAS, 480, 2733

4.1 Introduction

High-redshift radio galaxies (HzRGs) are thought to be the progenitors of local massive elliptical galaxies and generally contain large amounts of dust and gas (Best et al. 1998b; Carilli et al. 2002a; Reuland et al. 2004; De Breuck et al. 2010). They are also among the most massive galaxies at their redshift (Overzier et al. 2009) and are often found to be located at the centre of clusters and proto-clusters of galaxies (Pentericci et al. 2000; Venemans et al. 2002; Röttgering et al. 2003; Miley et al. 2004; Hatch et al. 2011; Orsi et al. 2016). Studies of their environment can give insights into the assembly and evolution of the large scale structure in the Universe. Miley & De Breuck (2008) provide an extensive review about the properties of distant radio galaxies and their environments.

Radio galaxies at $z > 6$, in the Epoch of Reionisation (EoR), are of particular interest as they could be used as unique tools to study the process of reionisation in detail. At these redshifts, the hyper-fine transition line from neutral hydrogen atoms, with a rest-frame wavelength of 21 cm, falls in the low-frequency radio regime and can be observed as absorption signals in spectra of luminous background radio sources such as radio galaxies (Carilli et al. 2002b; Furlanetto & Loeb 2002; Xu et al. 2009; Mack & Wyithe 2012; Ewall-Wice et al. 2014; Ciardi et al. 2015). Such 21 cm absorption signals from patches of neutral hydrogen clouds in the early Universe could in principle be observed by current and next-generation radio telescopes such as the Giant Metre-wave Radio Telescope (GMRT; Swarup et al. 1991), the Low Frequency Array (LOFAR; van Haarlem et al. 2013), the Murchinson Widefield Array (MWA; Tingay et al. 2013b) and the Square Kilometer Array (SKA; Dewdney et al. 2009). This unique application motivates searches for bright enough radio galaxies at the highest redshifts from deep all-sky surveys at low radio frequencies.

Finding powerful radio galaxies at increasingly large distances or redshifts, however, is challenging. HzRGs are rare and flux-limited samples have shown that their space densities fall off dramatically at $z > 2 - 3$ (Dunlop & Peacock 1990; Willott et al. 2001; Rigby et al. 2011, 2015). Although a number of quasars at $z > 5$ are known, with a few also being radio-loud (see Bañados et al. 2015, for example), the same cannot be said for radio galaxies - previously, the only known radio galaxy at $z > 5$ was TN J0924−2201 at $z = 5.19$ (van Breugel et al. 1999). If the orientation-based unification of radio galaxies and quasars is valid (see Morabito et al. 2017, for example), the number of radio quasars and galaxies at any given epoch should be comparable and it may be possible that many of the already unidentified radio sources are at $z > 5$. The scarcity of $z > 5$ radio galaxies could therefore be due to the relative difficulty in first identifying these sources amongst the wider radio source population, and then obtaining spectroscopic redshifts for these radio galaxies, which are optically much fainter than quasars. Dedicated spectroscopic follow-up of radio sources such as the WEAVE-LOFAR survey (Smith et al. 2016), and the upcoming major optical facilities such as the Extremely Large Telescope (ELT), the Thirty Meter Telescope (TMT), the Giant Magellan Telescope (GMT) and the James Webb Space Telescope (JWST) will help overcome these difficulties and potentially help characterise a number of USS radio sources.

The key requirement for gathering enough statistics for studies of radio galaxies at high redshifts are deep low-frequency radio surveys covering large areas on the sky. Surveys such as the TIFR GMRT Sky Survey Alternative Data Release 1 (TGSS; Intema et al. 2017) and the currently ongoing surveys using LOFAR (Shimwell et al. 2017) are opening up new parameter spaces for searches for radio galaxies at $z \geqslant 6$. Using TGSS, which covers the entire radio sky north of -53 declination at a frequency of 150 MHz and achieving a median noise level of 3.5 mJy beam^{-1}, we launched a campaign to hunt for fainter and potentially more distant HzRGs, with the ultimate aim of discovering radio galaxies that could be suitable probes of the EoR (Saxena et al. 2018b). In this paper, we report the discovery of a radio galaxy at a redshift of $z = 5.72$, TGSS J1530+1049, which was pre-selected as part of our sample of high-redshift radio galaxy candidates.

The layout of this paper is as follows. In Section 4.2 we present details about the initial source selection criteria and follow-up radio observations at high resolution for TGSS J1530+1049. In Section 5.2.2 we present the new optical spectroscopy and infrared imaging obtained for TGSS J1530+1049 and expand upon the data reduction methods. In Section 4.4 we describe how the redshift for this source was determined. In Section 5.4 we study the emission line and radio properties of this source and set constraints on its stellar mass. We also compare the observed properties to galaxies at the same epoch from the literature. Finally, in Section 4.6 we summarise the findings of this paper. Throughout this paper we assume a flat ΛCDM cosmology with H_0 = 70 km s^{-1} Mpc^{-1} and $\Omega_m = 0.3$. Using this cosmology, at a redshift of 5.72 the age of the Universe is 0.97 Gyr, and the angular scale per arcsecond is 5.86 kpc.

4.2 Source selection

Our two stage selection process is based on first isolating compact radio sources with an ultra-steep spectrum (USS; $\alpha < -1.3$, where $S_\nu \propto \nu^\alpha$) at radio wavelengths, that has historically been very successful at finding HzRGs from wide area radio surveys (Röttgering et al. 1994; Blundell et al. 1999; De Breuck et al. 2000a;

Afonso et al. 2011), and then combining it with optical and/or infrared faintness requirements. The relation that exists between the apparent K-band magnitude of radio galaxies and their redshift, known as the $K - z$ relation, (Lilly & Longair 1984; Jarvis et al. 2001b; Willott et al. 2003; Rocca-Volmerange et al. 2004) gives further strength to the argument of selecting USS sources that are also faint at near-infrared wavelengths in a bid to isolate HzRGs (Ker et al. 2012). Deep near-infrared imaging of promising USS candidates can therefore serve as an independent way to set constraints on the redshifts of radio sources. HzRGs are expected to be very young and therefore, have small sizes at the highest redshifts (Saxena et al. 2017): implementing an additional criterion that puts an upper limit on the angular sizes of radio sources has the potential to increase the efficiency of pin pointing the highest-redshift sources in a wide area radio survey.

Combining all of these selection methods, we first shortlisted 588 candidates with an ultra-steep spectrum ($\alpha_{1.4\,\mathrm{GHz}}^{150\,\mathrm{MHz}} < -1.3$) and compact morphologies, out of a total of 65,996 sources that had spectral index information from TGSS and FIRST/NVSS. This sample probes fainter flux densities than previous large area searches and has flux limits that ensure that a new parameter space in flux density and spectral index is probed, where a large number of undiscovered HzRGs are expected to lie (Ishwara-Chandra et al. 2010). From this shortlist, we then retained in our sample only those radio sources that are blank in all available optical surveys such as the Sloan Digital Sky Survey DR12 (SDSS; Alam et al. 2015b) and the Pan-STARRS1 survey (PS1; Chambers et al. 2016b), and infrared surveys such as ALLWISE using the *WISE* satellite (Wright et al. 2010b) and the UKIDSS surveys (Lawrence et al. 2007b) to maximise the chances of finding radio galaxies at the highest redshifts. This led to a final sample of 32 very promising HzRG candidates. Details of the sample selection can be found in Saxena et al. (2018b).

High resolution imaging using the Karl G. Jansky Very Large Array (VLA) for the 32 candidates, including for TGSS J1530+1049 (Right Ascension: 15:30:49.9, Declination: +10:49:31.1) is presented in Saxena et al. (2018b), which was used to obtain morphologies and sub-arcsecond localisation of the expected positions of the host galaxies, enabling blind spectroscopic follow-up. TGSS J1530+1049 in particular showed a compact morphology, which was fitted with a single Gaussian. With a flux density of $S_{150\,\mathrm{MHz}} = 170 \pm 34$ mJy, TGSS J1530+1049 is one of the brightest sources in the sample. At 1.4 GHz, it has a flux density $S_{1.4\,\mathrm{GHz}} = 7.5 \pm 0.1$ mJy, giving a spectral index of $\alpha = -1.4 \pm 0.1$. With a relatively small (deconvolved) angular size of 0.6 ± 0.1 arcsec, TGSS J1530+1049 was deemed to be a promising HzRG candidate. We show the location of TGSS J1530+1049 in the flux density$-$spectral index parameter space in Figure 4.1.

TGSS J1530+1049 is not detected in any of the PS1 bands (g, r, i, z and y).

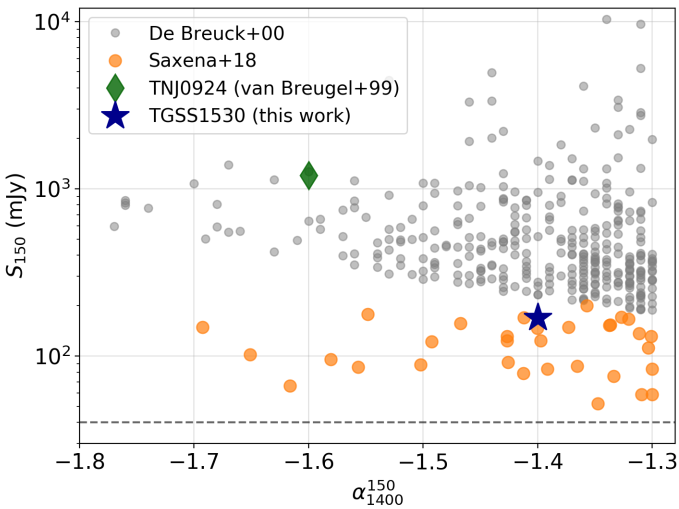

Figure 4.1: The location of TGSS J1530+1049 in the flux density−spectral index parameter space. The large orange points show the parameter space probed by the Saxena et al. (2018b) sample and the smaller grey points show radio sources from De Breuck et al. (2000a), scaled to an observed frequency of 150 MHz using the spectral indices provided for individual sources. Also shown for comparison is TN J0924−2201 at $z = 5.2$ (van Breugel et al. 1999). TGSS J1530+1049 is fainter than the previously studied large area samples and offers a new window into fainter radio galaxies at high redshifts.

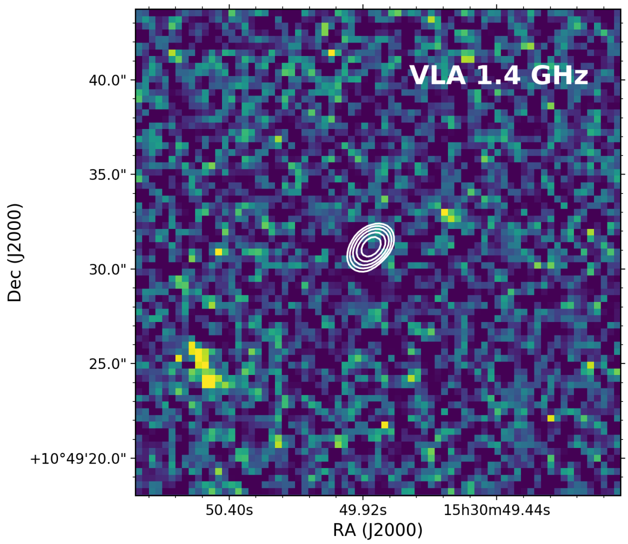

Figure 4.2: Stacked y, J, H and K band image from the UKIDSS Large Area Survey, with contours (starting from 0.5 mJy, in a geometric progression of $\sqrt{2}$) from the 1.4 GHz VLA map (Saxena et al. 2018b) overplotted for TGSS J1530+1049. The radio source is compact and has an ultra-steep spectral index. A non-detection in the UKIDSS LAS K band down to a magnitude limit of 18.4 Vega (~ 20.3 AB) made TGSS J1530+1049 a promising HzRG candidate and a prime target for spectroscopic follow-up.

This source also happens to lie in the sky area covered by the UKIDSS Large Area Survey (LAS), and is not detected down to (Vega) magnitude limits of $y > 20.5$, $J > 20.0$, $H > 18.8$ and $K > 18.4$. We show the image obtained from stacking all of the LAS bands with radio contours overlaid in Figure 4.2. Lastly, this source is also not detected in any of the ALLWISE bands. These non-detections coupled with the ultra-steep radio spectral index and compact radio morphology are in line with expectations of a high-redshift host galaxy and made TGSS J1530+1049 a prime candidate for follow-up spectroscopy.

4.3 Observations

4.3.1 Gemini GMOS spectroscopy

A long-slit spectrum of TGSS J1530+1049TGSS J1530+1049 was taken using GMOS on Gemini North on 28 April, 2017 (Program ID: GN-2017A- Q-8; PI:

Overzier) using the filter GG455_G0305 and the R400_G5305 grating giving a wavelength coverage of $5400 - 10800$ Å and a resolution of roughly $R \sim 1500$. The central wavelength was set to 7000 Å. The total length of the slit was 300 arcseconds and the slit width was chosen to be 1.5 arcseconds so that it covers the entire radio emission footprint detected in the VLA image. As the host galaxy of the radio source was undetected in all available all-sky optical/IR surveys, we performed blind offsetting from a bright star, which ensures positional accuracy to within 0.1 arcseconds, to the centroid of the radio emission. The VLA observations ensured sub-arcsecond localisation of the expected position of the host galaxy and the relatively large slit-width provided insurance against minor positional uncertainties. We took 3 exposures of 800 seconds each, giving a total of 2400 seconds of on-source exposure time. The standard star EG131 was observed for flux calibration.

We used the Gemini IRAF package for reducing the data, which includes the standard steps for optical spectrum reduction. Briefly, the bias frames were mean stacked in a master bias which was subtracted from all other images acquired. Pixel-to-pixel sensitivity was corrected through the flat field image taken during the day of the observations. The wavelength solution was derived from the arc lamp frame taken immediately after the science observations, and applied to the science frame and standard star. The 2D images were then combined in a single frame, rejecting possible cosmic rays. The sky lines were removed and flux calibration was achieved using the standard star spectrum.

A single emission line with a peak at 8170 Å and a spatial extent of ~ 1 arcsecond was detected in the reduced 2D spectrum at the expected position of the radio galaxy. No other line associated with this source was detected. No continuum was detected either bluewards or redwards of this line either. To ensure that the line detection is indeed real and not due to an artefact or contamination by cosmic rays, we looked at the individual frames, both raw and sky subtracted, to ensure that the detection (although marginal) was present in each science frame. The three frames are shown in Figure 4.3. The top panels show the raw frames and the bottom panels the sky subtracted frames. The emission line is clearly present in all three frames, ensuring that the detection is real. The extracted 1D spectrum with a 1 arcsecond aperture showing the detected emission line is shown in Figure 4.4. We give details about line identification in Section 4.4.

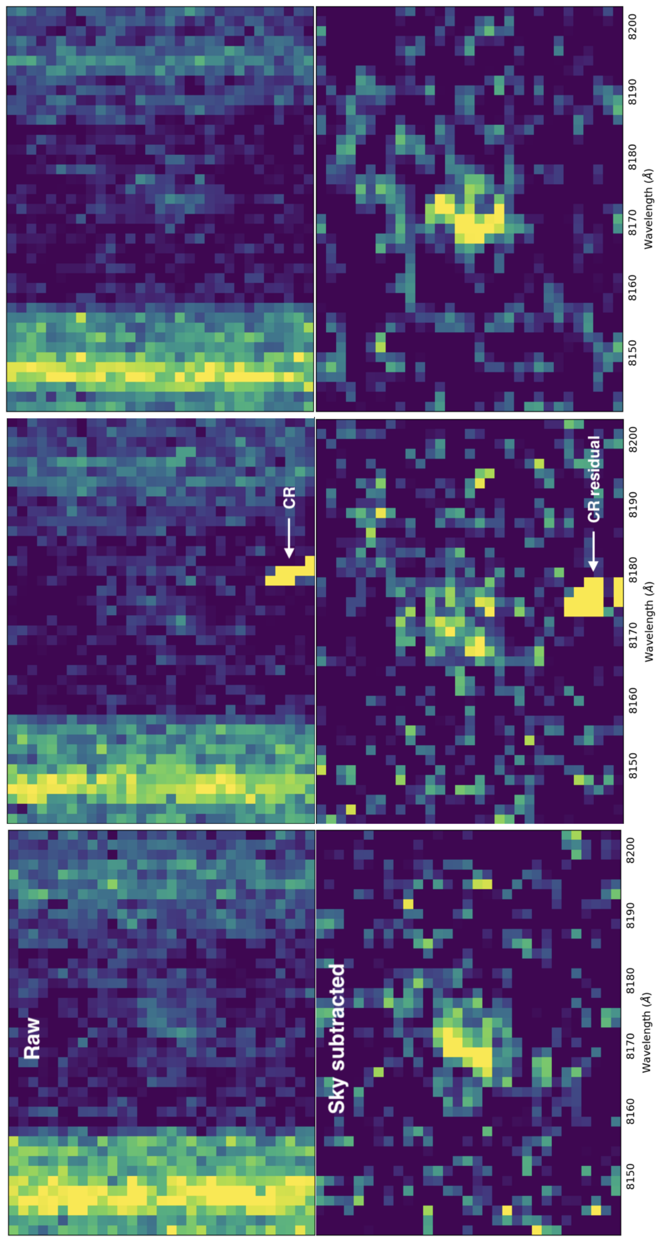

Figure 4.3: Raw (top panels) and sky subtracted (bottom panels) 2D frames shown for the three individual exposures taken using GMOS on Gemini. Traces of the emission line are visible in all three frames, ensuring that the detected line is real and not a consequence of cosmic rays or artefacts. There is some cosmic ray residual left over in the second frame but that does not contaminate the emission line signal.

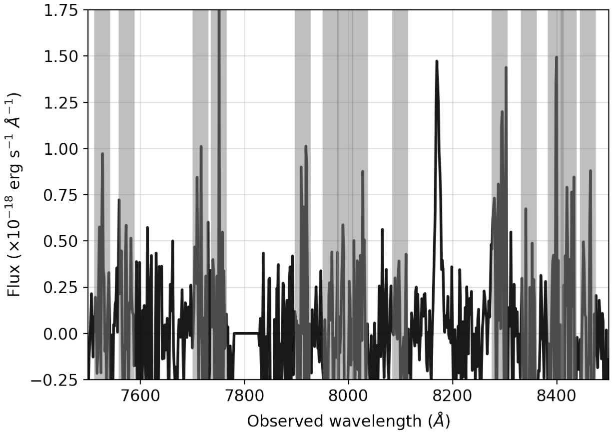

Figure 4.4: Extracted 1D spectrum showing the single emission line detection centred at 8170 Å from the GMOS 2D spectrum. No other line or continuum is detected. Shaded regions mark the presence of sky lines in the spectrum.

4.3.2 Large Binocular Telescope NIR imaging

Imaging in the J and Ks bands using LUCI (formerly known as LUCIFER; Seifert et al. 2003) on the Large Binocular Telescope (LBT) was carried out in two separate runs, with the first on 1 February 2018 and the second on 11 May 2018 (Program ID 2017_2018_43; PI: Prandoni). The average seeing throughout the observations was $0.6 - 0.8$ arcseconds. In the first run, the on-source exposure time was 720 (12×60s) seconds in J (central wavelength of 1.247 microns) and 1200 (20×60s) seconds in Ks (central wavelength of 2.194 microns). In the second run we obtained additional 3600 (30×120s) seconds in J and 3000 (50×60s) seconds in Ks, giving a total on-source exposure time of 4320 seconds in J band and 4200 seconds in Ks band.

The LUCI data reduction pipeline developed at INAF-OAR was used to perform the basic reduction such as dark subtraction, bad pixel masking, cosmic ray removal, flat fielding and sky subtraction. Astrometric solutions for individual frames were obtained and the single frames were then resampled and combined using a weighted co-addition to form a deeper image. The $4' \times 4'$ field-of-view of LUCI contained many bright objects detected in both 2MASS and the UKIDSS Large Area Survey, which were used to calibrate the photometry of the images in both bands.

The median and standard deviation of the background in both images was calculated by placing 5000 random apertures with a diameter of 1.5 arcseconds. We

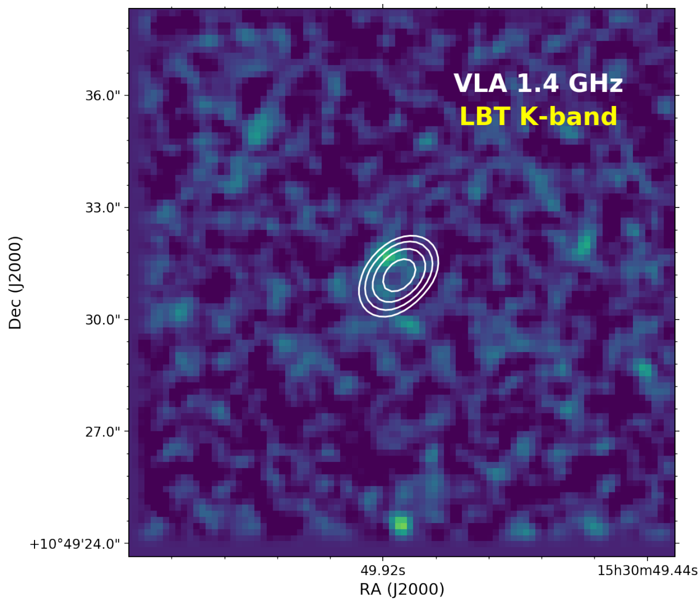

Figure 4.5: K-band image from the Large Binocular Telescope (LBT), which has been smoothed with a 3×3 pixel Gaussian kernel, with radio contours (same as Figure 2) from the VLA at 1.4 GHz overlaid. The measured magnitude at the radio position with a 1.5 arcsecond aperture is fainter than the 3σ depth of the image, giving $K > 22.4$. When the image is smoothed, however, faint emission is visible around the peak of the radio emission. The magnitude limit is consistent with $z > 5$ following the $K - z$ relation for radio galaxies. For comparison, the $z = 5.2$ radio galaxy TN J09224−2201 has a K-band magnitude of 21.3 (van Breugel et al. 1999).

measure 3σ depths of $J = 24.4$ and $Ks = 22.4$. Aperture photometry performed on both J and Ks (from here on we denote Ks as simply K) images using PHOTUTILS (Bradley et al. 2017) at the peak of the radio emission using an aperture of diameter 1.5 arcseconds yield magnitudes that are lower than the 3σ depths in both images. Smoothing the K band image with a 3×3 pixel Gaussian kernel reveals a faint source very close to the peak radio pixel, as shown in Figure 5.14, but it is not entirely clear if this indeed the host galaxy and there is no faint detection even in the smoothed J band image. A summary of the observations is given in Table 5.1.

Table 4.1: Observation log.

Telescope	Instrument	Date	Exp. time (sec)
Gemini N	GMOS long-slit	28-04-2017	2400 (3×800s)
LBT	LUCI J-band	01-02-2018	720 (12×60s)
		09-05-2018	3600 (30×120s)
	Total		4320
LBT	LUCI Ks-band	01-02-2018	1200 (20×60s)
		09-05-2018	3000 (50×60s)
	Total		4200

4.4 Redshift determination

We identify the single emission line detected in the GMOS spectrum as Lyα $\lambda1216$, giving a redshift of $z = 5.720 \pm 0.001$, which is shown in Figure 4.6. Other plausible identifications of this emission line could be [O III] $\lambda5007$, giving a redshift of $z \approx 0.63$ or Hα $\lambda6563$ at $z \approx 0.25$. These can be ruled out given the non-detection of other bright lines expected in the wavelength range covered. For example, if the observed line is [O III] at $z = 0.63$, then the [O II] $\lambda3727$ line would be observed at ~ 6075 Å, unless the galaxy has a particularly high [O III]/[O II] ratio as in the case of very low metallicity objects. An unresolved [O II] $\lambda\lambda3726, 3729$ doublet at a redshift of $z \approx 1.2$ could be a possibility, but the absence of other expected UV/optical lines common in AGN and radio galaxy spectra, such as C II] $\lambda2326$ or Mg II $\lambda\lambda2797, 2803$, which are on average a factor of $2 - 4$ times fainter than [O II] (De Breuck et al. 2001), makes this possibility unlikely. Another possibility could be C IV $\lambda1549$ giving $z = 4.27$, but this can be ruled out because in this case Lyα, which is often much brighter (for example, there are no radio galaxies in De Breuck et al. (2001) with Lyα flux lower than C IV $\lambda1549$ flux), would be expected at ~ 6410 Å and we do not see any signs of an emission line in that region, which is free from bright sky lines.

We fit a Gaussian to the emission line (shown in Figure 4.6) to measure an integrated line flux of $F_{Ly\alpha} = 1.6 \pm 0.2 \times 10^{-17}$ erg s^{-1} cm^{-2}. The total measured Lyα luminosity is $L_{Ly\alpha} = 5.7 \pm 0.7 \times 10^{42}$ erg s^{-1}. The full width at half maximum (FWHM) after correcting for the instrumental FWHM is 370 ± 30 km s^{-1}. Since no continuum is detected in the spectrum (down to 1σ depth of 4.0×10^{-19} erg s^{-1} cm^{-2}), we can only put a lower limit on the rest-frame equivalent width (EW) of the line, EW$_0 > 40$ Å. Table 4.2 presents a summary of emission line measurements for TGSS J1530+1049.

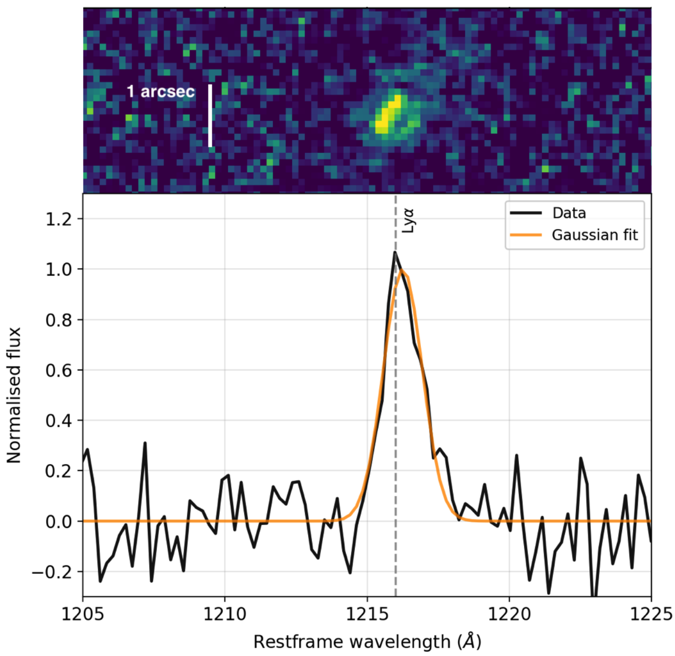

Figure 4.6: Rest-frame 1D spectrum showing the asymmetric Lyα line profile at a redshift of $z = 5.720$. Also shown is the best-fit Gaussian to the emission line. The peak of the fitted Gaussian is slightly redder than the peak of the line, suggesting asymmetry in the emission line. This is also clear from the excess towards the redder parts of the Gaussian. *Top:* The 2D GMOS spectrum showing the detected Lyα line. The spatial extent of the emission is roughly 1 arcsecond, which is also the aperture size used to extract the 1D spectrum.

4.4.1 Skewness and equivalent width

To further confirm our redshift determination, we quantify the asymmetry of the emission line following the prescriptions laid out by Kashikawa et al. (2006), by calculating the S-statistic and the weighted skewness parameter. A measure of the skewness of the emission line is particularly useful when dealing with spectra with a single emission line and can help differentiate Lyα emission at high redshifts from [O II], [O III] or Hα emission from lower redshift galaxies (Rhoads et al. 2003; Kurk et al. 2004; Kashikawa et al. 2006). We measure the skewness $S = 0.31 \pm 0.14$ and the weighted skewness $S_w = 6.44 \pm 2.97$ Å, which are consistent with what is observed for confirmed Lyα emitters at high redshift (Kashikawa et al. 2006, 2011; Matthee et al. 2017).

To check what possible values of skewness could be obtained from an unresolved [O II] doublet, we simulated the doublet with all possible ratios ($0.35 < j_{\lambda 3729}/j_{\lambda 3726} < 1.5$), convolved with the instrument resolution. We find that the skewness measured for the emission line seen in the spectrum ($S = 0.31$) is only possible for $j_{\lambda 3729}/j_{\lambda 3726} < 0.7$. These line ratios correspond to the high electron density regime when the line would be collisionally de-excited, and hence unlikely to be as strong as observed, with previous studies of the [O II] doublet in high-z galaxies (Steidel et al. 2014; Shimakawa et al. 2015; Sanders et al. 2016) also finding much higher line ratios on average. This helps drive the interpretation of the observed emission line more towards a Lyα at high redshift.

Further, an EW > 40 Å for an [O II] line originating from a presumably massive radio galaxy at $z \approx 1.2$ would be at the extreme end of the EW distribution (Bridge et al. 2015), including for radio-loud quasars (Kalfountzou et al. 2012). This EW value is also incompatible with the line ratios that would give rise to the observed skewness, as in regions of very high electron densities the [O II] line is expected to be weaker due to collisional de-excitation. Therefore, we can practically rule out the [O II] doublet as a possible identification of this emission line. An $\mathrm{EW}_0 > 40$ Å, however, is typical for Lyα emission seen in galaxies at $z \approx 5.7$ (see Kashikawa et al. 2011, for example) and generally consistent with the $z \sim 6$ galaxy population (De Barros et al. 2017).

4.4.2 K-z relation for radio galaxies

Finally, a strong indicator of a high-redshift nature of the host galaxy is the non-detection in K band down to a 3σ limiting magnitude of 22.4 (Figure 5.14) using aperture photometry at the peak pixel of the radio emission. For comparison, TN J0924$-$2201 at $z = 5.2$ has a magnitude of $K = 21.3 \pm 0.3$ and our measurement of $K > 22.4$ is consistent with $z > 5$ and helps rule out lower redshifts owing

Table 4.2: Spectroscopic redshift and emission line measurements for TGSS J1530+1049 through GMOS spectroscopy.

Property	Measurement
z_{spec}	5.720 ± 0.001
$F_{\text{Ly}\alpha}$	$1.6 \pm 0.2 \times 10^{-17}$ erg s^{-1} cm^{-2}
$L_{\text{Ly}\alpha}$	$5.7 \pm 0.7 \times 10^{42}$ erg s^{-1}
FWHM	370 ± 30 km s^{-1}
EW$_{\text{obs}}$	> 40 Å

to the $K - z$ relation for radio galaxies (note that the luminosity and the spectral index rule out that it is a star-forming galaxy). We expand upon this point in Section 4.5.3. The additional non-detection in J band down to a 3σ limit of 24.3 further favours a high redshift galaxy and supports the argument that the line we see is indeed Lyα and not [O II].

4.5 Discussion

4.5.1 Emission line measurements

The Lyα luminosity and FWHM measured for TGSS J1530+1049 are lower than what is seen for typical HzRGs at $z > 4$ (see Spinrad et al. 1995; De Breuck et al. 1999; van Breugel et al. 1999; Miley & De Breuck 2008, for examples) and more consistent with those measured for 'non-radio' Lyα emitting galaxies (LAEs) at this redshift (Rhoads et al. 2003; Ouchi et al. 2008; Kashikawa et al. 2011; Lidman et al. 2012; Matthee et al. 2017). However, the FWHM for TGSS J1530+1049 is consistent with that of a very faint radio galaxy VLA J123642+621331, with a 1.4 GHz flux density of $S_{1.4\,\text{GHz}} = 0.47$ mJy, discovered at $z = 4.424$ (Waddington et al. 1999). This galaxy has a FWHM of ≈ 420 km s^{-1} and a Lyα luminosity $\approx 2\times10^{42}$ erg s^{-1}, which is weaker than TGSS J1530+1049. VLA J123642+621331 is however, not detected in TGSS at 150 MHz down to a noise level of 3.5 mJy beam^{-1}, suggesting a relatively flat spectral index or a spectral turnover at low radio frequencies. We present some comparisons of the Lyα properties we measure for TGSS J1530+1049 with other HzRGs at $z > 4$ and also non-radio LAEs at $z = 5.7$ in Table 4.3.

A statistical sample of radio galaxies at $z \sim 6$ is needed to understand whether they are more like LAEs at high redshift or whether a majority of them continue being very different systems, surrounded by extremely overdense regions and forming stars intensively. The relatively underluminous Lyα would be one signature of a significantly neutral intergalactic medium (IGM) during the late stages of the

EoR. Weaker Lyα emission may also be caused by significant absorption in a cold and dusty medium surrounding the radio galaxy. The presence of cold gas and dust has been reported in many HzRGs, including TN J0924$-$2201 (see Klamer et al. 2005, for example) and dedicated observations to look for molecular gas and dust in a statistically significant sample of radio galaxies at $z > 5$ are required to better characterise their surrounding medium.

4.5.2 Radio properties

TGSS J1530+1049 has a flux density of 170 mJy at a frequency of 150 MHz and 7.5 mJy at 1.4 GHz (Saxena et al. 2018b). Using the standard K - corrections in radio astronomy and assuming a constant spectral index of $\alpha = -1.4$, we calculate a rest-frame radio luminosity of log $L_{150\,\mathrm{MHz}} = 29.1$ and log $L_{1.4\,\mathrm{GHz}} = 28.2$ W Hz^{-1}, which places this source at the most luminous end of the radio luminosity function at this epoch (Saxena et al. 2017). For comparison, TN J0924$-$2201 has a K-corrected radio luminosity of log $L_{1.4\,\mathrm{GHz}} = 29.3$ W Hz^{-1} using a spectral index of $\alpha = -1.6$ (van Breugel et al. 1999). TGSS J1530+1049 is close to an order of magnitude fainter than TN J09224$-$2201 at 1.4 GHz, but remains by far the brightest radio source observed this close to the end of the epoch of reionisation.

The deconvolved angular size determined by Saxena et al. (2018b) at 1.4 GHz for TGSS J1530+1049, which remains unresolved, is 0.6 arcseconds, which translates to a linear size of 3.5 kpc. This size is smaller than the size of TN J0924$-$2201 (van Breugel et al. 1999) and in line with predictions at $z \sim 6$ from Saxena et al. (2017), as radio galaxies in the early Universe are expected to be young and very compact (Blundell et al. 1999). In Table 4.4 we compare the radio properties of TGSS J1530+1049 with all currently known radio galaxies at $z > 4$. This was done by querying the TGSS ADR1 catalog to determine flux densities for all $z > 4$ radio galaxies at 150 MHz, which were then used to calculate radio powers using the standard K-corrections. We find that TGSS J1530+1049 is comparable to many of the $z > 4$ radio galaxies when looking at radio properties alone.

TGSS J1530+1049 has a spectral index of $\alpha^{150\,\mathrm{MHz}}_{1.4\,\mathrm{GHz}} = -1.4$, which is ultra-steep but flatter than TN J0924$-$2201 at $z = 5.19$, which was selected because of its spectral index of $\alpha^{365\,\mathrm{MHz}}_{1.4\,\mathrm{GHz}} = -1.6$. Interestingly, at lower radio frequencies the spectral index of TN J0924$-$2201 appears to flatten dramatically. The 150 MHz flux density measured in TGSS (Intema et al. 2017) for TN J0924$-$2201 is 760 ± 76 mJy, giving a low frequency spectral index $\alpha^{150\,\mathrm{MHz}}_{365\,\mathrm{MHz}} = -0.16$. If the spectral index were to be calculated only using the flux densities at frequencies of 150 MHz and 1.4 GHz, the inferred spectral index would be $\alpha^{150\,\mathrm{MHz}}_{1.4\,\mathrm{GHz}} = -1.06$, making it not strictly ultra-steep ($\alpha < -1.3$).

Table 4.3: Comparison of Lyα emission line properties of TGSS J1530+1049 reported in this paper with some of the known radio galaxies at $z > 4$, and the much fainter radio galaxy at $z = 4.42$ (all marked as RG), in addition to several confirmed LAEs at $z \approx 5.7$ from the literature.

Name	z	$F_{Ly\alpha}$ ($\times 10^{-17}$ erg s^{-1} cm^{-2})	$L_{Ly\alpha}$ ($\times 10^{42}$ erg s^{-1})	FWHM$_{Ly\alpha}$ (km s^{-1})	Reference
TGSS J1530+1049	5.72	1.6	5.7	370	This work
TN J0924−2201 (RG)	5.19	3.4	9.6	1500	(van Breugel et al. 1999)
J163912.11+405236.5 (RG)	4.88	18.5	47.0	1040	(Jarvis et al. 2009)
VLA J123642+621331 (RG)	4.42	0.6	2.0	420	(Waddington et al. 1999)
LALA J142546.76+352036.3	5.75	1.6	6.7	360	(Rhoads et al. 2003)
S11 5236	5.72	14.9	9.1	200	(Lidman et al. 2012)
SDF J132344.8+272427	5.72	1.1	3.7	366	(Kashikawa et al. 2011)
HSC J232558+002557	5.70	3.6	12.6	373	(Shibuya et al. 2018)
SR6	5.67	7.6	25.0	236	(Matthee et al. 2017)

Table 4.4: A comparison of the radio properties of TGSS J1530+1049 with other known radio galaxies at $z > 4$. Flux densities at 150 MHz are measured from the TGSS catalog.

Name	z	S_{150} (mJy)	$\log L_{150}$ (W Hz^{-1})	S_{1400} (mJy)	α_{1400}^{150}	Size (kpc)	Reference
TGSS J1530+1049	5.72	170	29.1	7.5	−1.4	3.5	This work
TN J0924−2201	5.19	760	29.6	71.1	−1.1	7.4	(van Breugel et al. 1999)
J163912.11+405236.5	4.88	103	28.2	22.5	−0.7	–	(Jarvis et al. 2009)
RC J0311+0507	4.51	5981	30.3	500.0	−1.1	21.1	(Parijskij et al. 2014)
VLA J123642+621331	4.42	undetected	–	0.5	–	–	(Waddington et al. 1999)
6C 0140+326	4.41	860	29.4	91.0	−1.0	17.3	(Rawlings et al. 1996)
8C 1435+635	4.25	8070	30.4	497.0	−1.2	21.1	(Lacy et al. 1994)
TN J1123−2154	4.11	512	29.1	49.3	−1.0	5.5	(Reuland et al. 2004)
TN J1338−1942	4.10	1213	29.5	120.8	−1.0	37.8	(Reuland et al. 2004)

This implies that in a search for ultra-steep spectrum radio sources using data at 150 MHz and 1.4 GHz, such as Saxena et al. (2018b), TN J0924−2201 would be missed entirely. Indeed, an indication of a generally flatter spectral index at lower frequencies is visible in the spectral indices calculated for known $z > 4$ radio galaxies between frequencies of 150 MHz and 1.4 GHz in Table 4.4. A large majority of these radio sources were selected for having an ultra-steep spectral index in a higher frequency range, but appear to have a flatter spectral index when calculated between 150 MHz and 1.4 GHz.

Spectral flattening or even a turnover at low radio frequencies is expected in radio galaxies at increasingly higher redshifts due to: a) Inverse Compton (IC) losses due to the denser cosmic microwave background that affect the higher frequencies and result in a steeper high frequency spectral index, and b) free-free or synchrotron self absorption due to the compact sizes of radio sources at high redshifts that can lead to a turnover in the low frequency spectrum (see Callingham et al. 2017, and references therein). Saxena et al. (2018b) have reported evidence of flattening of the low-frequency spectral index in candidate HzRGs and observations at intermediate radio wavelengths for sources like TGSS J1530+1049 are essential to measure spectral flattening and constrain various energy loss mechanisms that dominate the environments of radio galaxies in the early Universe. Additionally, search techniques for radio galaxies at even higher redshifts could be refined by possibly using radio colours instead of a simple ultra-steep spectral index selection. The LOFAR Two Metre Sky Survey (Shimwell et al. 2017, Shimwell et al. submitted) will eventually provide in-band spectral indices at 150 MHz and could potentially be used to identify HzRG candidates more efficiently.

We also draw attention towards the radio galaxy J163912.11+405236.5 at $z = 4.88$ (Jarvis et al. 2009), that has a spectral index of $\alpha^{325\,\mathrm{MHz}}_{1.4\,\mathrm{GHz}} = -0.75$ and is not an ultra-steep spectrum radio source. Interestingly, there is evidence of spectral flattening at lower frequencies with a 150 MHz flux density of 103.5 mJy, giving a spectral index $\alpha^{150\,\mathrm{MHz}}_{325\,\mathrm{MHz}} = -0.56$, which is flatter than that at higher frequencies. This source was targeted for spectroscopic follow-up owing to the faintness of its host galaxy at 3.6 μm. The very faint radio galaxy VLA J123642+621331 at $z = 4.42$ (Waddington et al. 1999) is also not strictly an ultra-steep spectrum source at high radio frequencies ($\alpha^{1.4\,\mathrm{GHz}}_{4.8\,\mathrm{GHz}} = -0.94$) and is too faint to be detected in TGSS. This source was also selected based on its optical and infrared faintness, suggesting that a considerable fraction of HzRGs may not be ultra-steep at all and therefore, be missed in samples constructed using the ultra-steep spectrum selection technique.

Indeed Ker et al. (2012) have shown that selecting infrared-faint radio sources (IFRS) could be more efficient at isolating HzRGs from large samples when compared to radio selection alone. This has been confirmed observationally through many previous studies (Norris et al. 2006; Collier et al. 2014; Herzog et al. 2014; Maini et al. 2016; Singh et al. 2017). However, the caveat is that deep infrared photometry over large sky areas is required to effectively implement such a selection, which can be expensive. The recently concluded UKIRT Hemisphere Survey (UHS; Dye et al. 2018) has the potential to be extremely useful in the identification of promising HzRG candidates in the Northern Hemisphere, particularly from the LOFAR surveys (Shimwell et al. 2017, Shimwell et al. submitted), as a combination of a relaxed spectral index steepness criterion and infrared-faintness could be more effective at isolating HzRGs.

4.5.3 Stellar mass limits

The non-detection of the host galaxy down to a 3σ depth of $K = 22.4$ can be used to set limits on the stellar mass for TGSS J1530+1049 using simple stellar population synthesis modelling. To do this, we make use of the PYTHON package SMPY[1], which is designed for building composite stellar populations in an easy and flexible manner, allowing for synthetic photometry to be produced for single or large suites of models (see Duncan & Conselice 2015). To build stellar populations, we use the Bruzual & Charlot (2003) model with a Chabrier (2003) initial mass function (IMF) and solar metallicity (Willott et al. 2003), a formation redshift $z_f = 25$ and assume a maximally old stellar population that has been forming stars at a constant rate (Lacy et al. 2000). We follow the Calzetti et al. (2000) law for dust attenuation and use values of $A_v = 0.15$ (moderate extinction) and 0.5 mag (dusty), which are commonly seen in massive galaxies at $5 < z < 6$ (McLure et al. 2006). The synthetic photometry is produced for different stellar masses, which we then convolve with the K band filter to calculate apparent K magnitudes over a redshift range $0 - 7$.

The K magnitude limit for TGSS J1530+1049 fits well with a stellar mass limit of $M_{\text{stars}} <\sim 10^{10.25}\ M_{\odot}$ for $A_v = 0.15$ mag, and $M_{\text{stars}} <\sim 10^{10.5}$ for $A_v = 0.5$ mag. We note here that thanks to the excellent seeing for K-band observations ($0.6 - 0.8$ arcseconds), and since at $z \sim 6$ the host galaxy is expected to be small, any aperture correction is only expected to be at the level of a few tenths of a magnitude at most, or $0.1 - 0.2$ in the logarithmic stellar mass, which is smaller than the uncertainty from dust extinction corrections.

We find that the stellar mass limits we infer are in agreement with the J band 3σ limit from LBT. The photometry predicted by the models in the optical bands from PS1 (g, r, i, z, y) is also consistent with the non-detections that we report. This stellar mass limit places TGSS J1530+1049 towards the $> M^*$ end of the

[1] `https://github.com/dunkenj/smpy`

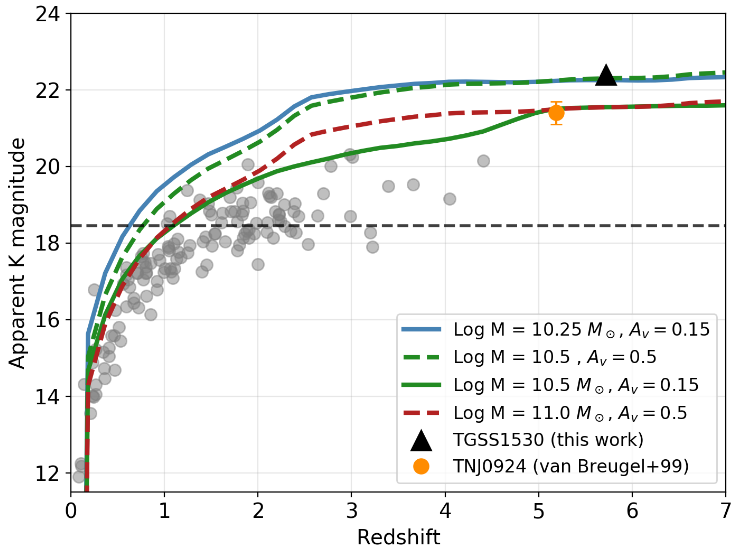

Figure 4.7: The '$K - z$' diagram for radio galaxies, showing stellar mass limits derived from stellar population synthesis modelling for TGSS J1530+1049 (black triangle). The K-band 3σ limit gives $M_{\rm stars} < 10^{10.25}\ M_\odot$ for $A_v = 0.15$ mag, and $M_{\rm stars} < 10^{10.5}$ for $A_v = 0.5$ mag. Also shown are K-band magnitudes and redshifts for known radio galaxies in the literature (grey points; see text), with TN J0924−2201 at $z = 5.19$ (orange circle). The K-band limits for TGSS J1530+1049 further help exclude lower redshift measurements from incorrect line identification.

galaxy stellar mass function at $z \sim 6$ (see Duncan et al. 2014, for example). For comparison, we show the apparent K band magnitudes of other radio galaxies in the literature, taken from the 3CRR, 6CE, 6C* and 7C−I/II/III samples (Willott et al. 2003), in Figure 4.7. Also shown is the K magnitude for TN J09224−2201 at $z = 5.2$ (van Breugel et al. 1999), which is best fit with a stellar mass of $10^{10.5}$ $M_{\odot}$ for $A_v = 0.15$ mag and 10^{11} $M_{\odot}$ for $A_v = 0.5$ mag.

We also show the K-band magnitude limit for the UKIDSS LAS as a dashed black line in Figure 4.7. TGSS J1530+1049 was initially selected due to its non-detection in LAS. However, these magnitude limits alone were not sufficient to constrain the very high redshift nature of the host galaxy. With deeper LBT observations in K band, we show that TGSS J1530+1049 follows the trend in the $K - z$ plot for radio galaxies. It is also clear that a low redshift solution that would arise if the detected emission line in Section 4.4 is not Lyman alpha (for example, $z \approx 1.2$ if the line is [O II]) would be hard to explain using galaxy evolution models with the inputs and assumptions outlined above and those generally used to model radio galaxy spectra (Overzier et al. 2009).

A stellar mass limit of $M_{\star} < 10^{10.5}$ $M_{\odot}$ for TGSS J1530+1049 (based on the outlined assumptions) is almost an order of magnitude lower than the sample of radio galaxies studied by Rocca-Volmerange et al. (2004), where the highest stellar masses are seen for radio galaxies in the redshift range $2 - 4$. This suggests that TGSS J1530+1049 is still evolving and is in the process of building up its stellar mass. This interpretation is in line with TGSS J1530+1049 being a relatively young radio galaxy owing to its small radio size, and lower stellar masses may be expected from radio galaxies close to or into the epoch of reionisation. Robust detections at optical and infrared wavelengths are required to properly characterise the galaxy spectral energy distribution in order to understand better the star formation history of TGSS J1530+1049.

4.6 Conclusions

In this paper we have presented the discovery of the highest redshift radio galaxy, TGSS J1530+1049, at $z = 5.72$. The galaxy was initially selected at 150 MHz from TGSS (Saxena et al. 2018b) and was assigned a high priority for spectroscopic follow-up owing to its compact morphology and faintness at optical and near-infrared wavelengths. The conclusions of this study are listed below:

1. Long-slit spectroscopy centered at the radio position of the source revealed an emission line at 8170 Å, which we identify as Lyman alpha at $z = 5.720$. We rule out alternative line IDs owing to the absence of other optical/UV

lines in the spectrum, the asymmetrical nature of the emission line characteristic of Lyman alpha at high redshifts that we quantify using the skewness parameter and the high observed equivalent width of the emission line.

2. Deep J and K band imaging using the Large Binocular Telescope led to no significant detection of the host galaxy down to 3σ limits of $K > 22.4$ and $J > 24.4$. The limits in K can be used as an additional constraint on the redshift, owing to the relation that exists between K band magnitude and redshift of radio galaxies. The magnitude limit is consistent with $z > 5$, practically ruling out a redshift of $z \approx 1.2$ that would be expected if the emission line were an unresolved [O II] $\lambda\lambda 3726, 3729$ doublet, which is the most likely alternative line identification.

3. The emission line is best fitted with a skewed Gaussian, giving an integrated line flux of $F_{Ly\alpha} = 1.6 \times 10^{-17}$ erg s^{-1} cm^{-2}, a Lyα luminosity of 5.7×10^{42} erg s^{-1}, an equivalent width of EW $>$ 40 Å and a FWHM of 370 km s^{-1}. These values are more consistent with those observed in non-radio Lyman alpha emitting galaxies at this redshift and much lower than those corresponding to typical radio galaxies at $z > 4$.

4. The radio luminosity calculated at 150 MHz is $\log L_{150} = 29.1$ W Hz^{-1}, which places it at the most luminous end of the radio luminosity function at this epoch. The deconvolved angular size is 3.5 kpc, which is in line with the compact morphologies expected at high redshifts. We find that the radio properties of TGSS J1530+1049 are comparable to other known radio galaxies at $z > 4$ but the compact size suggests that it is a radio galaxy in an early phase of its evolution. A joint study of the Lyα halo and the radio size of this source may provide one of the earliest constraints on the effects of radio-mode feedback.

5. We use the K band limit to put constraints on the stellar mass estimate using simple stellar population synthesis models. Assuming a constant star formation history and a maximally old stellar population, we derive a stellar mass limit of $M_{\text{stars}} <\sim 10^{10.25}$ $M_\odot$ for $A_v = 0.15$ mag, and $M_{\text{stars}} <\sim 10^{10.5}$ for $A_v = 0.5$ mag. These limits are almost an order of magnitude lower than typical radio galaxy masses in the redshift range $2 - 3$ and suggest that TGSS J1530+1049 may still be in the process of assembling its stellar mass, which is in line with it being a relatively young radio galaxy.

An effective application of deep radio surveys covering very large areas on the sky has been demonstrated by this discovery of the first radio galaxy at a record distance after almost 20 years. With the more sensitive, large area surveys currently underway with LOFAR (LoTSS; Shimwell et al. 2017, Shimwell et al. submitted), there is potential to push searches for radio galaxies to even higher redshifts. Discovery of even a single bright radio galaxy at $z > 6$ would open up new ways to study the epoch of reionisation in unparalleled detail, through searches for the 21cm absorption features left behind by the neutral hydrogen that pervaded the Universe at high redshifts.

Acknowledgements

The authors thank the referee for useful comments and suggestions. AS would like to thank Jorryt Matthee, David Sobral, Reinout van Weeren and Nobunari Kashikawa for fruitful discussions. AS, HJR and KJD gratefully acknowledge support from the European Research Council under the European Unions Seventh Framework Programme (FP/2007-2013)/ERC Advanced Grant NEWCLUSTERS-321271. RAO and MM received support from CNPq (400738/2014-7, 309456/2016-9) and FAPERJ (202.876/2015). PNB is grateful for support from STFC via grant ST/M001229/1. IP acknowledges funding from the INAF PRIN-SKA 2017 project 1.05.01.88.04 (FORECaST).

This paper is based on results from observations obtained at the Gemini Observatory, which is operated by the Association of Universities for Research in Astronomy, Inc., under a cooperative agreement with the NSF on behalf of the Gemini partnership: the National Science Foundation (United States), the National Research Council (Canada), CONICYT (Chile), Ministerio de Ciencia, Tecnología e Innovación Productiva (Argentina), and Ministério da Ciência, Tecnologia, Inovação e Comunicações (Brazil). This paper also contains data from the Large Binocular Telescope (LBT), an international collaboration among institutions in the United States, Italy and Germany. LBT Corporation partners are: The University of Arizona on behalf of the Arizona university system; Istituto Nazionale di Astrofisica, Italy; LBT Beteiligungsgesellschaft, Germany, representing the Max-Planck Society, the Astrophysical Institute Potsdam, and Heidelberg University; The Ohio State University, and The Research Corporation, on behalf of The University of Notre Dame, University of Minnesota, and University of Virginia.

This work has made extensive use of IPYTHON (Pérez & Granger 2007), ASTROPY (Astropy Collaboration et al. 2013), APLPY (Robitaille & Bressert 2012), MATPLOTLIB (Hunter 2007b) and TOPCAT (Taylor 2005). This work would not have been possible without the countless hours put in by members of the open-source developing community all around the world.

5 | Search for faint high-redshift radio galaxies II: spectroscopic and near-infrared observations

We present spectroscopic and near-infrared observations of a sample of faint radio sources selected initially selected as promising high-redshift radio galaxy (HzRG) candidates. We have determined redshifts for a total of 12 radio galaxies with redshifts ranging from $0.52 \leqslant z \leqslant 5.72$. Our sample probes radio luminosities that are almost an order of magnitude fainter than previous large samples at the highest redshifts. We use near-infrared photometry for a subsample of these galaxies to calculate stellar masses using simple stellar population models, and find stellar masses to be in the range $10^{10.8} - 10^{11.7} M_{\odot}$. We then compare our faint radio galaxies with brighter radio galaxies at $z \geqslant 2$ from the literature. We find that fainter radio galaxies have lower Lyα luminosities and full width at half maxima (FWHM) in comparison to the bright radio galaxies, implying that faint HzRGS are powered by photoionisation from weaker AGN. We also rule out the presence of shocks in faint HzRGs. The stellar masses determined for faint HzRGs are also lower that what has been observed for brighter ones. We find indications that faint HzRGs are likely in the process of building up their stellar mass through cold accretion of gas. Further, we find that the overall redshift evolution of radio sizes of $z > 2$ radio galaxies is fully compatible with increased inverse Compton scattering losses at high redshifts.

Based on:
Saxena A., Röttgering H.J.A., Best P.N., Duncan K.J., Hill G.J., Indahl B.L., Marinello M., Overzier R.A., Pentericci L., Prandoni I.
In preparation

5.1 Introduction

High-redshift radio galaxies (HzRGs) have been found to be hosted by some of the most massive galaxies in the universe and are thought to be progenitors of the massive ellipticals we observe today. HzRGs contain large amounts of dust and gas (Best et al. 1998b; Archibald et al. 2001; Carilli et al. 2002a; Reuland et al. 2004; De Breuck et al. 2010), are dominated by an old stellar population (Best et al. 1998a; Rocca-Volmerange et al. 2004; Seymour et al. 2007) and seen to have high star formation rates (Willott et al. 2003; McLure et al. 2004; Miley et al. 2006; Villar-Martín et al. 2007a; Seymour et al. 2008). Owing to the large stellar masses of their host galaxies, radio-loud AGN across all redshifts are often found to be located in the centre of clusters and proto-clusters (Pentericci et al. 2000; Venemans et al. 2002; Röttgering et al. 2003; Miley et al. 2004; Hatch et al. 2011; Wylezalek et al. 2013; Orsi et al. 2016). Miley & De Breuck (2008) summarise the properties of radio galaxies and their environments in their review.

HzRGs are seen to be some of the most massive galaxies across all redshifts (see Rocca-Volmerange et al. 2004, for example). As a result, near-infrared magnitudes of radio galaxies have been observed to follow a correlation with redshift, which is known as the $K - z$ relation (Jarvis et al. 2001b; Willott et al. 2003; Rocca-Volmerange et al. 2004). This is mainly because of the consistently high stellar masses observed and because HzRGs are thought to be dominated by an old stellar population, and the K band traces the part of SED that contains light emitted from these old stars. At higher redshifts ($z > 4$), the scatter in the $K - z$ relation is seen to increase as bluer parts of the rest-frame SED containing light from younger stars (which is more sensitive to the star-formation history) are observed in the K band.

Selecting HzRGs based on their radio emission alone has the advantage that no prior colour selection (one that probes the Lyman break, for example) is applied (De Breuck et al. 2000a). In principle, promising high-redshift candidates selected from a radio survey with follow-up optical/IR spectroscopy could discover massive galaxies all the way into the epoch of reionisation through observations of their redshifted synchrotron spectrum. Since radio observations are not affected by dust, radio selected galaxies can also provide an unbiased sample to study the dust properties of galaxies at high redshifts.

A successful method of identification of HzRGs from all-sky radio surveys is to first create samples of radio sources that display an ultra-steep spectral index (α, where $S \propto \nu^{\alpha}$) and then follow these up at optical and infrared wavelengths (Tielens et al. 1979; Röttgering et al. 1994; Chambers et al. 1996; Blundell et al. 1999; De Breuck et al. 2000a; Ishwara-Chandra et al. 2010; Afonso et al. 2011;

Singh et al. 2014). This method is effective owing to the apparent correlation that exists between the redshift of a radio source and the steepness of its low-frequency radio spectrum (see Ker et al. 2012, for example). The physical explanation for this correlation is still under debate, but it is commonly accepted that curvature of the radio SED combined with a K-correction is responsible for the apparent correlation. For a more thorough discussion on the redshift-spectral index correlation, we point the readers to Miley & De Breuck (2008) where some other possible explanations are also discussed. From an observational point of view, however, radio sources with an ultra-steep spectrum (USS) generally make promising HzRG candidates. Most of the currently known radio galaxies at the highest redshifts have been selected from relatively shallow all-sky surveys. Therefore, the well-studied HzRG samples (Laing et al. 1983; van Breugel et al. 1999; Willott et al. 1999; De Breuck et al. 2000a; Rawlings et al. 2001; Jarvis et al. 2001a; Willott et al. 2003; Vardoulaki et al. 2010; Rigby et al. 2011) consist of luminous radio sources and very little is currently known about the fainter and presumably more abundant radio galaxies at high redshifts. With the advent of the latest generation of radio telescopes such as the upgraded GMRT, LOFAR, MWA and SKA in the future, it is now possible to survey large areas of the sky to unprecedented depths at low radio frequencies and push the discovery of radio galaxies to lower luminosities and/or to higher redshifts, well into the epoch of reionisation (EoR; $z > 6$).

The spectra of radio galaxies across all redshifts are rich with emission lines and there have been many studies exploring the primary source of photoionisation in radio galaxies and AGN using UV and optical emission lines and their ratios. Robinson et al. (1987) and Baum et al. (1992) found that photoionisation by the central AGN alone was found to sufficiently explain the UV and optical line ratios observed in low redshift radio galaxies ($z < 0.2$). However, for radio galaxies at higher redshifts, photoionisation by AGN was not enough to explain the observed blue colours and bright Lyα emission observed in these objects (Villar-Martin et al. 1997). Further, there is evidence of strong interaction between the radio jet and the interstellar medium (ISM) of the host galaxy, that leads to the generation of powerful shocks that disturb the morphology, kinematics and physical conditions of the line-emitting gas (van Ojik et al. 1996; McCarthy et al. 1996; Villar-Martin et al. 1997). This interaction is also supported by observations that show close alignment between the radio jet and the extended emission line regions of HzRGs (Miley et al. 1992; Jannuzi et al. 1995). More recently, observations of the alignment of molecular gas with the radio jet in distant radio galaxies has lent further support to the jet-gas interaction scenario in radio galaxies (see Emonts et al. 2014, for example).

In this paper, we first present results from a campaign to spectroscopically

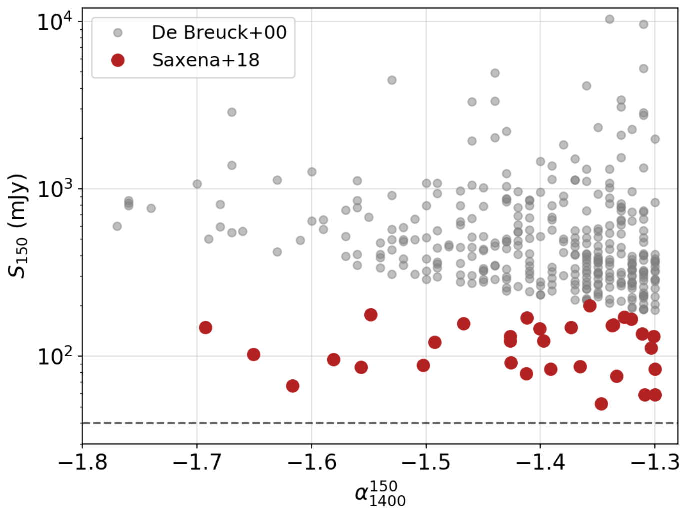

Figure 5.1: The unique parameter space in flux density and spectral index probed by the Saxena et al. (2018a) sample of ultra-steep spectrum radio sources selected from TGSS ADR1. Shown for comparison are the radio sources from De Breuck et al. (2000a). Going to fainter flux densities should open up the potential for discovering radio galaxies at higher redshifts than seen before, and lead to the discovery of fainter radio galaxies at all redshifts, providing a more complete picture of the radio galaxy population.

follow-up the faint HzRG candidates identified by Saxena et al. (2018a) and observe a subset of these at near-infrared wavelengths. These radio sources were initially selected at a frequency of 150 MHz from the TIFR GMRT Sky Survey Alternative Data Release 1 (TGSS ADR1; Intema et al. 2017), probing a new flux density regime by going fainter than before (as shown in Figure 5.1) over a large area of the sky ($\sim$ 10000 square degrees). We then combine these newly confirmed HzRGs with $z \geqslant 2$ radio galaxies from the literature to create an extended HzRG sample. We explore correlations between emission-line and radio properties for this extended sample and present some scenarios that may help explain the observed trends.

The layout of this paper is as follows. In Section 5.2 we present our new sample of spectroscopically confirmed radio galaxies. We first briefly describe the sample selection, observations and data reduction methods. We then present the spectroscopic and galaxy properties derived for the new radio galaxy sample, which probes fainter flux densities than previous all-sky radio surveys across all redshifts. In Section 5.3 we compare the properties of the faint high-redshift ($z > 2$) radio galaxies presented in this paper with known radio galaxies at $z \geqslant 2$ in the literature. We then explore various correlations between radio properties such as luminosity, size and spectral index with emission line properties such as line luminosity and widths in both the faint and literature HzRG samples. In Section 5.4 we present a discussion about the nature of faint HzRGs and some overall trends observed in the radio galaxy samples. Finally, in Section 5.5 we summarise the key findings of this study.

Throughout this paper we assume a flat ΛCDM cosmology with $H_0 = 70$ km s^{-1} Mpc^{-1} and $\Omega_m = 0.3$.

5.2 The faint HzRG sample

5.2.1 Sample selection

The HzRG candidates targeted for spectroscopy are mainly selected on the basis of (i) steepness of their spectral index ($\alpha_{1400}^{150} < -1.3$) calculated by cross-matching with the VLA FIRST survey at 1.4 GHz (Becker et al. 1995) and (ii) compact morphologies (largest angular size < 10 arcsec), which are expected from radio galaxies at the highest redshifts (Saxena et al. 2017). Lower flux density limits were applied both at 150 MHz and 1.4 GHz to ensure a high enough signal to noise ratios and upper flux density limits were applied at 150 MHz to ensure that none of the sources in our final sample would have been detected in previous searches for ultra-steep spectrum radio sources (for example De Breuck et al. 2000a). Further, only those sources with no clear optical or infrared counterparts in the available all-sky surveys such as SDSS (Alam et al. 2015b), PanSTARRS1 (Chambers et al. 2016b), ALLWISE (Wright et al. 2010b), UKIDSS LAS (Lawrence et al. 2007b) were retained in the final sample, increasing the likelihood of a high redshift nature of the radio host.

The final sample consisted of 32 radio sources that were followed up with the Karl G. Jansky Very Large Array (VLA) in configuration A (Project code: 16B-309, PI: Röttgering), which at a frequency of 1.4 GHz yielded an average beam size of 1.3 arcseconds. These results are presented in Saxena et al. (2018a). The high-resolution VLA images enabled sub-arcsecond isolation of the expected optical counterpart of the radio source. Blind spectroscopy at the position of the expected host of a radio source has been found to be successful at detecting emission lines and obtaining redshifts.

5.2.2 Observations and data reduction

Table 5.1: Observational setups used in this study.

Telescope	Instrument	Date	Grism/Grating	λ coverage ()	Exp. time (sec)
WHT	ISIS	24 – 27 July 2017	R300B	3200 – 5000	1800 – 3600
			R158R	5300 – 9200	
Gemini North	GMOS long-slit	7 April – 24 June 2017	R400_G5305	5600 – 9400	2400
HET	LRS2 IFU	December 2016 – March 2018	LRS2-B	3700 – 6300	3600
			LRS2-R	6500 – 10500	3600

Spectra presented in this paper were obtained over a period of December 2016 – March 2019 using three different telescopes, namely the 10m Hobby-Eberly Telescope (HET) at McDonald Observatory, Texas, the 8.2m Gemini North at Hawaii and the 4.2m William Herschel Telescope (WHT) at La Palma, Canary Islands. We used long-slit setups with Gemini and WHT and the integral field unit (IFU) setup with the HET. The typical observing times were one hour per object. The radio morphologies for most of the targets were unresolved (at a beam size of ~ 1.3 arcseconds and for these targets we aligned the slit at a parallactic angle of 0 degrees. For resolved radio objects, the slit was aligned along the extended radio morphology as radio galaxy hosts are typically extended over a few arcseconds and oriented along the radio axis (Röttgering et al. 1997). IFU observations were simply centred on the expected location of the radio host galaxy. Below we describe the observations taken using each telescope in detail. An overview of the setups used in various observing runs is given in Table 5.1.

4.2m William Herschel Telescope

The observations at the WHT were carried out using the Intermediate dispersion Spectrograph and Imaging System (ISIS) instrument with a 3 arcminute slit length and a slit width of 1.5 arcseconds (Program IDs: W17AN014 and W19AN015, PI: Saxena). We used the R300B grating in the Blue arm and the R158R grating in the Red arm of the spectrograph, providing a spectral resolution of R ~ 975 and R ~ 910, respectively and a total spectral range of ~ 3200 to ~ 9200 over both arms. The first set of observations were carried out from 24 to 27 July 2017. The first two nights of the observing run were strongly affected by Saharan dust covering the island, leading to extinction of up to 2 mags in worst conditions. The conditions improved significantly for the final two nights. The average seeing was around $0.6''$.

Standard afternoon calibrations were performed and both dome and sky flats were taken before and after each observing night. A flux standard was observed at the beginning and the end of each night. Each target was observed for a total of 3600 (1800×2) seconds in each arm simultaneously, except when a bright line or continuum was spotted after the first 1800 seconds. In such cases the second exposure was terminated earlier. We used CuAr + CuNe lamps for wavelength calibration, which were observed at the position of each target before the sky exposure. Since the optical magnitudes of the targets are very faint ($R > 23.5$ AB), we first acquired a bright star close to the target and then added offsets to arrive at the target coordinates. This ensures accurate positioning of the slit for very faint targets. Standard data reduction procedures that include bias subtraction, flat fielding, sky subtraction, wavelength calibration and flux calibration were performed using PYTHON scripts written by our team. These scripts were based on the WHT data reduction package written by Steve Crawford[1].

8.2m Gemini North

The observations at Gemini North were carried out using the Gemini Multi-Object Spectrograph (GMOS) in long-slit mode with a slit width of $1.5''$ and a slit length of 5 arcminutes (Program ID: GN-2017A-Q-8, PI: Overzier) . A total observing time of 7 hours was used to observe six targets. The observations were carried out over a period of two months, from 7 April 2017 to 24 June 2017. We used the R400_G5305 grating with a central wavelength of 700 nm, giving a resolution of $R \sim 1500$, providing coverage over the wavelength range $3600 - 9400$ Å. We took three exposures of 800s each, giving 2400s of exposure time per object.

We used the Gemini IRAF package[2] for reducing the data, which performed all the basic reductions including bias subtraction, dark subtraction, flat-fielding and cosmic-ray removal. Wavelength and flux calibration was then performed on the spectra using the pipeline tools.

10m Hobby-Eberly Telescope (HET)

The observations at the HET were carried out using the Low Resolution Spectrograph 2 (LRS2), which is a 7×12 sq. arcsec fiber integral-field unit (IFU), covering a wavelength range of $3500 - 11000$ with a resolving power of R $\sim$ 1800. The wavelength range on the LRS2 is split into two spectrographs, the LRS2-B ($3500 - 6300$) and LRS2-R ($6300 - 11000$). The observations were taken in spectroscopic sky conditions over four trimesters, beginning in December 2016 and ending in March 2018 (PI: Hill).

We used the LRS2 data reduction package[3] written in PYTHON to perform the basic reduction of the IFU data. The reduction steps include bad pixel masking, bias subtraction, flat fielding, cosmic ray removal and wavelength calibration using arc lamps (taken with either Cd, Hg, FeAr, or Kr) for individual frames from both blue and red arms. The reduced data products include both 2D row-stacked spectra (RSS) and 3D data cubes. The individual RSS and cubes were then median combined to form the final science data products.

The presence of line emission in the data was first identified by visually examining the 2D spectra. Where signs of an emission line were spotted, we looked at

[1] can be found at:
`https://github.com/crawfordsm/wht_reduction_scripts`

[2] `https://www.gemini.edu/sciops/data-and-results/processing-software`

[3] `https://github.com/BrianaLane/LRS2_reduction`

Table 5.2: Number of objects observed and number of detections during runs on different telescopes. There are a few objects that have duplicate observations on multiple telescopes. We also count continuum detections in these numbers, but their spectra have not been presented in this study.

Telescope (Run)	Observed	Detected	Detections	1σ depth (erg s^{-1} cm^{-2} Å^{-1})
WHT (W)	12	7	58%	1.1×10^{-18}
HET (H)	15	8	55%	XX
Gemini North (G)	6	5	83%	1.0×10^{-18}

the spatial distribution of the line emission in the 3D data cube. When the full spatial extent of the emission line was determined by eye, we used a circular aperture that fully encompassed the emitting region with a signal-to-noise of 3 or above, to extract the pixels with line emission. The 1D spectra from all pixels within the aperture were then median stacked to create a 1D spectrum of the source. The LRS2-B and -R response functions were then used to calibrate the flux of the extracted 1D spectrum and emission lines were then identified using methods that are described in the following section.

We observed different targets in each of our spectroscopy runs on the three different telescopes listed above but there were a few targets that were observed using two or more telescopes owing to scheduling restrictions. We list the number of targets observed and the number of detections, either emission lines or continuum, recorded during all our runs in Table 5.2. In the next section we summarise the flux limits achieved and detection rates from each of our observing runs.

Near-infrared imaging

Additional near infrared imaging in the J and K bands was obtained using LUCI (formerly known as LUCIFER) on the Large Binocular Telescope for 9 HzRG candidates in our sample. Of these, 7 had spectroscopically confirmed redshifts. Below we highlight the observations and data reduction strategy.

The observations were carried out in two separate runs, with the first on 1 February 2018 and the second on 11 May 2018 (Program ID 2017 2018 43; PI: Prandoni). The average seeing throughout the observations was $0.6 - 1.0$ arcseconds. The average on-source exposure times were 720 (12×60s) seconds in J (central wavelength of 1.247 microns) and 1200 (20×60s) in K (central wavelength of 2.194 microns). We used a standard jitter pattern with a maximum jitter distance of 15 arcseconds to enable effective sky subtraction in both bands.

The LUCI data reduction pipeline developed at INAF-OAR was used to perform the reductions and calibrations of raw images. These tasks include dark subtraction, bad pixel masking, cosmic ray removal, flat-fielding, and sky subtraction. Astrometric corrections for individual frames were calculated and applied and the corrected frames were then resampled and combined using a weighted co-addition method to obtain a deep image. The photometry of the co-added image was then calibrated using 2MASS and where available, UKIDSS Large Area Survey to an accuracy of within 0.1 mag. The median and standard deviation of the background in all co-added images were then calculated by placing random apertures with a diameter of 1.5 arcseconds.

5.2.3 Results

Flux limits and detection rates

The median 1σ flux limit achieved in the first observing run on WHT was 1.1×10^{-18} erg s^{-1} cm^{-2} Å^{-1}. We targeted 12 sources in total and were able to detect 7 (either emission lines or continuum). The flux limits reached during observations with the Hobby-Eberly Telescope range from XX - YY. The variation in these limits is mainly down to the variation in the observing conditions, as the observations were taken over a long period of time. The flux limits reached using Gemini North are 1.0×10^{-18} erg s^{-1} cm^{-2} Å^{-1}.

Redshift determination and emission line measurements

After applying all the calibrations, the identification of emission lines in the extracted 1D spectra was attempted. The spectra of radio galaxies are dominated by one or several of the following emission lines: Lyα λ1216, [O II] λ3727, [O III] λ5007, Hα λ6563 + [N II] λ6583 (McCarthy 1993; Röttgering et al. 1997; De Breuck et al. 2001) and the initial redshift determination was based on the identification of one or more of these lines. Relatively fainter lines such as C IV λ1549, He II λ1640, C III] λ1909, C II] λ2326 and Mg II λ2800 were then used in case of ambiguity arising from the identification of the stronger emission lines. For objects with a single emission line in the spectrum, we used the shape and the equivalent width of the emission line, in addition to near infrared magnitudes (where available) to identify the emission line for redshift determination. For example, an asymmetric line profile (combined with a faint near-infrared magnitude) would be a strong indicator of Lyα at high redshifts.

Once the redshift was determined we derived the integrated flux and full width at half maximum (FWHM), by fitting a single Gaussian to the emission line. In a few cases we detect double peaked emission lines (mostly Lyα λ1216 and [O II] λ3727), but for the purposes of this study we smoothed the spectrum in order to fit a single Gaussian to such lines. The above line identification methods yielded reliable redshifts for a total of 12 objects, which are presented in Table 5.3. Also shown are the flux densities and calculated radio luminosities at 150 MHz from Saxena et al. (2018a). The 1D spectra are shown in Figure 5.15 in Appendix A.

Notes on individual object spectra

1. USS7, $z = 0.52$

   Two emission lines, [O III] and [O II] at a redshift of $z = 0.52$ are detected in the spectrum. This source is slightly resolved in the radio image and the [O III] and [O II] line strengths suggest that this source is a faint high-excitation radio galaxy[4].

2. USS483, $z = 0.86$

   This object has an interesting spectrum, with only one bright emission line visible at 9291 . There is also faint continuum visible around the emission line, therefore ruling out the line identification as Lyα. We tentatively identify this line as [O III], giving a redshift of $z = 0.86$. We do not detect [O II] in the spectrum, which implies that this must be a HERG (Best & Heckman 2012). The long-slit was aligned along the radio axis (Figure 5.2, top) and the line emission in the 2D spectrum (Figure 5.2, bottom) is extended along the radio axis, which implies interaction between the jet and the gas surrounding the host galaxy. The line emission can be seen extending up to 15 arcseconds, pointing towards the possibility of large scale emission line halos around the central radio galaxy.

3. USS43, $z = 1.46$

   A redshift of $z = 1.46$ was confirmed using the [O II] and Mg II emission lines. Also detected in the spectrum are Ne V and slightly blue-shifted C II], which is blue-shifted by about 30 in the observed frame. When applying a smoothing kernel to the spectrum, we also see faint C III] and C IV emission. C III] is also blue-shifted by 30 whereas C IV is not, suggesting that the C IV may be tracing emission from the central AGN. The host galaxy is detected in near-infrared (NIR) with $K = 21.6 \pm 0.2$ AB.

[4] High-excitation radio galaxies (HERGs) are a class of radio galaxies that show strong high-excitation emission lines. A characteristic feature of HERGs is their high [O III] equivalent widths (> 3) and higher [O III]/[O II] ratios (see Best & Heckman 2012, for example).

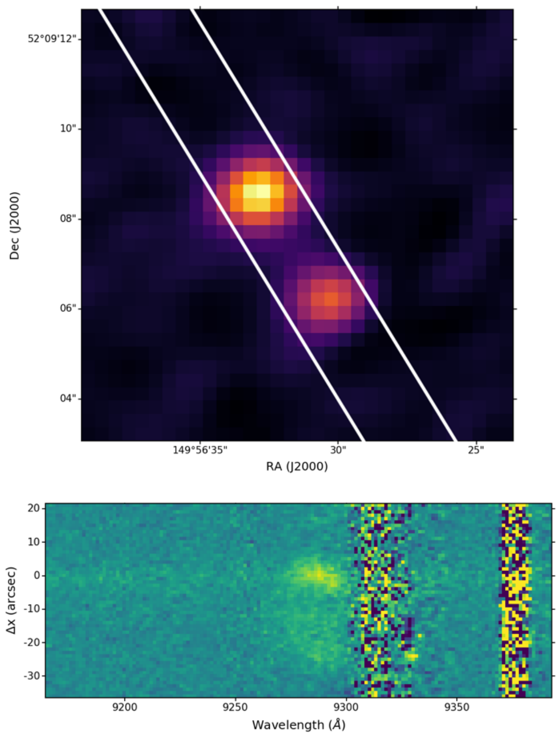

Figure 5.2: Top: VLA image of USS483 at 1.4 GHz, with a beam size of $\sim 1.3''$. Also shown is the position of the GMOS long-slit, aligned along the radio axis. Bottom: The 2D line emission that we identify as [O III] at $z = 0.86$. The line emission is spatially extended along the radio axis, with emission extending all the way to $\sim 15''$ away from the central host galaxy. This behaviour is a clear sign of interaction between the radio jet and the surrounding gas.

Table 5.3: Details of detected emission lines, radio flux densities and luminosities at 150 MHz, and radio sizes of galaxies in this paper. The source IDs, radio flux densities and sizes are taken from Saxena et al. (2018a). We also give the telescope that was used to observe each source in the Tel. column. 'W' stands for William Herschel Telescope, 'G' for Gemini North and 'H' for Hobby-Eberly Telescope.

Source ID	z	Tel.	Line	Flux (10^{-17} erg s^{-1} cm^{-2})	Luminosity (10^{41} erg s^{-1})	FWHM (km s^{-1})	$S_{150\,\mathrm{MHz}}$ (mJy)	$\log L_{150\,\mathrm{MHz}}$ (W Hz^{-1})	LAS$_{\mathrm{rad}}$ (kpc)
USS7	0.52	W	[O II] λ3727	4.5 ± 3.3	0.5 ± 0.3	970 ± 60	122 ± 24	26.2 ± 0.7	21.6 ± 0.6
			[O III] λ5007	8.3 ± 2.1	0.9 ± 0.2	460 ± 30			
USS483	0.86	G	[O III] λ5007	36.6 ± 1.7	13.0 ± 0.6	1050 ± 60	89 ± 16	26.4 ± 0.7	18.8 ± 0.8
USS43	1.46	W	Mg II λ2800	5.0 ± 3.4	6.9 ± 4.7	640 ± 50	200 ± 40	27.6 ± 0.7	5.8 ± 0.8
			[O II] λ3727	40.0 ± 3.0	55.0 ± 4.1	1380 ± 80			
USS182	2.02	H	Lyα	32.6 ± 5.0	96.5 ± 14.8	1420 ± 60	146 ± 30	27.8 ± 0.7	24.2 ± 0.8
USS18	2.06	H	Lyα	77.9 ± 4.3	242.0 ± 13.4	950 ± 60	131 ± 26	27.8 ± 0.7	9.5 ± 0.8
USS320	2.20	W, H, G	Lyα	8.7 ± 3.8	31.7 ± 13.9	1300 ± 100	86 ± 17	27.9 ± 0.7	19.6 ± 0.8
			Mg II λ2800	3.2 ± 1.1	12.1 ± 4.1	320 ± 30			
USS268	2.35	W, H	Lyα	22.8 ± 2.8	97.6 ± 12.0	750 ± 50	92 ± 18	27.8 ± 0.7	12.6 ± 0.8
			Mg II λ2800	5.2 ± 3.0	23.2 ± 13.4	320 ± 30			
USS98	2.61	W, G	Lyα	20.4 ± 1.6	112.7 ± 8.8	810 ± 30	178 ± 36	28.3 ± 0.7	56.9 ± 0.8
USS206	4.01	W	Lyα	241.6 ± 41.9	3925.1 ± 680.6	1935 ± 270	102 ± 20	28.5 ± 0.7	58.7 ± 0.8
USS172	4.11	H	Lyα	5.2 ± 0.7	85.3 ± 11.5	570 ± 30	124 ± 25	28.6 ± 0.7	65.9 ± 0.7
USS188	4.57	H	Lyα	6.8 ± 0.7	143.3 ± 14.8	520 ± 20	166 ± 33	28.8 ± 0.7	26.2 ± 0.7
USS46	4.86	H	Lyα	5.1 ± 0.8	124.2 ± 20.0	500 ± 30	87 ± 17	28.7 ± 0.7	6.2 ± 0.6
USS202	5.72	G	Lyα	1.6 ± 0.6	57.0 ± 21.4	370 ± 30	170 ± 34	29.1 ± 0.7	6.3 ± 0.6

4. USS182, $z = 2.02$

   A strong emission line that we identify as Lyα at $z = 2.02$ is the only emission line visible in the HET spectrum. The line is asymmetric, has an integrated flux of 3.3×10^{-16} erg s^{-1} cm^{-2} and a broad FWHM of 1420 $\pm$ 30 km s^{-1}. The spatial extent of the Lyα emission from IFU data is calculated to be 29.5×18.8 kpc. The host galaxy is detected with a magnitude of $K = 21.8 \pm 0.2$ AB.

5. USS18, $z = 2.06$

   Similar to USS182, only a strong Lyα emission line at $z = 2.06$ is identified in the spectrum. The line also appears to be asymmetric, has a an integrated flux of $7.8 \times 1-^{-16}$ erg s^{-1} cm^{-2} and a FWHM of 950 ± 60 km s^{-1}. The spatial extent of the Lyα emission is 32.0×22.6 kpc.

6. USS320, $z = 2.20$

   The double-peaked Lyα emission line was identified at a redshift of $z = 2.20$. The Lyα emission seems to be extended in the 2D spectrum. There are also hints of very faint C IV emission, C II], Ne IV and possible Mg II (although in sky lines) emission in the redder parts of the spectrum at the same redshift. We smooth the double-peaked Lyα emission line and fit with a single Gaussian. We derive a line flux of 2.79×10^{-17} erg s^{-1} cm^{-2} and a FWHM of 1980 km s^{-1}. The host galaxy is detected with a magnitude of $K = 21.7 \pm 0.3$ AB.

7. USS268, $z = 2.35$

   Spatially resolved double peaked Lyα emission detected, with a strong HI absorption feature at $z = 2.35$. Also detected in the redder parts of the spectrum is C II] and Mg II (although this is again in sky lines) at the same redshift. We again smooth the Lyα line and fit with a single Gaussian to calculate a line flux of 7.33×10^{-17} erg s^{-1} cm $^{-2}$ and FWHM of 1981 km s^{-1}. The host galaxy is detected with $J = 23.6 \pm 0.1$ AB and $K = 21.9 \pm 0.3$ AB.

8. USS98, $z = 2.61$

   A single, strong Lyα emission line at a redshift of $z = 2.61$ is detected in the blue arm. The line appears to be asymmetric. There is no clear emission line in the redder parts, as most of the expected lines are contaminated by sky lines. Gaussian fit to the emission line gives a line flux of 5.91×10^{-17} erg s^{-1} cm^{-2} and a narrower FWHM of 810 km s^{-1}.

9. USS172, $z = 4.11$

   A single emission line is detected in the spectrum, which we identify with Lyα at $z = 4.106$. The line is faint, with an integrated flux of 5.2×10^{-17} erg s^{-1} cm^{-2} and has a relatively narrow FWHM of 570 ± 30 km s^{-1}. No other emission line is detected in either the blue or the red channels of the spectrograph. The spatial extent of the Lyα emission is relatively compact, at 13.3×9.5 kpc. The host galaxy is detected at NIR wavelengths with $J = 22.8 \pm 0.1$ AB and $K = 22.7 \pm 0.2$ AB.

10. USS188, $z = 4.57$

    A single, weak emission line identified as Lyα at $z = 4.57$ is detected in the spectrum. The integrated line flux is 6.8×10^{-17} erg s^{-1} cm^{-2} with a relatively narrow FWHM of 520 ± 20 km s^{-1}. Near infrared photometry of the host galaxy shows that it is undetected down to a 3σ depth of $J > 23.4$ AB, but is detected with $K = 21.6 \pm 0.2$ AB, where expected contanimation from the [O II] λ3727 eimssion line may be present.

11. USS43, $z = 4.86$

    We detect a single emission line for this source too, which is identified as Lyα at $z = 4.86$. The line is asymmetric and has an integrated flux of 5.1 ± 0.8 erg s^{-1} cm^{-2} and a narrow FWHM of 500 ± 30 km s^{-1}. At this redshift, USS43 is one of the highest redshift radio galaxies currently known. No other line is detected in the spectrum to confirm the redshift, though. Near-infrared photometry is also currently not available for this source.

12. USS202, $z = 5.72$

    A single emission line, characteristic of Lyα at high redshifts is detected in the spectrum of this object, giving a redshift of $z = 5.72$. This makes it the highest redshift radio galaxy observed to date. A detailed analysis of the emission line in this particular source is presented separately in Saxena et al. (2018c).

Undetected sources

There remain 11 USS sources that were targeted for spectroscopy and no emission lines were detected. From these, two sourcrs had continuum detections but no emission lines, implying a possible low redshift. These sources could either lie in the redshift range where the bright optical emission lines are hard to observe from ground based telescopes ($1 < z < 2$) or just lack strong emission lines in their

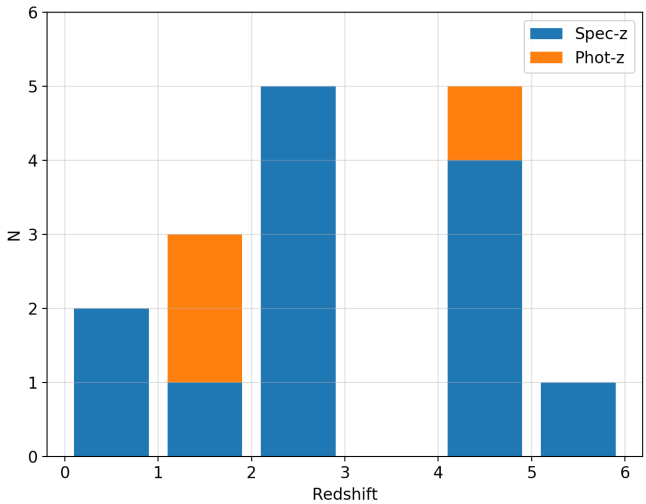

Figure 5.3: Distribution of spectroscopic redshifts (blue), with photometric redshifts (orange) stacked on top, giving the total number of sources in each redshift bin in the original Saxena et al. (2018a) sample. The distribution shows that the USS selection is effective at picking out high-redshift radio galaxies from a large area radio survey.

spectra. For sources with no line or continuum detections, it may be possible that the emission lines are broad and therefore, missed by our relatively shallow spectroscopic observations. The non-detections could also indicate that these sources are either (optically) faint low mass radio galaxies, or lie at very high redshifts (De Breuck et al. 2001).

5.2.4 Properties of the faint radio galaxy sample

Redshift distribution

In this section we look at the redshift distribution of the spectroscopically confirmed radio sources. Out of a total of 32 sources that were initially compiled by Saxena et al. (2018a), we spectroscopically confirmed redshifts for 12 of them. Figure 5.3 shows the distribution of these redshifts, along with photometric redshifts for three additional objects in the sample reported by Saxena et al. (2018a), which pushes the total number of sources with redshifts to 15. The spectroscopic redshift distribution peaks at $2 < z < 3$, with the total range of redshifts between $0.52 < z < 5.72$. This includes the recent discovery of the highest redshift radio galaxy discovered at $z = 5.72$, which was reported separately in Saxena et al. (2018c). The detection of a fair amount of $z > 2$ radio galaxies, through USS selection combined with optical faintness and compact radio sizes, is holds promise for similar studies in the future with even deeper radio surveys, such as the LOFAR Two-meter Sky Survey (Shimwell et al. 2017; Shibuya et al. 2018).

Velocity dispersion

For radio sources spectroscopically confirmed in this study, through [O II], [O III] and Mg II lines at low redshifts and the Lyα line at high redshifts ($z > 2$), the full width at half maximum (FWHM) of the emission lines is in the range $320 - 1420$ km s^{-1}. This range is lower than what is typically observed for much brighter radio galaxies across all redshifts (see De Breuck et al. 2000a, for example) and in the following sections we compare the line widths with radio galaxies in the literature.

Stellar masses

We now estimate stellar masses for 8 (out of the 12 spectroscopically confirmed) new radio galaxies that were observed in K band. To do this, we first model the expected K band magnitudes for radio galaxies with different stellar masses across redshifts using the PYTHON package called SMPY (Duncan & Conselice 2015). SMPY is a stellar population modelling code designed for building composite stellar populations in an easy and flexible manner and allows for synthetic photometry to be produced for single or large suites of stellar population models. To build stellar populations, we use the Bruzual & Charlot (2003) model with a Chabrier (2003) initial mass function (IMF). We assume solar metallicity, similar to Willott et al. (2003), a formation redshift of $z_f = 25$ and a maximally old stellar population that has been forming stars at a constant rate. We follow the Calzetti et al. (2000) law for dust attenuation, using $A_v = 0.15$, in line with observations and predictions from McLure et al. (2018) and Cullen et al. (2018) at the redshifts and mass bins that are typical of radio galaxy hosts ($M_\star > 10^{10.5}\ M_\odot$). The synthetic photometry produced for stellar masses in range $10.6 < \log M_\star < 12.0$ is then convolved with the K band filter to calculate apparent K band magnitudes over a redshift range $0 < z < 7$. The individual stellar mass is determined by finding the best fit stellar mass track to the K band magnitude and redshift using chi-squared minimisation.

The NIR photometry for faint radio galaxies and stellar masses inferred from the models are shown in Table 5.4. The fainter radio galaxies have lower stellar masses on average when compared to the bright radio galaxies known in the literature. The $10^{12}\ M_\odot$ stellar mass limit predicted for radio galaxies by Rocca-Volmerange et al. (2004) stands even for our sample – there is no radio source

Table 5.4: Near infrared photometry for HzRGs and stellar mass measurements for radio galaxies in our sample.

Source ID	z	J (AB)	K (AB)	log $M_\star$ ($M_\odot$)
USS43	1.46	–	21.6 ± 0.2	10.8 ± 0.4
USS182	2.02	–	21.8 ± 0.2	11.0 ± 0.4
USS320	2.20	–	21.7 ± 0.3	11.2 ± 0.4
USS268	2.35	23.6 ± 0.1	21.9 ± 0.3	11.2 ± 0.5
USS172	4.11	22.8 ± 0.1	22.7 ± 0.2	11.2 ± 0.5
USS188	4.57	> 23.4	$21.6 \pm 0.2^\star$	11.7 ± 0.5
USS202	5.72	> 25.3	> 24.2	< 10.7

*Expected contamination from [O II] $\lambda3727$ emission line in the K band.

with an inferred stellar mass higher than 10^{12} $M_\odot$ in our sample. Overall, we find that fainter radio galaxies occupy the massive end of the stellar mass function at all redshifts, in line with previous observations that showed that radio galaxies are hosted by massive galaxies at every epoch (Rocca-Volmerange et al. 2004).

The highest redshift radio galaxy, TGSS J1530+1049 at $z = 5.72$, which was part of our sample and was presented in Saxena et al. (2018c) is one of the lowest stellar mass radio galaxy from our sample. It is important to remember, however, that the overall lower stellar masses of galaxies in our sample are obtained under the assumptions that go into the stellar population modelling mentioned earlier. The biggest uncertainty comes from the assumption of dust attenuation, $A_v = 0.15$. It may be possible that radio galaxy hosts are dustier, which would lead to a higher stellar mass than what we report. However, since our models are able to account for the scatter in the $K - z$ relation for known radio galaxies without requiring extremely large or extremely small stellar masses, the inferred stellar masses for galaxies in our sample seem to be in line with expectations.

5.3 Comparison with literature HzRG sample

In this section we compile a sample of known high-redshift radio galaxies ($z \geqslant 2$) from the literature to compare the sample of newly discovered faint HzRGs against. We begin by briefly describing the parent radio samples from which the literature $z > 2$ radio galaxies were selected. We particularly highlight the flux limits of each of these radio samples and note that a large majority of these radio samples have much higher flux density limits than the Saxena et al. (2018a) sample used in this study. We point the readers to the relevant references mentioned in the sample description for detailed information about the sources.

5.3.1 Literature samples

Röttgering et al. 1997

This sample contains spectroscopic follow-up of the Leiden ultra-steep spectrum (USS) sample (Röttgering et al. 1994) and the 4C USS sample Tielens et al. (1979). Röttgering et al. (1997) sample contains spectra for 64 radio galaxies, with 29 of them being at $z > 2$. Other Lyα properties from this sample are presented in van Ojik et al. (1997). The median radio flux density of these sources is in the range $1 - 2$ Jy.

De Breuck et al. 2001

This spectroscopic sample of radio galaxies follows up the USS radio sources that were first presented in De Breuck et al. (2000a). The De Breuck et al. (2001) sample contains spectra for 69 radio galaxies from the De Breuck et al. (2000a) radio sample and observations of a few other previously known HzRGs, with 22 of them confirmed at $z > 2$. The limiting radio flux density for various subsamples observed in this study ranges from $250 - 1000$ mJy.

Jarvis et al. 2001

This sample contains spectra for radio sources selected from the 6C* sample (Blundell et al. 1998). The Jarvis et al. (2001a) sample has a total of 29 spectra, 12 of which lie at $z > 2$. The flux density at 151 MHz of sources in this sample is in the range $0.96 - 2$ Jy.

Willott et al. 2002

This sample contains optical spectroscopy for 49 radio sources selected from the 7C Redshift Survey, which is a spectroscopic survey of the regions covered in the 5C and 7C radio surveys. The Willott et al. (2002) sample contains 5 radio galaxies at $z > 2$. The radio flux density probed by this sample is $S_{151} > 0.5$ Jy.

Bornacini et al. 2007

This sample contains spectra for 14 USS sources selected from the Westerbork in the Southern Hemisphere (WISH) catalogue (De Breuck et al. 2002) and subsamples from the De Breuck et al. (2000a) USS catalogue. Six out of 14 sources observed by Bornancini et al. (2007) lie at $z > 2$. The limiting flux density of the WISH sample is $S_{352} \sim 18$ mJy.

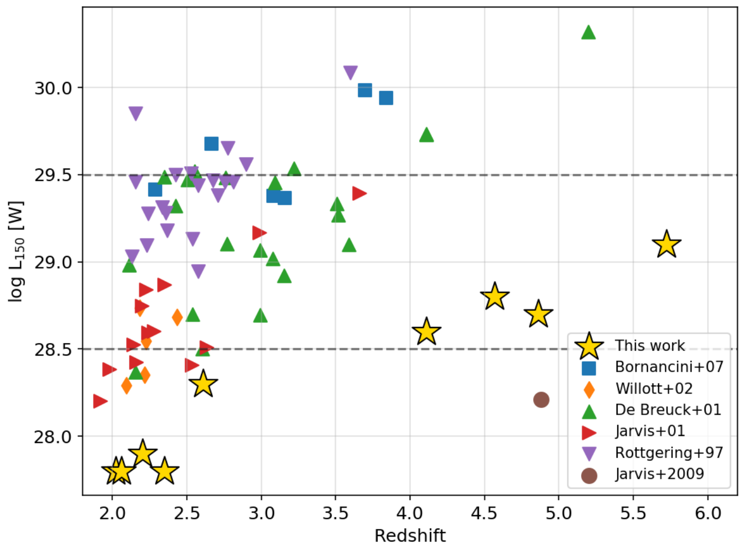

Figure 5.4: Radio luminosities scaled to an observing frequency of 150 MHz as a function of redshift for the extended HzRG sample, with the newly discovered HzRGs shown as gold stars. These new radio galaxies are almost an order of magnitude fainter at the highest redshift, opening up a new parameter space for the discovery and study of radio galaxies at high redshifts. Also shown as dashed black lines are the luminosity bins that are used for further analysis in this paper.

Radio luminosities

The extended HzRG sample consists of a total of 75 radio galaxies at $z \geqslant 2$. All these radio galaxies have Lyα line measurements. We calculate the radio luminosities, radio sizes and Lyα luminosities for the literature HzRGs using the updated cosmology used in this study. Specifically for the radio luminosities at a frequency of 150 MHz, we use the published flux density at 150 MHz wherever available and when needed, we scale their flux density to 150 MHz using the published spectral index. For the newly spectroscopically confimed radio galaxies reported in this paper, we use the radio measurements from Saxena et al. (2018a) to calculate radio luminosities.

The distribution of radio luminosities as a function of redshift is shown in Figure 5.4. Our sample of newly confirmed faint HzRGs is marked with gold stars (and in all the following sections). It is immediately clear that our sample probes radio luminosities almost and order of magnitude fainter at the highest redshifts. This includes the discovery of the highest redshift radio galaxy known till date, TGSS J1530+1049 (Saxena et al. 2018c). We also show the faint radio galaxy detected by Jarvis et al. (2009), which was detected in a deep field and not from an all-sky survey, as an example of the kind of sensitivites that future radio surveys would be able to achieve to probe even fainter radio galaxies at high redshifts.

5.3.2 Comparison of emission line and radio properties

In this section we will explore how the emission line and radio properties of faint HzRGs compare with those of the literature HzRG sample.

Lyα luminosities and FWHM

We begin our analysis by first showing the distribution of Lyα line luminosities and FWHM values for faint HzRGs (gold stars) and literature HzRGs (black circles) across all redshifts in Figure 5.5. We note that the faint HzRGs in our sample show a systematically lower Lyα luminosity and FWHM compared to other HzRGs in the literature. The faint HzRG sample has a median Lyα luminosity of log $L_{Ly\alpha} = 43.0$ erg s^{-1} , with 1σ standard deviation of 0.2 erg s^{-1} . The literature HzRG sample has a median Lyα luminosity of log $L_{Ly\alpha} = 43.5$ erg s^{-1} but a much larger 1σ standard deviation of 0.7 erg s^{-1} . The difference in median FWHM values between the two samples is considerably large, with faint HzRGs having median and standard deviation of 750 ± 350 (1σ) km s^{-1}, and the literature HzRGs having median and standard deviation of 1475 ± 800 km s^{-1}.

In Figure 5.6 we plot the Lyα luminosities with redshift for both faint and literature samples. The higher dispersion in the literature sample is seen across all

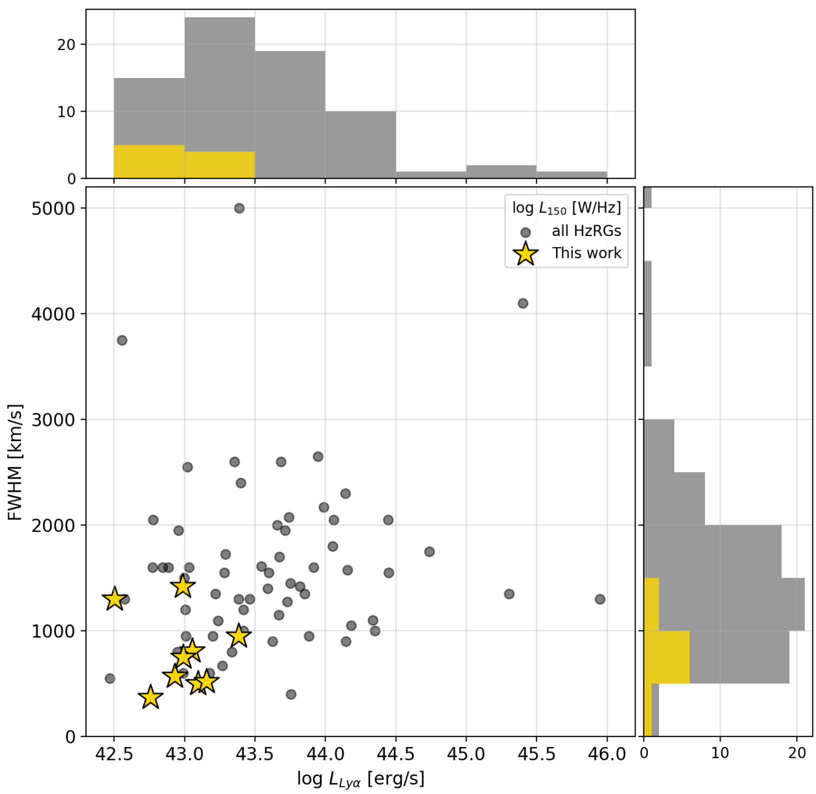

Figure 5.5: Distribution of Lyα luminosities and FWHM for faint (gold stars) and literature (black circles) radio galaxies. Also shown are the histograms of both these samples. Clearly, the faint HzRGs have lower Lyα luminosities and FWHM. In the text we give the median and standard deviations of Lyα luminosities and FWHM in the two samples. There is no correlation observed between the Lyα luminosities and FWHM for either of the two samples.

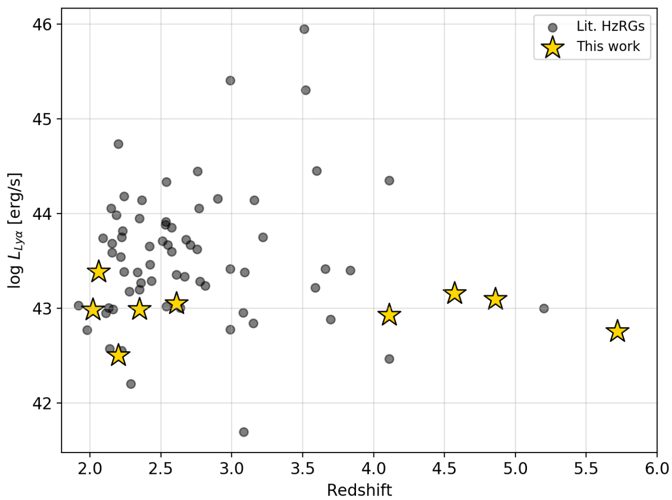

Figure 5.6: Lyα line luminosities as a function of redshift for the faint and literature HzRG samples. Across all redshifts, the faint HzRGs show lower luminosity values. We do not see any evolution in the line luminosity with redshift for either of the two HzRG samples.

redshifts, with a handful of sources at $z \sim 3 - 3.5$ showing significant deviations ($2.5 - 3\sigma$) from the median, such as WN J1053+5424 at $z = 3.1$ exhibiting the weakest Lyα luminosity of the sample ($\log L_{Ly\alpha} = 41.7$ erg s^{-1}) and TN J0205+2242 at $z = 3.5$ having the strongest luminosity ($\log L_{Ly\alpha} = 45.9$ erg s^{-1}). The faint HzRGs have comparable Lyα luminosities across redshifts. Overall, the luminosities (both faint and literature) do not seem to evolve much with redshift, with the Pearson's correlation coefficient $r = -0.02$ suggesting little to no evolution.

Next, we plot the Lyα line widths (FWHM) as a function of redshift for both faint and literature HzRG samples in Figure 5.7. We find a negative correlation between FWHM and redshift for both samples and the anti-correlation is stronger in the faint sample ($r = -0.85$, compared to $r = -0.12$ for the literature sample). From the literature sample, there are 3 radio galaxies at $z \sim 2 - 3$ that are 3σ outliers from the median value, with the radio galaxy 1113$-$178 from Röttgering et al. (1997) showing the broadest Lyα profile with FWHM = 5000 km s^{-1}. The broadest line widths observed at $z \sim 2 - 3$ correspond with the epoch of the peak of AGN activity, due to peaks in both the AGN luminosity density (Fanidakis et al. 2012, and references therein) and the central supermassive black hole growth rate

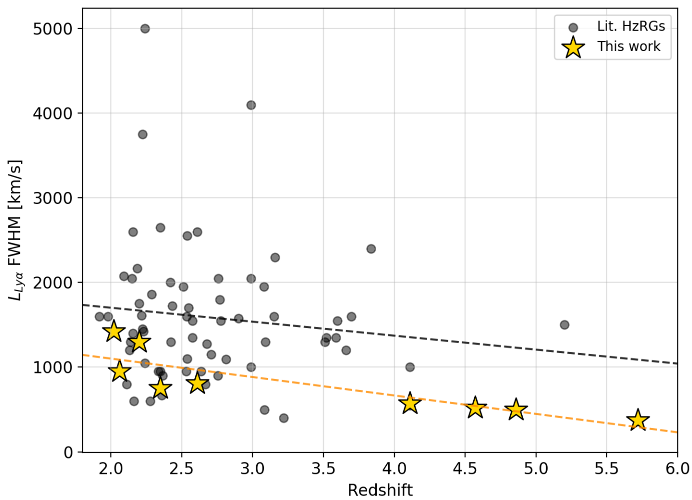

Figure 5.7: The Lyα FWHM as a function of redshift for the faint and literature HzRGs. Across all redshifts, faint HzRGs exhibit lower FWHM values when compared to the literature HzRGs. We see a decrease in FWHM with redshift in both samples, but the anticorrelation is stronger for faint HzRGs (orange dashed line) than the bright ones (black dashed line).

as a function of redshift (Shankar et al. 2009, and references therein).

Radio luminosity vs. Lyα luminosity

We now show Lyα line luminosities as a function of radio luminosity at 150 MHz for the faint and literature samples in Figure 5.8. We see a weak positive correlation in the literature sample, with $r = 0.06$, which is weaker than what Jarvis et al. (2001a) observed for their sample of radio galaxies. Conversely, in the faint HzRG sample we see a weak negative correlation, with $r = -0.08$. Both these r-values are consistent with little to no correlation between the two quantities, indicating that the radio luminosity (across several orders of magnitude) of a radio galaxy does not have much influence on its Lyα luminosity.

Linear sizes

In this section, we look at the linear size distribution of radio galaxies both samples. For faint HzRGs presented in this paper, we use the angular sizes reported by Saxena et al. (2018a). Sizes of literature galaxies were calculated using the updated cosmology used in this study. The median size of our faint radio sources is

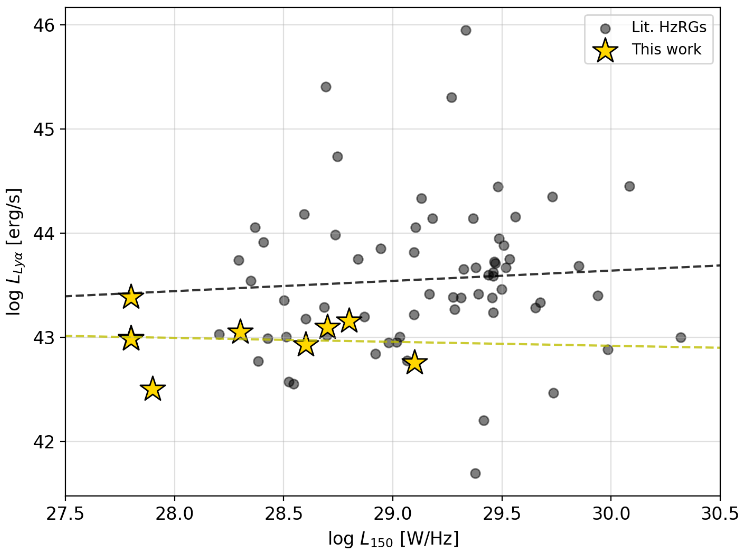

Figure 5.8: Lyα luminosities as a function of radio luminosity at 150 MHz for faint and literature HzRGs. There is a positive correlation observed between the two quantities for literature HzRGs, however it is weaker than what some previous studies have found. However, we do not see any correlation between the two for faint HzRGs.

22 kpc and the median size of the literature HzRGs is 42 kpc. It is important to remember that Saxena et al. (2018c) introduced an angular size restriction ($< 10''$) while selecting faint HzRG candidates, which would preferentially select compact radio sources across all redshifts.

We show the distribution of radio luminosities at 150 MHz as a function of linear size for both the faint and the literature HzRGs in Figure 5.9. These so-called '$P - D$' diagrams have long been used to characterise the growth and evolution of powerful radio sources across all redshifts (Kaiser et al. 1997; Blundell et al. 1999; Saxena et al. 2017). The $P - D$ tracks essentially trace the evolutionary path that a radio source takes through its lifetime. For a given jet power, radio sources start out at the left side of the $P - D$ diagram. As radio sources grow, they lose energy, initially through adiabatic losses and at larger sizes due to inverse Compton losses because of interactions with the cosmic microwave background radiation (Kaiser & Best 2007). Overall, this results in the radio sources experiencing decreasing radio luminosities with increasing linear sizes, moving them towards the bottom-right side of the $P - D$ diagram. The $P - D$ tracks are influenced by magnetic field strength, redshift and the radio source environment. Different jet powers also give rise to different $P - D$ tracks (Kaiser et al. 1997).

As seen in Figure 5.9, the faint HzRGs lie in the part of the $P - D$ diagram corresponding to weaker and younger radio sources. We also note that the largest radio sources are also some of the most luminous ones and larger radio sources are expected to be older than the compact ones. Radio sources with intrinsically weaker jets are unable to grow out to large sizes as they are unable to overcome the increasing energy losses with increase in linear size, and are eventually extinguished before ever achieving large sizes (Saxena et al. 2017). This is evident from the lack of sources in the bottom-right part of the $P - D$ diagram. We discuss the redshift evolution of linear sizes of both the faint and literature samples in Section 4.4.

Radio spectral index vs. redshift

We now explore the observed correlation between the low-frequency radio spectral index (α) and redshift (z) in our extended HzRG sample in Figure 5.10. The $z - \alpha$ correlation for radio galaxies has often been used to identify HzRG candidates in large area radio surveys (see Röttgering et al. 1997, for example).

We observe a correlation between redshift and spectral index in the brighter radio galaxies from the literature. However, it is important to note that most of the radio galaxies that are part of the extended sample were initially selected because of their ultra-steep spectra (USS) at low radio frequencies ($\alpha < -1$), which could potentially bias the distribution and lead to the recovered correlation. From

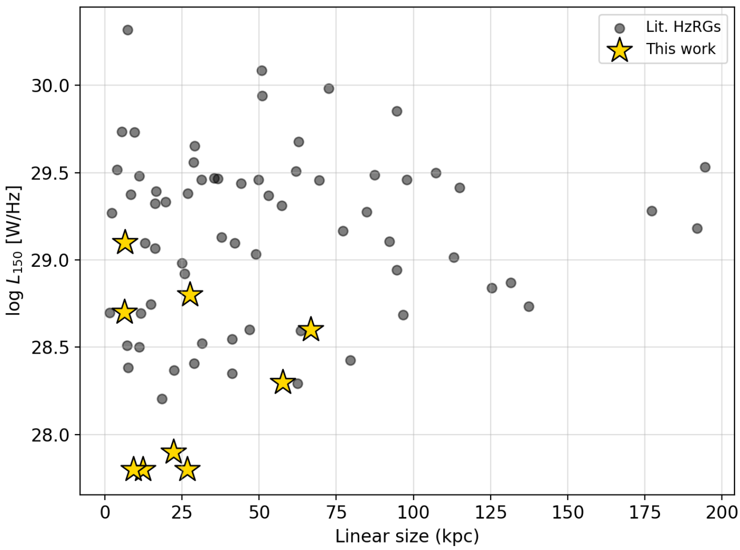

Figure 5.9: The distribution of radio luminosities at 150 MHz and linear sizes of sources in the faint and literature samples. the $P-D$ diagram tracks the evolution of radio sources through their lifetime. Clearly, The most luminous sources are able to grow out to larger sizes as their intrinsically more powerful jets work against the energy loss mecahanisms that begin to dominate later in the radio source life. The faint HzRGs preferentially lie towards the low power, small size part of the plot, indicating that they must be young.

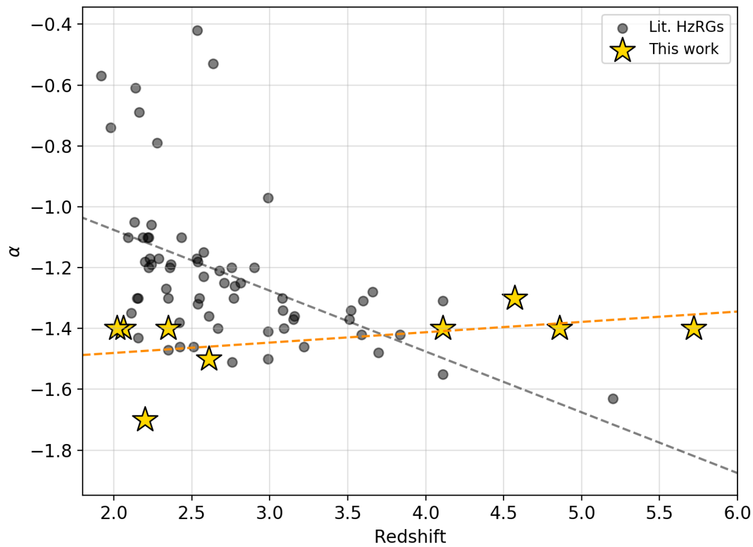

Figure 5.10: Low-frequency radio spectral index as a function of redshift for both faint and literature HzRGs. We observe an anticorrelation between z and α for the literature sample, which has been used successfully to select promising HzRG candidates from large radio surveys. However, the faint HzRGs actually show a positive correlation between the two. Since most of the HzRGs presented in this study were initially selected because of their spectra, the observed correlations are likely to contain several biases.

our sample of faint galaxies, however, we do not see a strong correlation between spectral index and redshift. In fact, the faint radio galaxies exhibit a positive correlation between α and z, in contrast to what is seen for literature HzRGs. Further, we do not find extremely steep spectral indices at the highest redshifts, even though the best-fit suggests a strong correlation.

The origin of the observed $z - \alpha$ correlation was investigated by Morabito & Harwood (2018), where they found that a combination of inverse Compton losses at high redshifts and selection effects were able to explain the observed $z - \alpha$ correlation in radio galaxies. Inverse Compton losses affect the high frequency parts of the radio SED, which results in an overall steeper spectral index when measured at low-frequencies. Inverse Compton losses are also expected to affect the linear sizes of radio sources. However, we do not find any strong correlation between the spectral index and linear sizes of radio sources in either of the two samples studied.

5.4 Discussion

5.4.1 Lyα emission in faint HzRGs is powered by weak AGN

As shown in Figure 5.5, our newly discovered faint radio galaxies have lower Lyα luminosities and FWHM values across all redshifts. The dispersion in their Lyα luminosities is also low. This is interesting because the distribution of Lyα luminosities and FWHM for brighter HzRGs shows a much larger variety (3σ dispersion of log $L_{Ly\alpha} = 2.1$ erg s^{-1} , as opposed to 0.6 erg s^{-1} for the faint radio galaxies, as shown in Section 5.3.2). Historically, the large luminosities and equivalent widths of Lyα emission from bright HzRGs have been explained by anisotropic photoionisation from an obscured AGN in combination with jet-induced shock ionisation or contribution from hot stars (Chambers et al. 1990; Baum et al. 1992; McCarthy 1993; van Ojik et al. 1996, 1997; De Breuck et al. 2000b). Additionally, physical phenomena such as launching of winds and outflows from the central AGN (see Nesvadba et al. 2008, for example), bursts of star formation and radio AGN activity driven by recent mergers (see Villar-Martín et al. 2007b, for example) and gas infall on to the host galaxy (see Villar-Martín et al. 2007a, for example) are sometimes required to explain the UV line ratios and large velocity dispersions at high redshifts.

The systematically lower Lyα luminosities in faint HzRGs indicate that the line emission must be ionised by a weaker AGN, or by modest star-burst activity. To accurately disentangle the relative contributions from AGN and star-formation, rest-frame optical nebular emission lines are needed to then use the BPT diagram

(Baldwin et al. 1981). Lyα alone can not be used to make clear distinctions between the underlying ionising sources.

5.4.2 No direct evidence of strong interaction between radio jet and line-emitting gas

Another indication of the absence of shocks is the lack of evidence for strong jet-gas interaction – we do not see an anti-correlation between Lyα FWHM and linear size, which has previously been interpreted as a signature of jet-gas interaction in radio galaxies (van Ojik et al. 1997; Baum & McCarthy 2000; Best et al. 2000). The origin of this anti-correlation has been attributed to jets in smaller radio sources still being in the process of traversing the relatively dense interstellar medium of their host galaxies, which leads to transfer of kinetic energy from the jets to the line emitting gas, resulting in larger line widths (see van Ojik et al. 1997, for example). For larger radio sources, when the jet has passed well beyond the emission line regions, the emission line widths are narrower indicating that the gas has more relaxed and settled kinematics.

In fact, when combining the faint and literature HzRG samples, it is clear that even though some of the largest radio sources in our sample show narrower Lyα line widths, we can not conclusively infer that narrow line widths are a consequence of less jet-gas interaction, as shown in Figure 5.11 in which the faint HzRGs are marked with gold stars and literature HzRGs with black circles. The median linear sizes in the combined sample were calculated in bins of Lyα FWHM. These FWHM bins are $0 - 1000$, $1000 - 2000$, $2000 - 3000$ and > 3000 km s^{-1}. Therefore, from our data we can not conclusively pin-point the dominant impact of jet-gas interactions in smaller radio sources. However, the added complexity of probing radio sources across a broad range of radio and Lyα luminosities as well as redshifts in our sample may dilute out any strong effects that may be seen in subsets of relatively similar radio galaxies.

5.4.3 Faint HzRGs have lower stellar masses

As shown earlier, the apparent K-band magnitudes for a subset of faint radio galaxies presented in this paper were lower than what has been observed for more powerful radio sources across all redshifts. Using simple stellar population modelling, we find that the stellar masses inferred for faint HzRGs are also lower than what has been typically determined for bright HzRGs (see Rocca-Volmerange et al. 2004, for example). This is shown in Figure 5.12, where we show apparent magnitudes for our faint HzRGs along with those from HzRGs in the literature.

Also shown are predictions for apparent K magnitude from our stellar popula-

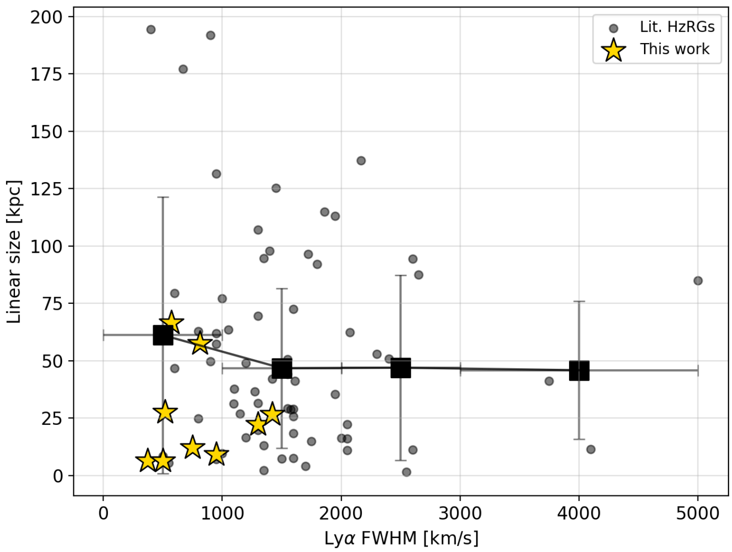

Figure 5.11: The linear sizes of faint HzRGs (gold stars) are not seen to anticorrelate with Lyα FWHM, which is indicative of absence of strong jet-gas interaction. This implies that shocks do not play a strong role in powering the Lyα emission in faint HzRGs. The anticorrelation in the combined sample of faint and literature HzRGs, calculated by binning in FWHM, is also very weak (black squares), although we see that the largest literature HzRGS often also exhibit narrower FWHM.

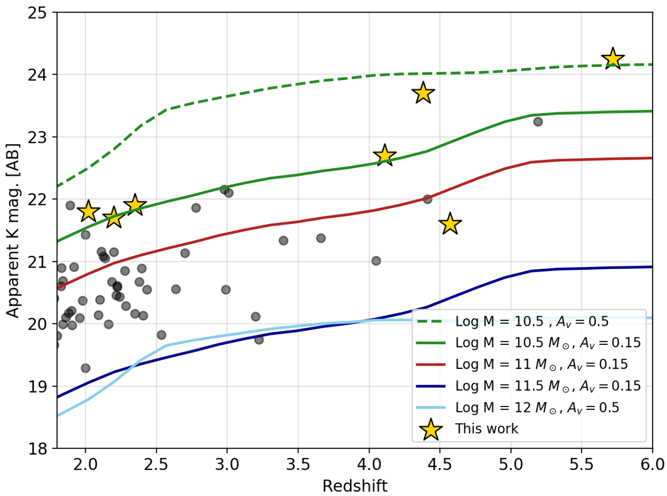

Figure 5.12: Apparent K band magnitudes and redshifts for faint HzRGs (gold stars) presented in this study. The solid lines indicate photometry obtained using simple stellar population modelling for different stellar masses. Also shown are radio galaxies with K magnitudes already in the literature (black circles), for comparison. The fainter radio galaxies studied in this paper have lower stellar masses when compared to the previously known, more powerful radio galaxies across all redshifts. The brightest galaxy in our faint HzRG sample has possible contamination from an emission line in the K band, which may lead to an overestimated stellar mass using simple models.

tion synthesis modelling. Our faint HzRGs lie closer to the lower mass tracks, with the exception of USS188 with a stellar mass of $M_\star = 10^{11.7\pm0.7}\ M_\odot$. However, contamination from the [O II] $\lambda3727$ emission line is expected in the K band and it is therefore likely that the stellar mass for this galaxy is being overestimated. The stellar mass estimates presented in this paper are based on only the K band magnitudes and photometry in additional bands and more detailed stellar population modelling is required to accurately measure stellar masses for our sample of faint HzRGs.

5.4.4 Are faint HzRG hosts rapidly assembling their stellar mass?

As shown earlier, the faint HzRGs reported in this paper show weaker Lyα luminosities and narrower line widths in comparison to the brighter HzRGs. The host galaxies of these faint radio sources are also less massive than the hosts of brighter radio galaxies. Questions naturally arise about the nature of the galaxies that host weak radio sources at high redshifts. In this section we attempt to provide some qualitative constraints on this.

When comparing the line luminosities and widths of the radio galaxies presented in this study with 'non-radio' Lyα emitters (LAEs) with high equivalent widths (EW), such as the eight LAEs in the redshift range $3.8 - 4.4$ studied by Saito et al. (2008), an interesting trend emerges. In Figure 5.13 we show the Lyα luminosities plotted against line widths for the extended HzRG sample and the faint HzRGs reported in this paper, along with the high EW (>240 Å) LAEs from Saito et al. (2008). Clearly, the literature HzRGs (black dots) show a large scatter in both Lyα luminosity and FWHM values. The distribution for faint HzRGs (gold stars) and high EW LAEs (red diamonds) are much tighter. Saito et al. (2008) rule out the presence of 'superwinds' launched by bursts of star formation and ionisation by a central AGN for their sample of LAEs. Owing to the observed tight positive correlation between the line luminosities and widths, Saito et al. (2008) conclude that the origin of line emission in these galaxies is most likely due to cold accretion and that these LAEs are in an early phase of their evolution.

In Figure 5.13 we note that our faint HzRGs form a 'bridge' between supposedly cold accreting LAEs and the AGN-dominated bright HzRGs currently known in the literature. Further, faint radio galaxies show a positive correlation between Lyα luminosity and line width, in line with what was observed by Saito et al. (2008). As shown in Section 5.4.1, the faint HzRGs are most likely ionised by weaker AGN. This means that the contribution from the AGN towards the Lyα emission would be low. Under this assumption, we may infer from the positive correlation between Lyα luminosity and FWHM observed for a majority of faint HzRGs that they are in an early stage of their evolution and are actively accreting cold material from their surroundings, similar to high EW LAEs from Saito et al. (2008). This is consistent with the lower stellar masses inferred for the host galaxies of faint radio sources across redshifts.

The suggestion that faint radio galaxies at high redshifts are actively building up their stellar mass is not entirely implausible, since faint radio galaxies at the highest redshifts are expected to be young (see Blundell et al. 1999, for example). Recent VLBI radio observation of TGSS J1530+1049, a radio galaxy at $z = 5.72$, by Gabányi et al. (2018) revealed two distinct lobes separated by only $0.4''$, confirming that the radio source is young and that the host galaxy must be in a very early phase of its evolution.

5.4.5 Inverse Compton losses dominant at high redshift

Although there is no strong redshift evolution seen in the sizes of the faint HzRGs reported in this paper, we do observe an evolution of radio sizes with redshift of

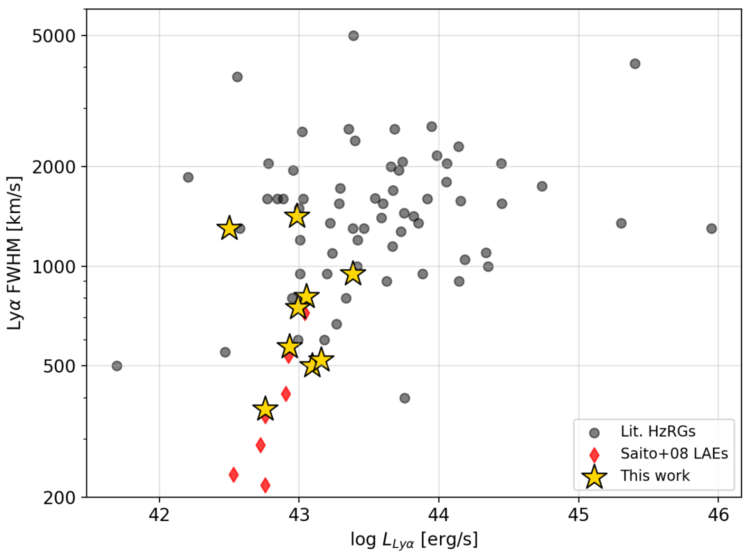

Figure 5.13: Lyα luminosity as a function of line width for faint (gold stars) and literature (black circles) HzRGs. Also shown are 'non-radio' Lyα emitting galaxies (LAEs) with high Lyα equivalent widths (EW $>$ 250 Å) from (Saito et al. 2008) (red diamonds). The faint HzRGs form a 'bridge' between the LAEs and the bright radio galaxies known in the literature, suggesting that fainter HzRGs are powered by weaker AGN. The relatively tight correlation between luminosity and FWHM for faint HzRGs also indicates that they may be actively accreting cold material from their surroundings like the Saito et al. (2008) LAEs.

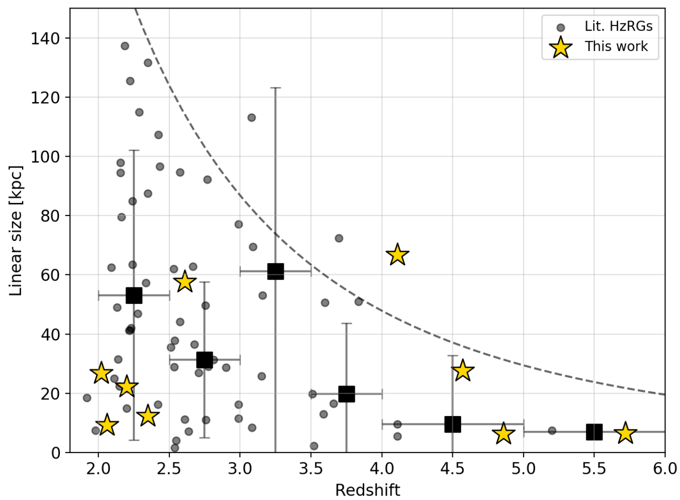

Figure 5.14: Linear sizes of HzRGs the faint (gold stars) and literature (black circles) samples with redshift. The median sizes, which are calculated by binning all radio sources in the combined HzRG sample in redshift bins, are shown as large black circles. Also shown are the predictions for redshift evolution of linear sizes due to inverse Compton losses, through interaction with the ambient cosmic microwave background radiation, from Saxena et al. (2017), that effectively provide an upper limit on achievable radio size. The median sizes of radio sources evolve strongly with redshift, and are well described by the Saxena et al. (2017) prediction, indicating that the dominant energy loss mechanism that shapes the size distribution of radio sources at high redshifts are inverse Compton losses.

literature radio galaxies. To gain better insights into the overall redshift evolution at $z > 2$, we combine the new faint and literature samples and bin the sources in redshift bins of $z < 2.5$, $2.5 - 3.0$, $3.0 - 3.5$, $3.5 - 4.0$, $4.0 - 5.0$ and $5.0 - 6.0$. The median linear sizes in each redshift bin as a function of redshift are shown in Figure 5.14. The error bars indicate the 1σ standard deviations in the redshift bins. In the highest redshift bin only two sources are present and therefore the small error bar is only indicative of ΔFWHM.

The strong evolution of radio sizes and the size distribution of individual sources are consistent with the prediction for the evolution of radio sizes with redshift from Saxena et al. (2017), where the decrease in radio size at high redshifts is primarily dominated by inverse Compton (IC) losses. This suggests that IC scattering is the dominant energy loss mechanism at high redshifts. The enhanced IC losses, due to an increasing energy density of the cosmic microwave background radiation at high redshifts, dominate over other energy loss mechanisms such as synchrotron or adiabatic losses (see Saxena et al. 2017, for example).

5.5 Summary

In this section we summarise the key findings of this paper. We have obtained spectroscopic redshifts for 12 out of the 32 sources that were selected for having an ultra-steep radio spectral index in the Saxena et al. (2018a) sample. These radio galaxies are almost an order of magnitude fainter than those that were previously discovered from large-area radio surveys and probe a new parameter space in low radio frequency flux densities. In addition to spectroscopy we have also obtained deep near-infrared imaging for a subset of the confirmed radio galaxies.

Next, we have compiled a sample of known $z > 2$ radio galaxies in the literature that have Lyα measurements. The literature HzRG sample was then used to compare the properties of our faint radio galaxies across redshifts. We explored the radio and optical properties of the both the faint and literature high-redshift radio galaxies The main conclusions of this study are as follows:

1. The newly confirmed fainter radio galaxies lie in the redshift range $0.52 \leqslant z \leqslant 5.72$, including the discovery of the highest redshift radio galaxy discovered till date, TGSS J1530+1049, which was first reported in Saxena et al. (2018c). The Lyα emission line profiles show a wide variety with FWHM values ranging from $320 - 1240$ km s^{-1}. The Lyα luminosities and FWHM are systematically lower than what has previously been observed for brighter radio galaxies at these redshifts. Due to fainter line luminosities, narrower line widths and no evidence of ionisation by shocks in the faint HzRGs, we conclude that Lyα emission in these galaxies is powered by weak AGN.

2. We use K band photometry for a subset of spectroscopically confirmed faint HzRGs presented in this paper to estimate stellar masses. Simple stellar population synthesis models are used for this. We find that the stellar masses to lie in the range $10.7 < \log M_\star < 11.7\ M_\odot$, which are lower than what is seen for brighter HzRGs in the literature. Therefore, fainter HzRGs are hosted by galaxies with lower stellar masses, which are also appear in a phase of building up their stellar mass rapidly.

3. Combined with the presence of weak AGN and lower stellar masses of faint radio galaxies across redshifts, we find that the hosts of fainter radio sources at high redshifts are in the process of assembling their stellar mass. This is also evident from the Lyα luminosities and FWHM of faint radio galaxies

following a correlation similar to those of high equivalent width, 'non-radio' Lyα emitting galaxies, whose line emission is powered by cold accretion of gas onto the galaxies.

4. The linear sizes of faint HzRGs do not evolve much with redshift, but the sizes of the literature HzRGs exhibit a decrease with increasing redshift. The redshift evolution of median sizes of sources in a combined sample of faint and literature HzRGs matches well with predictions for size evolution purely due to increased inverse Compton losses at high redshifts. Therefore, the dominant energy loss mechanism in radio galaxies at high redshifts is inverse Compton scattering due to interactions with the cosmic microwave background radiation, and not synchrotron or adiabatic losses.

There remain many radio sources from the original Saxena et al. (2018a) sample that still do not have a spectroscopic redshift and are high-priority targets for spectroscopy. Our new sample of HzRGs, that probes fainter flux densities over a large area on the sky, has offered glimpses into the nature of relatively less powerful radio galaxies at high redshifts. Ongoing large area surveys that are even more sensitive at low radio frequencies, such as the LOFAR Two-Meter Sky Survey (Shimwell et al. 2017) will uncover many more faint radio galaxies at high-redshifts, furthering our understanding of how radio galaxies are fuelled and their impact on their surroundings.

Acknowledgements

AS, HJR and KJD gratefully acknowledge support from the European Research Council under the European Unions Seventh Framework Programme (FP/2007-2013)/ERC Advanced Grant NEWCLUSTERS-321271. RAO and MM received support from CNPq (400738/2014-7, 309456/2016-9) and FAPERJ (202.876/2015). IP acknowledges funding from the INAF PRIN-SKA 2017 project 1.05.01.88.04 (FORECaST). PNB is grateful for support from STFC via grant ST/M001229/1.

This paper contains data from several different facilities. The William Herschel Telescope is operated on the island of La Palma by the Isaac Newton Group of Telescopes in the Spanish Observatorio del Roque de los Muchachos of the Instituto de Astrofísica de Canarias. The Hobby-Eberly Telescope (HET) is a joint project of the University of Texas at Austin, the Pennsylvania State University, Stanford University, Ludwig-Maximilians-Universität München, and Georg-August-Universität Göttingen. The HET is named in honor of its principal benefactors, William P. Hobby and Robert E. Eberly. The Gemini Observatory is operated by the Association of Universities for Research in Astronomy, Inc., under a cooperative agreement with the NSF on behalf of the Gemini partnership: the National Science Foundation (United States), the National Research Council (Canada), CONICYT (Chile), Ministerio de Ciencia, Tecnología e Innovación Productiva (Argentina), and Ministério da Ciência, Tecnologia e Inovação (Brazil). The Large Binocular Telescope (LBT), an international collaboration among institutions in the United States, Italy and Germany. LBT Corporation partners are: The University of Arizona on behalf of the Arizona university system; Istituto Nazionale di Astrofisica, Italy; LBT Beteiligungsgesellschaft, Germany, representing the Max-Planck Society, the Astrophysical Institute Potsdam, and Heidelberg University; The Ohio State University, and The Research Corporation, on behalf of The University of Notre Dame, University of Minnesota, and University of Virginia.

This work has made extensive use of ipython (Pérez & Granger 2007), astropy (Astropy Collaboration et al. 2013), aplpy (Robitaille & Bressert 2012), matplotlib (Hunter 2007b), mpdaf and topcat (Taylor 2005). This work would not have been possible without the countless hours put in by members of the open-source developing community all around the world.

5.A Long-slit spectra

Here we give the 1D spectra (observed frame) of all confirmed radio sources observed using three different facilities. The spectra are displayed with increasing redshift, and contain information about the source name, the redshift and the telescope used. Regions of strong skylines are marked by shaded boxes.

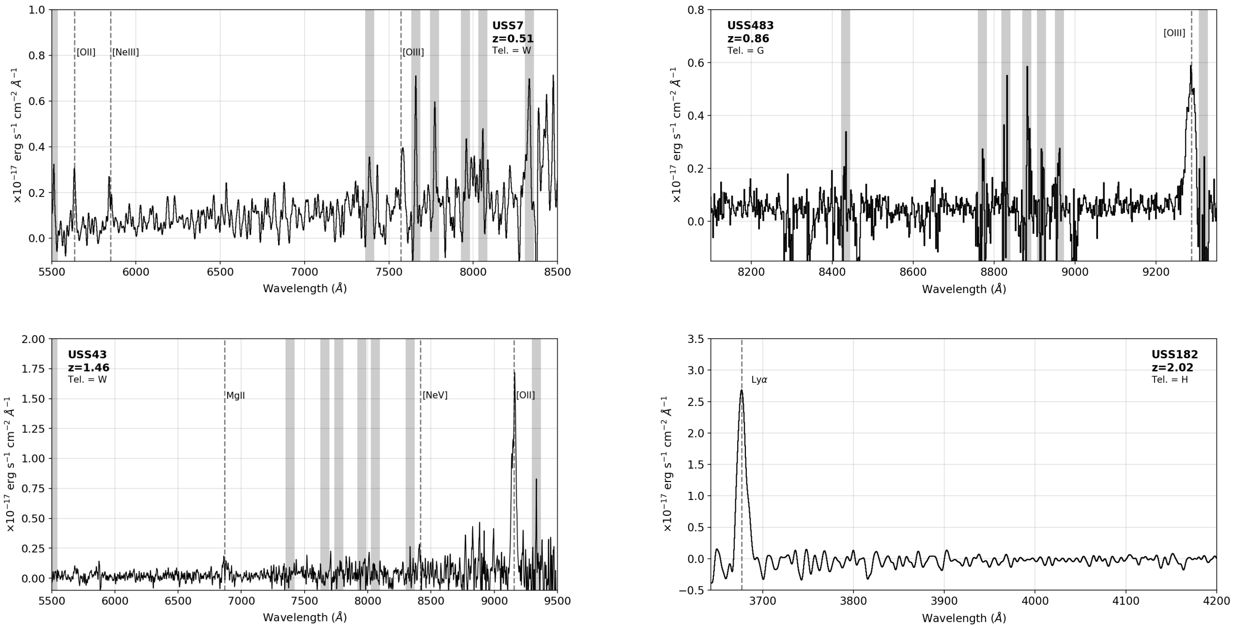

Figure 5.15: One dimensional spectra of all spectroscopically confirmed sources with the WHT, HET and Gemini. For clarity, we only show the relevant wavelength ranges for each spectrum. The shaded boxes indicate regions of strong contamination from atmospheric sky lines. Indicated in each spectrum is the, object name, redshift and telescope code (Tel.).

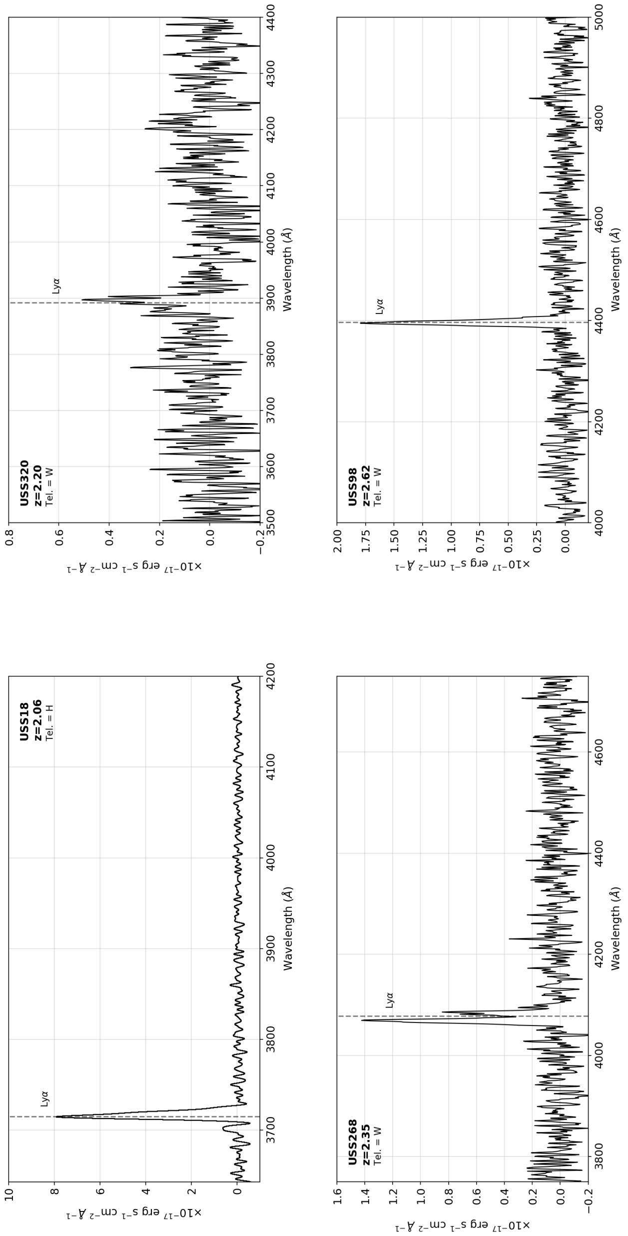
USS320
z=2.20
Tel. = W
USS98
z=2.62
Tel. = W
USS18
z=2.06
Tel. = H
USS268
z=2.35
Tel. = W
Lyα
Wavelength (Å)
×10⁻¹⁷ erg s⁻¹ cm⁻² Å⁻¹

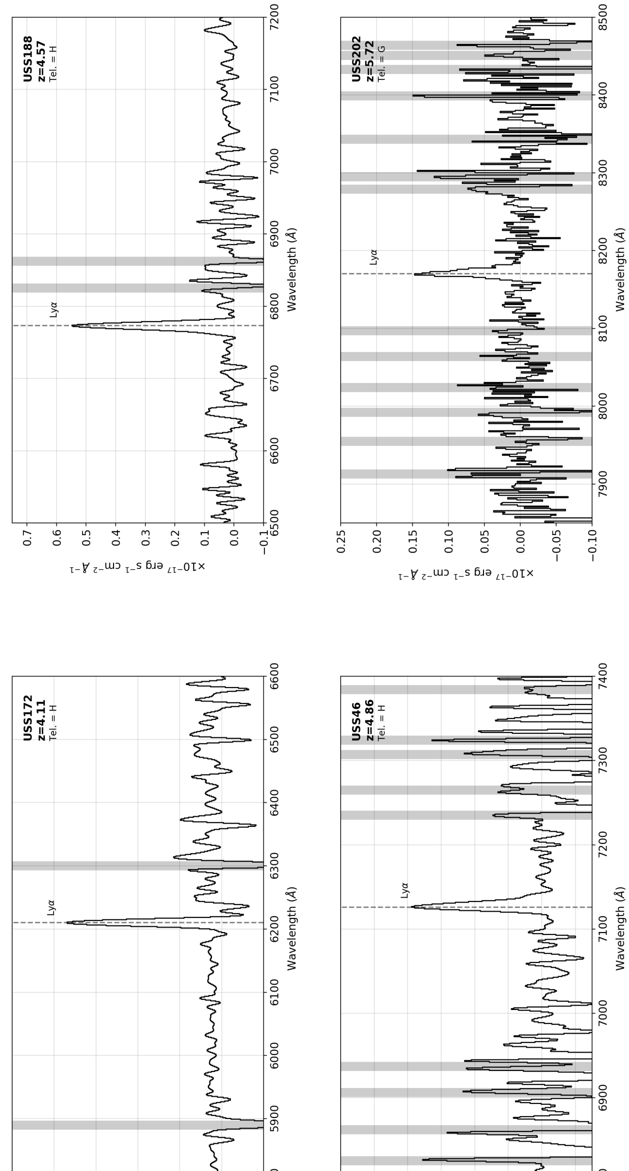
USS188
z=4.57
Tel. = H
USS202
z=5.72
Tel. = G
USS172
z=4.11
Tel. = H
USS46
z=4.86
Tel. = H
Lyα
Wavelength (Å)
×10⁻¹⁷ erg s⁻¹ cm⁻² Å⁻¹

5.B K-band images

Here we give the K band images for the subset of sources that were observed at NIR wavelengths. Overlain on top of the K band image are radio contours at 1.4 GHz from Saxena et al. (2018a). The contours shown begin at 0.25 mJy, which is on average $3.5 - 5\sigma$, and are a geometric progression of $\sqrt{2}$, such that the flux density increases by a factor of 2 for every two contours.

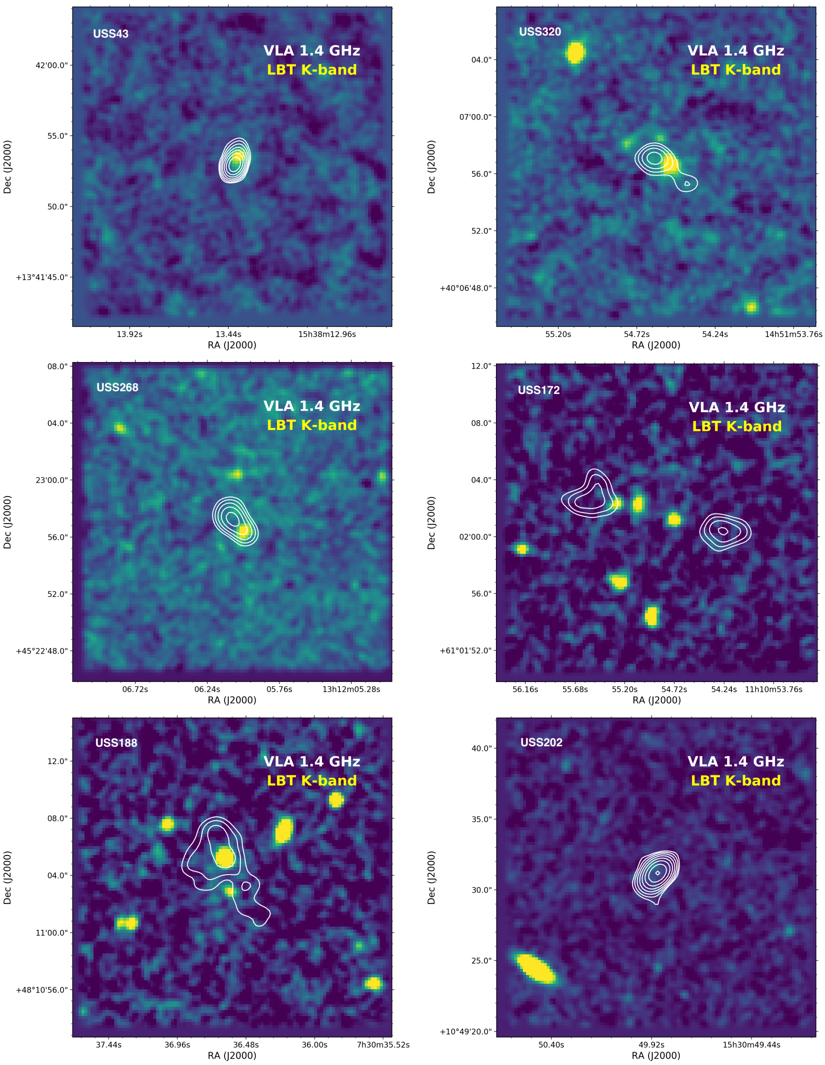

Figure 5.14: K-band image of the host galaxy of the radio source, with radio contours at 1.4 GHz from Saxena et al. (2018a) overlaid on top. The contours shown begin at 0.25 mJy, which is on average $3.5 - 5\sigma$, and are a geometric progression of $\sqrt{2}$, such that the flux density increases by a factor of 2 for every two contours.

Bibliography

Afonso J., et al., 2011, ApJ, 743, 122
Aihara H., et al., 2017, preprint, (arXiv:1702.08449)
Alam S., et al., 2015a, ApJS, 219, 12
Alam S., et al., 2015b, ApJS, 219, 12
Alexander P., 2000, MNRAS, 319, 8
Alexander P., 2002, MNRAS, 335, 610
Archibald E. N., Dunlop J. S., Hughes D. H., Rawlings S., Eales S. A., Ivison R. J., 2001, MNRAS, 323, 417
Astropy Collaboration et al., 2013, A&A, 558, A33
Bañados E., et al., 2015, ApJ, 804, 118
Baade W., Minkowski R., 1954, ApJ, 119, 206
Baldwin J. A., Phillips M. M., Terlevich R., 1981, PASP, 93, 5
Barthel P. D., Miley G. K., 1988, Nature, 333, 319
Baum S. A., McCarthy P. J., 2000, AJ, 119, 2634
Baum S. A., Heckman T. M., van Breugel W., 1992, ApJ, 389, 208
Becker R. H., White R. L., Helfand D. J., 1995, ApJ, 450, 559
Becker R. H., et al., 2001, AJ, 122, 2850
Belsole E., Worrall D. M., Hardcastle M. J., Croston J. H., 2007, MNRAS, 381, 1109
Best P. N., Heckman T. M., 2012, MNRAS, 421, 1569
Best P. N., Longair M. S., Röttgering H. J. A., 1998a, MNRAS, 295, 549
Best P. N., et al., 1998b, MNRAS, 301, L15
Best P. N., Röttgering H. J. A., Longair M. S., 2000, MNRAS, 311, 23
Best P. N., Kauffmann G., Heckman T. M., Ivezić Ž., 2005, MNRAS, 362, 9
Bilicki M., Jarrett T. H., Peacock J. A., Cluver M. E., Steward L., 2014, ApJS, 210, 9
Bird J., Martini P., Kaiser C., 2008, ApJ, 676, 147
Bîrzan L., Rafferty D. A., McNamara B. R., Wise M. W., Nulsen P. E. J., 2004, ApJ, 607, 800
Bîrzan L., McNamara B. R., Nulsen P. E. J., Carilli C. L., Wise M. W., 2008, ApJ, 686, 859

Blandford R. D., Payne D. G., 1982, MNRAS, 199, 883
Blandford R. D., Rees M. J., 1974, MNRAS, 169, 395
Blandford R. D., Znajek R. L., 1977, MNRAS, 179, 433
Blumenthal G., Miley G., 1979, A&A, 80, 13
Blundell K. M., Rawlings S., 1999, Nature, 399, 330
Blundell K. M., Rawlings S., Eales S. A., Taylor G. B., Bradley A. D., 1998, MNRAS, 295, 265
Blundell K. M., Rawlings S., Willott C. J., 1999, AJ, 117, 677
Bornancini C. G., De Breuck C., de Vries W., Croft S., van Breugel W., Röttgering H., Minniti D., 2007, MNRAS, 378, 551
Bradley L., et al., 2017, astropy/photutils: v0.4, doi:10.5281/zenodo.1039309, https://doi.org/10.5281/zenodo.1039309
Brammer G. B., van Dokkum P. G., Coppi P., 2008, ApJ, 686, 1503
Bridge J. S., et al., 2015, ApJ, 799, 205
Brook P. R., Karastergiou A., Johnston S., Kerr M., Shannon R. M., Roberts S. J., 2016, MNRAS, 456, 1374
Brown M. J. I., et al., 2014, ApJS, 212, 18
Brusa M., et al., 2009, ApJ, 693, 8
Bruzual G., Charlot S., 2003, MNRAS, 344, 1000
Callingham J. R., et al., 2015, ApJ, 809, 168
Callingham J. R., et al., 2017, ApJ, 836, 174
Calzetti D., Armus L., Bohlin R. C., Kinney A. L., Koornneef J., Storchi-Bergmann T., 2000, ApJ, 533, 682
Carilli C. L., 2003, New A Rev., 47, 231
Carilli C. L., Harris D. E., Pentericci L., Röttgering H. J. A., Miley G. K., Kurk J. D., van Breugel W., 2002a, ApJ, 567, 781
Carilli C. L., Gnedin N. Y., Owen F., 2002b, ApJ, 577, 22
Cavagnolo K. W., McNamara B. R., Nulsen P. E. J., Carilli C. L., Jones C., Bîrzan L., 2010, ApJ, 720, 1066
Chabrier G., 2003, PASP, 115, 763
Chambers K. C., Miley G. K., van Breugel W. J. M., 1988, ApJ, 327, L47
Chambers K. C., Miley G. K., van Breugel W. J. M., 1990, ApJ, 363, 21
Chambers K. C., Miley G. K., van Breugel W. J. M., Huang J.-S., 1996, ApJS, 106, 215
Chambers K. C., et al., 2016a, preprint, (arXiv:1612.05560)
Chambers K. C., et al., 2016b, preprint, (arXiv:1612.05560)
Ciardi B., et al., 2013, MNRAS, 428, 1755
Ciardi B., et al., 2015, MNRAS, 453, 101
Cimatti A., di Serego Alighieri S., Vernet J., Cohen M. H., Fosbury R. A. E., 1998, ApJ, 499, L21
Civano F., et al., 2011, ApJ, 741, 91
Collier J. D., et al., 2014, MNRAS, 439, 545
Condon J. J., Cotton W. D., Greisen E. W., Yin Q. F., Perley R. A., Taylor G. B., Broderick

J. J., 1998, AJ, 115, 1693
Cullen F., et al., 2018, MNRAS, 476, 3218
Dabhade P., Gaikwad M., Bagchi J., Pandey-Pommier M., Sankhyayan S., Raychaudhury S., 2017, MNRAS, 469, 2886
Daly R. A., 1992, ApJ, 386, L9
Daly R. A., 2009, ApJ, 696, L32
Daly R. A., Guerra E. J., 2002, AJ, 124, 1831
De Barros S., et al., 2017, A&A, 608, A123
De Breuck C., van Breugel W., Minniti D., Miley G., Röttgering H., Stanford S. A., Carilli C., 1999, A&A, 352, L51
De Breuck C., van Breugel W., Röttgering H. J. A., Miley G., 2000a, A&AS, 143, 303
De Breuck C., Röttgering H., Miley G., van Breugel W., Best P., 2000b, A&A, 362, 519
De Breuck C., et al., 2001, AJ, 121, 1241
De Breuck C., Tang Y., de Bruyn A. G., Röttgering H., van Breugel W., 2002, A&A, 394, 59
De Breuck C., et al., 2010, ApJ, 725, 36
Dewdney P. E., Hall P. J., Schilizzi R. T., Lazio T. J. L. W., 2009, IEEE Proceedings, 97, 1482
Dubois Y., Volonteri M., Silk J., 2014, MNRAS, 440, 1590
Duncan K., Conselice C. J., 2015, MNRAS, 451, 2030
Duncan K., et al., 2014, MNRAS, 444, 2960
Dunlop J. S., Peacock J. A., 1990, MNRAS, 247, 19
Dye S., et al., 2006, MNRAS, 372, 1227
Dye S., et al., 2018, MNRAS, 473, 5113
Emonts B. H. C., et al., 2014, MNRAS, 438, 2898
Emonts B. H. C., et al., 2016, Science, 354, 1128
Ewall-Wice A., Dillon J. S., Mesinger A., Hewitt J., 2014, MNRAS, 441, 2476
Fabian A. C., 2012, ARA&A, 50, 455
Fan X., et al., 2001, AJ, 122, 2833
Fan X., et al., 2004, AJ, 128, 515
Fanaroff B. L., Riley J. M., 1974, MNRAS, 167, 31P
Fanidakis N., et al., 2012, MNRAS, 419, 2797
Fanti C., Fanti R., Dallacasa D., Schilizzi R. T., Spencer R. E., Stanghellini C., 1995, A&A, 302, 317
Fontanot F., Cristiani S., Monaco P., Nonino M., Vanzella E., Brandt W. N., Grazian A., Mao J., 2007, A&A, 461, 39
Frail D. A., Jagannathan P., Mooley K. P., Intema H. T., 2016, ApJ, 829, 119
Fukazawa Y., Makishima K., Ohashi T., 2004, PASJ, 56, 965
Furlanetto S. R., Loeb A., 2002, ApJ, 579, 1
Gabányi K. É., Frey S., Gurvits L. I., Paragi Z., Perger K., 2018, Research Notes of the American Astronomical Society, 2, 200
Galametz A., et al., 2012, ApJ, 749, 169

Garn T., Alexander P., 2008, MNRAS, 391, 1000
Garn T. S., Green D. A., Riley J. M., Alexander P., 2010, Bulletin of the Astronomical Society of India, 38, 103
Godfrey L. E. H., Shabala S. S., 2013, ApJ, 767, 12
Gunn J. E., Peterson B. A., 1965, ApJ, 142, 1633
Harwood J. J., Hardcastle M. J., Croston J. H., Goodger J. L., 2013, MNRAS, 435, 3353
Hasinger G., Miyaji T., Schmidt M., 2005, A&A, 441, 417
Hatch N. A., et al., 2011, MNRAS, 410, 1537
Hatch N. A., et al., 2014, MNRAS, 445, 280
Heald G. H., et al., 2015, A&A, 582, A123
Herzog A., Middelberg E., Norris R. P., Sharp R., Spitler L. R., Parker Q. A., 2014, A&A, 567, A104
Hey J. S., Parsons S. J., Phillips J. W., 1946, Nature, 158, 234
Hogan M. T., et al., 2015, MNRAS, 453, 1201
Hunter J. D., 2007a, Computing In Science & Engineering, 9, 90
Hunter J. D., 2007b, Computing In Science & Engineering, 9, 90
Hurley-Walker N., 2017, preprint, (arXiv:1703.06635)
Intema H. T., Jagannathan P., Mooley K. P., Frail D. A., 2017, A&A, 598, A78
Ishwara-Chandra C. H., Sirothia S. K., Wadadekar Y., Pal S., Windhorst R., 2010, MNRAS, 405, 436
Jackson C. A., Wall J. V., 1999, MNRAS, 304, 160
Jannuzi B. T., Elston R., Schmidt G. D., Smith P. S., Stockman H. S., 1995, ApJ, 454, L111
Jansky K. G., 1933a, Popular Astronomy, 41, 548
Jansky K. G., 1933b, Nature, 132, 66
Janssen R. M. J., Röttgering H. J. A., Best P. N., Brinchmann J., 2012, A&A, 541, A62
Jarvis M. J., et al., 2001a, MNRAS, 326, 1563
Jarvis M. J., Rawlings S., Eales S., Blundell K. M., Bunker A. J., Croft S., McLure R. J., Willott C. J., 2001b, MNRAS, 326, 1585
Jarvis M. J., Teimourian H., Simpson C., Smith D. J. B., Rawlings S., Bonfield D., 2009, MNRAS, 398, L83
Jiang L., et al., 2016, ApJ, 833, 222
Kaiser C. R., Alexander P., 1997, MNRAS, 286, 215
Kaiser C. R., Best P. N., 2007, MNRAS, 381, 1548
Kaiser C. R., Dennett-Thorpe J., Alexander P., 1997, MNRAS, 292, 723
Kalfountzou E., Jarvis M. J., Bonfield D. G., Hardcastle M. J., 2012, MNRAS, 427, 2401
Kashikawa N., et al., 2006, ApJ, 648, 7
Kashikawa N., et al., 2011, ApJ, 734, 119
Kashikawa N., et al., 2015, ApJ, 798, 28
Kelly B. C., Vestergaard M., Fan X., Hopkins P., Hernquist L., Siemiginowska A., 2010, ApJ, 719, 1315
Ker L. M., Best P. N., Rigby E. E., Röttgering H. J. A., Gendre M. A., 2012, MNRAS,

420, 2644
Klamer I. J., Ekers R. D., Sadler E. M., Weiss A., Hunstead R. W., De Breuck C., 2005, ApJ, 621, L1
Kodama T., Tanaka I., Kajisawa M., Kurk J., Venemans B., De Breuck C., Vernet J., Lidman C., 2007, MNRAS, 377, 1717
Kormendy J., Gebhardt K., 2001, in Wheeler J. C., Martel H., eds, American Institute of Physics Conference Series Vol. 586, 20th Texas Symposium on relativistic astrophysics. pp 363–381 (arXiv:astro-ph/0105230), doi:10.1063/1.1419581
Krolik J. H., Chen W., 1991, AJ, 102, 1659
Kurk J. D., Cimatti A., di Serego Alighieri S., Vernet J., Daddi E., Ferrara A., Ciardi B., 2004, A&A, 422, L13
Lacy M., et al., 1994, MNRAS, 271, 504
Lacy M., Bunker A. J., Ridgway S. E., 2000, AJ, 120, 68
Laing R. A., Riley J. M., Longair M. S., 1983, MNRAS, 204, 151
Lang D., 2014, AJ, 147, 108
Large M. I., Mills B. Y., Little A. G., Crawford D. F., Sutton J. M., 1981, MNRAS, 194, 693
Lawrence A., et al., 2007a, MNRAS, 379, 1599
Lawrence A., et al., 2007b, MNRAS, 379, 1599
Lidman C., Hayes M., Jones D. H., Schaerer D., Westra E., Tapken C., Meisenheimer K., Verhamme A., 2012, MNRAS, 420, 1946
Lilly S. J., 1988, ApJ, 333, 161
Lilly S. J., Longair M. S., 1984, MNRAS, 211, 833
Mack K. J., Wyithe J. S. B., 2012, MNRAS, 425, 2988
Mahony E. K., et al., 2016, MNRAS, 463, 2997
Maini A., Prandoni I., Norris R. P., Spitler L. R., Mignano A., Lacy M., Morganti R., 2016, A&A, 596, A80
Manchester R. N., Hobbs G. B., Teoh A., Hobbs M., 2005, AJ, 129, 1993
Martini P., et al., 2013, ApJ, 768, 1
Matthee J., Sobral D., Darvish B., Santos S., Mobasher B., Paulino-Afonso A., Röttgering H., Alegre L., 2017, MNRAS, 472, 772
Mayo J. H., Vernet J., De Breuck C., Galametz A., Seymour N., Stern D., 2012, A&A, 539, A33
McCarthy P. J., 1993, ARA&A, 31, 639
McCarthy P. J., Baum S. A., Spinrad H., 1996, ApJS, 106, 281
McLure R. J., Willott C. J., Jarvis M. J., Rawlings S., Hill G. J., Mitchell E., Dunlop J. S., Wold M., 2004, MNRAS, 351, 347
McLure R. J., et al., 2006, MNRAS, 372, 357
McLure R. J., et al., 2018, MNRAS, 476, 3991
Meier D. L., 2002, New A Rev., 46, 247
Merritt D., Ferrarese L., 2001, ApJ, 547, 140
Middelberg E., Norris R. P., Hales C. A., Seymour N., Johnston-Hollitt M., Huynh M. T.,

Lenc E., Mao M. Y., 2011, A&A, 526, A8
Miley G. K., 1968, Nature, 218, 933
Miley G., De Breuck C., 2008, A&A Rev., 15, 67
Miley G. K., Chambers K. C., van Breugel W. J. M., Macchetto F., 1992, ApJ, 401, L69
Miley G. K., et al., 2004, Nature, 427, 47
Miley G. K., et al., 2006, ApJ, 650, L29
Minkowski R., 1960, ApJ, 132, 908
Morabito L. K., Harwood J. J., 2018, MNRAS, 480, 2726
Morabito L. K., et al., 2017, submitted
Morganti R., et al., 2006, MNRAS, 371, 157
Mosleh M., et al., 2012, ApJ, 756, L12
Narayan R., Yi I., 1994, ApJ, 428, L13
Neeser M. J., Eales S. A., Law-Green J. D., Leahy J. P., Rawlings S., 1995, ApJ, 451, 76
Nesvadba N. P. H., Lehnert M. D., De Breuck C., Gilbert A. M., van Breugel W., 2008, A&A, 491, 407
Nesvadba N. P. H., De Breuck C., Lehnert M. D., Best P. N., Collet C., 2017, A&A, 599, A123
Nilsson K., Valtonen M. J., Kotilainen J., Jaakkola T., 1993, ApJ, 413, 453
Norris R. P., 2017, Nature Astronomy, 1, 671
Norris R. P., et al., 2006, AJ, 132, 2409
Ono Y., et al., 2013, ApJ, 777, 155
Orsi Á. A., Fanidakis N., Lacey C. G., Baugh C. M., 2016, MNRAS, 456, 3827
Ouchi M., et al., 2008, ApJS, 176, 301
Overzier R. A., 2016, A&A Rev., 24, 14
Overzier R. A., et al., 2006, ApJ, 637, 58
Overzier R. A., et al., 2009, ApJ, 704, 548
Parijskij Y. N., et al., 2014, MNRAS, 439, 2314
Parma P., Murgia M., de Ruiter H. R., Fanti R., Mack K.-H., Govoni F., 2007, A&A, 470, 875
Pentericci L., et al., 2000, A&A, 361, L25
Pérez F., Granger B. E., 2007, Computing in Science and Engineering, 9, 21
Planck Collaboration et al., 2014, A&A, 571, A16
Rawlings S., Lacy M., Blundell K. M., Eales S. A., Bunker A. J., Garrington S. T., 1996, Nature, 383, 502
Rawlings S., Eales S., Lacy M., 2001, MNRAS, 322, 523
Reber G., 1944, ApJ, 100, 279
Rengelink R. B., Tang Y., de Bruyn A. G., Miley G. K., Bremer M. N., Röttgering H. J. A., Bremer M. A. R., 1997, A&AS, 124
Reuland M., Röttgering H., van Breugel W., De Breuck C., 2004, MNRAS, 353, 377
Rhoads J. E., et al., 2003, AJ, 125, 1006
Rigby E. E., Best P. N., Brookes M. H., Peacock J. A., Dunlop J. S., Röttgering H. J. A., Wall J. V., Ker L., 2011, MNRAS, 416, 1900

Rigby E. E., Argyle J., Best P. N., Rosario D., Röttgering H. J. A., 2015, A&A, 581, A96
Robinson A., Binette L., Fosbury R. A. E., Tadhunter C. N., 1987, MNRAS, 227, 97
Robitaille T., Bressert E., 2012, APLpy: Astronomical Plotting Library in Python, Astrophysics Source Code Library (ascl:1208.017)
Rocca-Volmerange B., Le Borgne D., De Breuck C., Fioc M., Moy E., 2004, A&A, 415, 931
Roche N., Franzetti P., Garilli B., Zamorani G., Cimatti A., Rossetti E., 2012, MNRAS, 420, 1764
Röttgering H. J. A., Lacy M., Miley G. K., Chambers K. C., Saunders R., 1994, A&AS, 108, 79
Röttgering H. J. A., van Ojik R., Miley G. K., Chambers K. C., van Breugel W. J. M., de Koff S., 1997, A&A, 326, 505
Röttgering H., Daddi E., Overzier R., Wilman R., 2003, New A Rev., 47, 309
Ryle M., Scheuer P. A. G., 1955, Proceedings of the Royal Society of London Series A, 230, 448
Saito T., Shimasaku K., Okamura S., Ouchi M., Akiyama M., Yoshida M., Ueda Y., 2008, ApJ, 675, 1076
Sanders R. L., et al., 2016, ApJ, 816, 23
Saxena A., Röttgering H. J. A., Rigby E. E., 2017, MNRAS, 469, 4083
Saxena A., et al., 2018a, MNRAS, 475, 5041
Saxena A., et al., 2018b, MNRAS, 475, 5041
Saxena A., et al., 2018c, MNRAS, 480, 2733
Schaye J., et al., 2015, MNRAS, 446, 521
Scheuer P. A. G., 1974, MNRAS, 166, 513
Schmidt M., 1968, ApJ, 151, 393
Schmidt M., Schneider D. P., Gunn J. E., 1995, AJ, 110, 68
Schwartz D. A., 2002, ApJ, 569, L23
Seifert W., et al., 2003, in Iye M., Moorwood A. F. M., eds, Proc. SPIEVol. 4841, Instrument Design and Performance for Optical/Infrared Ground-based Telescopes. pp 962–973, doi:10.1117/12.459494
Seymour N., et al., 2007, ApJS, 171, 353
Seymour N., et al., 2008, ApJ, 681, L1
Shakeshaft J. R., Ryle M., Baldwin J. E., Elsmore B., Thomson J. H., 1955, MmRAS, 67, 106
Shakura N. I., Sunyaev R. A., 1973, A&A, 24, 337
Shankar F., Weinberg D. H., Miralda-Escudé J., 2009, ApJ, 690, 20
Shankar F., Weinberg D. H., Miralda-Escudé J., 2013, MNRAS, 428, 421
Shapiro S. L., 2005, ApJ, 620, 59
Sheldon E. S., Cunha C. E., Mandelbaum R., Brinkmann J., Weaver B. A., 2012, ApJS, 201, 32
Shibuya T., et al., 2018, PASJ, 70, S15
Shimakawa R., et al., 2015, MNRAS, 451, 1284

Shimwell T. W., et al., 2017, A&A, 598, A104

Sieber W., 1973, A&A, 28, 237

Silverman J. D., et al., 2005, ApJ, 624, 630

Singal A. K., Laxmi Singh R., 2013, ApJ, 766, 37

Singh V., et al., 2014, A&A, 569, A52

Singh V., Wadadekar Y., Ishwara-Chandra C. H., Sirothia S., Sievers J., Beelen A., Omont A., 2017, MNRAS, 470, 4956

Smith H. E., Spinrad H., 1980, ApJ, 236, 419

Smith D. J. B., et al., 2016, in Reylé C., Richard J., Cambrésy L., Deleuil M., Pécontal E., Tresse L., Vauglin I., eds, SF2A-2016: Proceedings of the Annual meeting of the French Society of Astronomy and Astrophysics. pp 271–280 (`arXiv:1611.02706`)

Spinrad H., 1982, PASP, 94, 397

Spinrad H., Westphal J., Kristian J., Sandage A., 1977, ApJ, 216, L87

Spinrad H., Dey A., Graham J. R., 1995, ApJ, 438, L51

Springel V., et al., 2005, Nature, 435, 629

Steidel C. C., Pettini M., Hamilton D., 1995, AJ, 110, 2519

Steidel C. C., et al., 2014, ApJ, 795, 165

Stevens J. A., et al., 2003, Nature, 425, 264

Surace J. A., Shupe D. L., Fang F., Evans T., Alexov A., Frayer D., Lonsdale C. J., SWIRE Team 2005, in American Astronomical Society Meeting Abstracts. p. 1246

Swarup G., Ananthakrishnan S., Kapahi V. K., Rao A. P., Subrahmanya C. R., Kulkarni V. K., 1991, Current Science, Vol. 60, NO.2/JAN25, P. 95, 1991, 60, 95

Taylor M. B., 2005, in Shopbell P., Britton M., Ebert R., eds, Astronomical Society of the Pacific Conference Series Vol. 347, Astronomical Data Analysis Software and Systems XIV. p. 29

Tielens A. G. G. M., Miley G. K., Willis A. G., 1979, A&AS, 35, 153

Tingay S. J., et al., 2013a, PASA, 30, e007

Tingay S. J., et al., 2013b, PASA, 30, e007

Vardoulaki E., et al., 2010, MNRAS, 401, 1709

Venemans B. P., et al., 2002, ApJ, 569, L11

Venemans B. P., et al., 2007, A&A, 461, 823

Villar-Martin M., Tadhunter C., Clark N., 1997, A&A, 323, 21

Villar-Martín M., Humphrey A., De Breuck C., Fosbury R., Binette L., Vernet J., 2007a, MNRAS, 375, 1299

Villar-Martín M., Humphrey A., De Breuck C., Fosbury R., Binette L., Vernet J., 2007b, MNRAS, 375, 1299

Volonteri M., Sikora M., Lasota J.-P., 2007, ApJ, 667, 704

Waddington I., Windhorst R. A., Cohen S. H., Partridge R. B., Spinrad H., Stern D., 1999, ApJ, 526, L77

Wagner A. Y., Bicknell G. V., Umemura M., 2012, ApJ, 757, 136

Wall J. V., Jackson C. A., Shaver P. A., Hook I. M., Kellermann K. I., 2005, A&A, 434, 133

Wan L., Daly R. A., Guerra E. J., 2000, ApJ, 544, 671
Wayth R. B., et al., 2015, PASA, 32, e025
White R. L., Becker R. H., Helfand D. J., Gregg M. D., 1997, ApJ, 475, 479
Williams W. L., Röttgering H. J. A., 2015, MNRAS, 450, 1538
Willott C. J., Rawlings S., Blundell K. M., Lacy M., 1999, MNRAS, 309, 1017
Willott C. J., Rawlings S., Blundell K. M., Lacy M., Eales S. A., 2001, MNRAS, 322, 536
Willott C. J., Rawlings S., Blundell K. M., Lacy M., Hill G. J., Scott S. E., 2002, MNRAS, 335, 1120
Willott C. J., Rawlings S., Jarvis M. J., Blundell K. M., 2003, MNRAS, 339, 173
Willott C. J., et al., 2010a, AJ, 139, 906
Willott C. J., et al., 2010b, AJ, 140, 546
Woo J.-H., Urry C. M., 2002, ApJ, 579, 530
Wright E. L., et al., 2010a, AJ, 140, 1868
Wright E. L., et al., 2010b, AJ, 140, 1868
Wu J., et al., 2012, ApJ, 756, 96
Wylezalek D., et al., 2013, ApJ, 769, 79
Xu Y., Chen X., Fan Z., Trac H., Cen R., 2009, ApJ, 704, 1396
Zaroubi S., 2013, in Wiklind T., Mobasher B., Bromm V., eds, Astrophysics and Space Science Library Vol. 396, The First Galaxies. p. 45 (arXiv:1206.0267), doi:10.1007/978-3-642-32362-1_2
de Gasperin F., Intema H. T., Frail D. A., 2017, preprint, (arXiv:1711.11367)
van Breugel W., De Breuck C., Stanford S. A., Stern D., Röttgering H., Miley G., 1999, ApJ, 518, L61
van Haarlem M. P., et al., 2013, A&A, 556, A2
van Ojik R., Röttgering H. J. A., Carilli C. L., Miley G. K., Bremer M. N., Macchetto F., 1996, A&A, 313, 25
van Ojik R., Röttgering H. J. A., Miley G. K., Hunstead R. W., 1997, A&A, 317, 358
van der Wel A., et al., 2014, ApJ, 788, 28
van der Werf P. P., 1999, The Most Distant Radio Galaxies, Proceedings of the colloquium, p. 161

Nederlandse Samenvatting

Het doel van dit proefschrift is om met behulp van de nieuwste en diepste radio waarnemingen van de hemel op lage frequenties zeer ver weg gelegen radio sterrenstelsels te vinden die vervolgens gebruikt kunnen worden ter bestudering van het tijdperk van reionisatie en de formatie en evolutie van sterrenstelsels. Om een algemeen begrip van zeer verre radio sterrenstelsels te verkrijgen bevat dit proefschrift een combinatie van theoretisch werk en observationeel werk gebaseerd op waarnemingen in het radio, optisch en infrarode deel van het spectrum, gecombineerd met modellen om deze waarnemingen te interpreteren. De waarnemingen die in dit proefschrift gepresenteerd worden zijn verkregen met de nieuwste faciliteiten ter wereld, namelijk de *Karl G. Jansky Very Large Array (VLA)*, *William Herschel Telescope (WHT)*, *Large Binocular Telescope (LBT)*, *Gemini North Telescope*, *Hobby-Eberly Telescope (HET)*, *Gran Telescopio Canarias (GTC)* and de *Very Large Telescope (VLT)*. Hieronder geven we een korte beschrijving van elk hoofdstuk in dit proefschrift.

In Hoofdstuk 2 modelleren we de groei van radiobronnen om het aantal van heldere radio sterrenstelsels op z 6 te voorspellen. Deze verre objecten zouden kunnen gebruikt worden om het tijdperk van reionisatie te bestuderen. We beginnen met het construeren van een model dat op basis van de massa en spin van een superzware zwarte gat de kracht van de jet en de geassocieerde radio helderheid berekent. In ons model is er mee rekening gehouden dat tijdens hun groei deze radiobronnen door verschillende fysische processen energie verliezen. Met ons model kunnen we de verdeling van de radiobronnen in de ruimte voorspellen in ieder specifiek tijdperk, samen met de verdeling van de grootte van radiobronnen. We testen eerst ons model op $z = 2$, waar een grote hoeveelheid radio waarnemingen beschikbaar zijn, en laten zien dat onze voorspellingen goed overeenkomen met waarnemingen. Vervolgens gebruiken we het model om de aantallen en de distributie van de groottes van radiobronnen te voorspellen op $z = 6$. Deze informatie gebruiken we dan om de beste waarneemstrategieën te definiëren zodat het aantal radio sterrenstelsels dat waargenomen kan worden op op $z = 6$ geoptimaliseerd wordt, en zo kan een belangrijke vraag omtrent verre radio sterrenstelsels beantwoord: *Hoe veel radio sterrenstelsels bestaan er op $z = 6$ en hoe kunnen wij hen vinden?*

In Hoofdstuk 3 presenteren wij de eerste resultaten van een observationeel onderzoek naar radio sterrenstelsels. Veelbelovende kandidaten voor radio sterrenstelsels op hoge roodverschuiving zijn geselecteerd op 150 MHz door middel van selectie technieken die eerder in deze Introductie zijn besproken. Voor 32 veelbelovende kandidaten presenteren we hoge resolutie radio waarnemingen die verkregen zijn met de VLA. We presenteren ook de globale optische en infrarode eigenschappen van deze sterrenstelsels, en bepalen de fotometrische roodverschuiving voor een handvol stelsels, waar voor diepere fotometrische waarnemingen in optische en infrarode golflengten beschikbaar zijn. We presenteren de radio eigenschapen van de selectie, en testen of de lage frequentie spectra tekenen van kromming laten zien, welke vaak waargenomen zijn in HzRGs. We rapporteren ook de toevallige ontdekking van een gigantisch radio stelsel (GRG) met een fotometrische roodverschuiving van 1.8 ± 0.5. Dit hoofdstuk beantwoordt de vraag: *Hoe succesvol kunnen diepere radio waarnemingen zijn om verre radio sterrenstelsels te detecteren?*

In Hoofdstuk 4 rapporteren we de ontdekking van het verste radio stelsel dat bekend is tot nu toe, TGSS J1530+1049 op $z = 5.72$, welke zich dicht bij het einde van het tijdperk van reionisatie bevindt. Dit sterrenstelsel was in eerste instantie geselecteerd als een veelbelovende radiobron in Hoofdstuk 3 en spectroscopische en nabij-infrarode fotometrische waarnemingen hebben vervolgens geholpen om zijn roodverschuiving vast te stellen. Deze ontdekking breekt het vorige record van het verste radio sterrenstelsel, van bijna 20 jaar geleden. In dit Hoofdstuk presenteren we verder een gedetailleerde analyse van de Lyman alpha (Lyα) emissie lijn van dit sterrenstelsel en hoe de Lyα en radio eigenschappen (zoals de helderheid en grootte) zich verhouden tot andere radio stelsels op hoge roodverschuivingen, evenals 'niet-radio' sterrenstelsels op vergelijkbare roodverschuivingen. We maken ook schattingen van de stermassa van dit stelsel en laten zien dat TGSS J1530+1049 een erg jong radio stelsel moet zijn. Dit Hoofdstuk zet een eerste stap in de richting naar het beantwoorden van de vraag: *Hoe ziet een radio stelsel eruit dat zich erg dicht bij het tijdperk van remionisatie bevindt?*

In Hoofdstuk 5 presenteren we resultaten van een spectroscopisch onderzoek om de roodverschuiving van veelbelovende kandidaten uit Hoofdstuk 3 te meten. We zijn in staat om radio sterrenstelsels op verschillende roodverschuivingen te identificeren die bijna een orde van grootte zwakker zijn in radio helderheid dan eerder ontdekte radio stelsels. We laten ook nabij-infrarode waarneming zien voor een deel van de bevestigde bronnen om hun stermassa te schatten. Vervolgens selecteren we bekende $z \sim 2$ radio sterrenstelsels uit de literatuur en combineren deze met onze nieuw ontdekte sterrenstelsels om een groter sample te vormen. We kijken dan naar de eigenschappen van de radio emissie en emissie lijnen van deze grotere selectie, en vinden correlaties tussen veel van deze eigenschappen en introduceren scenarios die open vragen omtrent radio melkwegstelsels op hoge roodverschuiving beantwoorden. Dit hoofdstuk behandelt de vraag: *Wat is de oorsprong van radio sterrenstelsels die zich bevinden op hoge roodverschuiving?*

List of publications

First author

Saxena A., Marinello M., Overzier R.A., Best P.N., Röttgering H.J.A., Duncan K.J., Prandoni I., Pentericci L., Magliocchetti M., Paris D., Cusano F., Marchi F., Intema H.T. and Miley G.K., 2018, *Discovery of a radio galaxy at* $z = 5.72$, MNRAS, 480, 2733.

Saxena A., Jagannathan P., Röttgering H.J.A., Best P.N., Intema H.T., M. Zhang, Duncan K.J., Carilli C.L. and Miley G.K., 2018, *A search for faint high-redshift radio galaxy candidates at 150 MHz*, MNRAS, 475, 5041.

Saxena A., Röttgering H.J.A. and Rigby E.E., 2017, *Modelling the luminosities and sizes of radio sources: radio luminosity function at* $z = 6$, MNRAS, 469, 4083.

Saxena A. and Röttgering H.J.A., 2018, *High-redshift radio galaxies at low radio frequencies*, Proceedings of the IAU Focus Meeting 3: "Radio Galaxies: Resolving the AGN phenomenon".

Contributing author

Omar A., **Saxena A.**, Chand K., Paswan A., Röttgering H.J.A., Duncan K.J., Kumar T.S., Krishnareddy B., Pant J., 2019, *Optical detection of a GMRT-detected candidate high-redshift radio galaxy with 3.6-m Devasthal optical telescope*, Journal of Astrophysics and Astronomy, 40, 9.

Sabater J., et al., 2019, *The LoTSS view of radio AGN in the local Universe. The most massive galaxies are always switched on*, A& A, 622, A17.

Shimwell T.W., et al., 2019, *The LOFAR Two-metre Sky Survey. II. First data release*, A& A, 622, A1.

Morabito L.K., Williams W.L., Duncan, K.J., Röttgering H.J.A., Miley, G.K., **Saxena, A.**, et al., 2017, *Investigating the unification of LOFAR-detected powerful AGN in the Boötes field*, MNRAS, 469, 1883.

Kerkhoven A.H., Russo P., Land-Zandstra A.M., **Saxena A.** and Rodenburg F.J., 2016, *Gender Stereotypes in Science Education Resources: A Visual Content Analysis*, PLoS ONE, 11(11): e0165037.

Curriculum Vitae

I was born in New Delhi, India on 30 September 1992. As a kid, I always found myself doing well at science and maths. But if given a choice, I much preferred going out to play football rather than be in the classroom. I started developing an interest in astronomy at the age of around 13, thanks to some introductory physics courses about gravitation and how it kept the planets in motion around the Sun. I was also part of the Astronomy Club in middle school and a field trip out in the country side with the club, armed with some amateur telescopes and plenty of snacks, changed my perception of the cosmos forever. On a moonless night, we saw the moons of Jupiter, the rings of Saturn and for the first time in my life, I could see the Milky Way, which for a city boy like me was absolutely mind-blowing. I remember just laying on the grassy field for an hour, looking up and feeling insignificant. From that day my interest in Astronomy grew, and I think I knew somewhere at the back of my mind that Astronomy is what I truly enjoyed studying.

After finishing school, I enrolled in a Bachelor in Physics (with Honours) at the University of Delhi. During my Bachelors degree, I had the pleasure of coming across many nice teachers and supervisors who helped build my motivation to apply for a Masters degree. I then obtained a Masters in Astrophysics from University College London, towards the end of which I knew that I would like to pursue a career in scientific research. The main driving force was my Masters thesis supervisor, Prof. Kinwah Wu, who taught me so much, inspired me everyday with his knowledge and his personality and motivated me to not just be a good scientist, but also be a good human being. His selflessness and intelligence gave me something to strive for, and if not for his advice, I probably would not have ended up in Leiden for my PhD.

I will never forget my time in Leiden, both because of the amazing life experiences I've had and because of how much I have grown as a scientist and as a person. I arrived at Leiden Observatory in November of 2014 to start a PhD with Prof. Huub Röttgering, studying distant radio AGN. I had very little experience with radio astronomy, and had been a theoretician all my life. Leiden gave me the platform and the resources to continue my growth as a scientist. Thanks to Huub's unwavering support, I was fortunate to have worked on a project that involved theory/modelling, radio astronomy, optical spectroscopy and near-infrared imaging. In Leiden I gained my first telescope observing experience, which has the power to reinforce one's love for astronomy and I have found myself going observing regularly ever since. I also had the opportunity to travel to the biggest institutes and conferences around the world to collaborate and present my results. Being surrounded by inspiring people helped me set high standards for myself and step out of my comfort zone.

I aim to continue my growth as a scientist and maintain a wide variety of research interests, which is why I have switched gears a little bit and decided to pursue research in the formation and evolution of galaxies at high redshifts. I have now moved to the Osservatorio Astronomico di Roma, Italy for my postdoc and I am looking forward to seeing the sun a lot more, and learning new things and accumulating new experiences. One thing that has not changed is the fact that if given an option, I would still much prefer to play (or watch) football, any day of the week.

Acknowledgements

There are so many people to thank that it is hard to know where to start. As the famous Nigerian saying goes, *"it takes a village to raise a child"*, it is certainly true that it takes the support of a large number of people to produce a successful PhD thesis. It seems fitting to start by thanking the amazing support staff at Leiden Observatory. Evelijn Gerstel, Alexandra Schouten-Voskamp, Marjan Balkestein and Yvonne Kluijt, thank you so much for making me feel welcome and settled in right from the very first day. The IT staff, including Erik Deul and Eric van der Kraan, thank you for always being there to solve our issues and making sure we have absolutely no troubles at all when it comes to doing our jobs. Having this kind of support is vital to performing our research duties to the best of our capabilities. Also thanks to the members of the open source community all around the world who put in countless hours to make software easily accessible.

I deeply cherished my time in Leiden and so many people made it worthwhile. Mieke, we have come a long way from when we first started out on the 11th floor and struggled to learn each other's names. Thank you for always being there and I always knew that I could talk to you about anything in the world. Ele, I admire your positivity and your appetite to learn. Your calming influence, even though you seem to almost always be in a state of panic, was vital in maintaining (I hope mutually) our mental stability. Jorryt, I thoroughly enjoyed discussing everything from resonant scattering of Lyα photons to the aerodynamics of a road bike with you and look forward to more such discussions. Ken, thanks for playing the role of my academic 'big brother' and I learnt a lot from you. Gaby, we started our PhD journey together and it is lovely to see you grow and evolve into a wonderful scientist and human being. Christian, it has been an absolute pleasure knowing you and I will always remember our adventures early in the PhD. Thanks to my PhD cohort – Andrew, Ann-Sofie, Chris, Eva, Geert-Jan, Igone, Kirstin, Mason, Mike, Pedro – we did it! Thank you Christos, Jit, Maria Cristina and Tommaso for the great memories. A special thanks to my research group – Andra, Alex, Duy, Edwin, Frits, Gabriella, Huib, Jonah, Josh, Julius, Kim, Leah, Martijn, Rafael, Reinout, Wendy and all other current and past members. Maolin, it was a pleasure getting to know a kind and gentle soul like yours and we miss you. Thanks to the other wonderful people I met at the observatory – Allison, Andrej, Berenice, Carmen, Clement, Daniel, David, Emanuele, Francisca, Fraser, Jeroen, Kirsty, Leindert, Leo, Liz, Luke, Marcelo, Marco, Mattia, Matus, Michael, Nico, Niels, Pedro, Pratik, Santiago, Themiya, Valeria and anyone else I may have missed.

Outside of work, I had the pleasure of meeting some great people through organisation of festivals and sporting activities. Laura, it has been great getting to know you over the past few years and curating films, organising LISFE, supporting each other through crises and talking about so many different topics is something I will cherish. Thanks to my other friends from LISFE – Anastasia, Dieter, Eleonora, Evita, Izzy, Klara, Melissa, Stefano and Yara. A massive thank you to all members of my football team, Leiden Football Factory – I looked forward to our training sessions and matches every week. Benoit, Jelmer and Pedro, thanks for the good times, even though beer and McDonald's after matches was probably not what the doctor ordered.

There are a few key people who helped shape my scientific career so far. Prof. Patrick Das Gupta, thank you for giving me my first research experience in astrophysics. Prof. Kinwah Wu, thank you for inspiring me to become a good scientist and an even better human being. George, your undying passion for astronomy and using it to make the world a better place serves as an inspiration for all of us. I hope to follow in your footsteps and never lose the drive to use astronomy to make people's lives better. Although it is not customary to thank your supervisor for "doing their job", Huub, you have been more than just a supervisor and working with you has been a pleasure. Thanks to your mentorship, I have become a more independent and capable researcher. I thoroughly enjoyed discussing Johan Cruijff's footballing philosophies with you in our free time and I hope all my future supervisors share the same passion for sport (and life in general) as you do.

Silvia, thank you so much for standing by me through some of the toughest periods of the PhD. I know how annoying I can be and the patience and affection you have shown is something that I am deeply grateful for. I hope in a couple of years I can be there for you as you finish your PhD, although you are much smarter and I'm sure you will handle it better than I did.

Perhaps the most important people I would like to thank are my parents, Anil and Seema. You have always supported me throughout my life and my career, and without your unconditional love and support none of this would have been possible. Papa, thank you for inspiring me to be a critical thinker and having discussions with you and taking your advice has always helped me. Mumma, thank you for teaching me to stay humble, and for showing me that sometimes thinking from the heart is the right thing to do.